IMPROVEMENT OF WAVE STRUCTURE INTERACTION CALCULATION WITH APPLICATIONS TO THE SHALLOW WATER, MANEUVERING IN WAVES AND HULL FORM OPTIMIZATION

A Dissertation

by

ZHITIAN XIE

Submitted to the Office of Graduate and Professional Studies of
Texas A&M University
in partial fulfillment of the requirements for the degree of

DOCTOR OF PHILOSOPHY

Chair of Committee,	Jeffrey Falzarano
Committee Members,	Moo-Hyun Kim
	Robert Randall
	Richard Mercier
	Alan Palazzolo
Head of Department,	Sharath Girimaji

May 2021

Major Subject: Ocean Engineering

ABSTRACT

The goal of this work is to develop an improved hydrodynamic analysis methodology with applications to the numerical evaluation of Green's function in shallow water, maneuvering in waves and floating systems hull optimization, which involves several distinct topics that are steps leading towards a definite goal. A numerical evaluation of Green's function in finite water depth has been firstly developed using the Gauss-Legendre integral, with improved efficiency and efficacy in solving the 1st-order diffraction and radiation hydrodynamic problem. The expression of the 2nd-order wave loads has been derived in a unique form and the quadratic transfer function of a floating structure has been numerically estimated. Moreover, the effect of the floating structure's forward speed or current velocity on the 2nd-order mean drift loads has been compared using Aranha's formula, a far field method and the Neumann-Kelvin linearization, a near field method. Then, a framework involving both the seakeeping problem considering the 2nd-order wave loads with forward speed and the maneuvering problem has been developed to numerically evaluate maneuvering in waves. With the numerically estimated 1st-order and 2nd-order hydrodynamic quantities, an optimization framework has been applied to the hull of a floating structure which has been developed through the use of genetic algorithms.

This improved wave and structure interaction calculation with its applications will present a meaningful improvement in the process of the design of offshore structures of ship shape and non-ship shape hull forms.

ACKNOWLEDGEMENTS

I would like to express my sincere gratitude to my supervisor, Professor J. Falzarano, for his support, encouragement and guidance throughout my studies. His unique inspiration and wealth of knowledge in research has a great influence on me, and I believe this influence will accompany me for the rest of my life.

I would also like to thank my thesis committee members, Professor M. H. Kim and Professor R. Randall of the Ocean Engineering Department, Professor R. Mercier of the Civil & Environmental Engineering Department, Professor A. Palazzolo of the Mechanical Engineering Department, for their valuable and insightful suggestions on my thesis work.

I have learned a lot through the course work at Texas A&M University. I am especially grateful to Professor J. Falzarano, Professor M. H. Kim, Professor R. Mercier, Professor A. Palazzolo, Professor H. C. Chen who offer courses on Dynamics of Ocean Vehicles, Nonlinear Hydrodynamics Problems, Dynamics of Offshore Structures, Nonlinear Vibrations and Fluid Dynamics Ocean & Environmental Engineering which have been very useful for my academic background and thesis research.

My thanks are also due to the financial support from the Ocean Systems Simulation & Control Laboratory, Texas A&M University and American Bureau Shipping Scholarship.

Finally, I would like to express gratitude to my parents, who have been giving me the endless encouragement and love in my life. I could not have finished the study without their patience, sacrifice and support.

CONTRIBUTORS AND FUNDING SOURCES

Contributors

This work was supported by a dissertation committee consisting of Professor Jeffrey Falzarano and Professor Moo-Hyun Kim, Professor Robert Randall of the Department of Ocean Engineering and Professor Richard Mercier of the Department of Civil & Environmental Engineering and Professor Alan Palazzolo of the Department of Mechanical Engineering.

The experimental data for Section 5 was published by Hiroshima University (available online).

All other work conducted for the dissertation was completed by the student independently.

Funding Sources

Graduate study was supported by American Bureau Shipping Scholarship and the Ocean Systems Simulation & Control Laboratory, Texas A&M University.

NOMENCLATURE

A_{wp}: floating body's waterplane area

c: wave celerity

$\boldsymbol{F}$: wave forces

G: Green's functions

g: the gravity acceleration

$$\boldsymbol{H} = \frac{1}{\varepsilon^2}\begin{pmatrix} -\frac{1}{2}(\eta_5^2+\eta_6^2) & 0 & 0 \\ \eta_4\eta_5 & -\frac{1}{2}(\eta_4^2+\eta_6^2) & 0 \\ \eta_4\eta_6 & \eta_5\eta_6 & -\frac{1}{2}(\eta_4^2+\eta_5^2) \end{pmatrix}$$

h: the water depth

I_z: the moment of inertia w.r.t the vertical axis going through the midship point

J_0: the first kind Bessel function with zero order

k: the wave number

$\boldsymbol{M}$: wave moments

m: the mass

m_j: m terms

$\boldsymbol{N_{F_{\dot{v}}}}$, $\boldsymbol{N_{F_v}}$: turning moment due to sway acceleration and sway velocity

$\boldsymbol{N_{F_{\dot{r}}}}$, $\boldsymbol{YN_{F_r}}$: turning moment due to yaw acceleration and yaw rate

$\boldsymbol{n}$: normal vector

PV: the Cauchy principal value of the integral with a singularity $x_0 = k \bullet h$

$p = p(x, y, z)$: the field point

$q = q(\xi, \eta, \zeta)$: is the source point

R: the wave reflection coefficient

r: vessel's yaw rate

$\dot{r}$: acceleration of vessel's yaw rate

S: the exact wetted surface of the floating structure

S_M: the equilibrium wetted surface of the floating structure

$T_{jj}^{ic}(w_j)$: the diagonal component of the full QTF matrix

t: time

U, u: vessel's forward speed

$\dot{u}$: acceleration of vessel's forward speed

V, v: vessel's lateral speed

$\dot{v}$: acceleration of vessel's lateral speed

$\boldsymbol{W}$: steady flow velocity

$\boldsymbol{X}$: global coordinate

$\boldsymbol{X'}$: vessel-fixed coordinate

$\boldsymbol{X_0}$: the origin of the vessel-fixed coordinate in the global coordinate

$\boldsymbol{X_{F_{drift}}}, \boldsymbol{Y_{F_{drift}}}, \boldsymbol{N_{F_{drift}}}$: wave drift loads in longitudinal, lateral and yaw directions

$\boldsymbol{X_F}$, $\boldsymbol{Y_F}$, $\boldsymbol{N_F}$: surge force, sway force, yaw moment in the seakeeping problem

$\boldsymbol{X_{F_{\dot{u}}}}, \boldsymbol{X_{F_u}}$: surge force due to surge acceleration and surge velocity

x_G: horizontal distance between the center of gravity and the midship point

$\boldsymbol{Y_{F_{\dot{v}}}}, \boldsymbol{Y_{F_v}}$: sway force due to sway acceleration and sway velocity

$\boldsymbol{Y_{F\dot{r}}}$, $\boldsymbol{Y_{F_r}}$: sway force due to yaw acceleration and yaw rate

ε: a small parameter of the order of the wave slope assuming small amplitude oscillation

Φ_{total} : total wave potential

Φ: perturbation wave potential

φ : steady base flow's potential

η_i : vessel's motions in 6 degrees of freedom

$\boldsymbol{\eta} = \begin{pmatrix} \eta_1 \\ \eta_2 \\ \eta_3 \end{pmatrix}$: surge, sway and heave motions

$\boldsymbol{\alpha} = \begin{pmatrix} \eta_4 \\ \eta_5 \\ \eta_6 \end{pmatrix}$: roll, pitch and yaw motions

ζ: wave elevation

ρ: water density

ω_0 : wave frequency

ω_e : encounter frequency

ψ_R : the radiation wave potential

β : the wave direction with respect to the vessel-fixed coordinate.

Ω_R: vessel's yaw rate

TABLE OF CONTENTS

Page

LIST OF FIGURES

Page

LIST OF TABLES

Page

1. INTRODUCTION

The goal of this work is to develop an improved hydrodynamic analysis methodology with applications to the numerical evaluation of Green's function in shallow water, maneuvering in waves and floating systems hull optimization, which involves several distinct topics that are steps leading towards a definite goal. A numerical evaluation of Green's function in finite water depth has been firstly developed using the Gauss-Legendre integral, with improved efficiency and efficacy in solving the 1^{st}-order diffraction and radiation hydrodynamic problem. The expression of the 2^{nd}-order wave loads has been derived in a unique form and the quadratic transfer function of a floating structure has been numerically estimated. Moreover, the effect of the floating structure's forward speed or current velocity on the 2^{nd}-order mean drift loads has been compared using Aranha's formula, a far field method and the Neumann-Kelvin linearization, a near field method. Then, a framework involving both the seakeeping problem considering the 2^{nd}-order wave loads with forward speed and the maneuvering problem has been developed to numerically evaluate maneuvering in waves. With the numerically estimated 1^{st}-order and 2^{nd}-order hydrodynamic quantities, an optimization framework has been applied to the hull of a floating structure which has been developed through the use of genetic algorithms. This improved wave and structure interaction calculation with its applications will present a meaningful improvement in the process of the design of offshore structures of ship shape and non-ship shape hull forms.

The hydrodynamic motion and load response of offshore structures in finite water depth present different characteristics compared with those in deep water. To obtain an accurate motion response prediction of floating structures in finite water depth, an accurate and efficient numerical evaluation of Green's function and its partial derivatives for a pulsating source in finite water depth is one of the most important aspects in the theory of potential flow applied to marine hydrodynamics. In Section 2, the Gauss-Legendre integral method has been applied to numerically evaluate the value of Green's function and its derivatives in finite water depth. In this method, the singular point of the function in the traditional integral equation can be avoided. Moreover, based on the improved Gauss-Laguerre integral method proposed in the previous research, a new methodology is developed through the Gauss-Legendre integral. Using this new methodology, Green's function with the field and source points near the water surface can be obtained, which is rarely mentioned in the previous research. The accuracy and efficiency of this new method have also been investigated. The numerical results using a Gauss-Legendre integral method show good agreements with other numerical results of direct calculations and series form in the far field. Considering the improved computational efficiency, the method using the Gauss-Legendre integral proposed in this research could obtain the accurate numerical results of Green's function and its derivatives in finite water depth and can be adopted in the near field.

The second order force of a floating structure can be expressed in terms of a time independent quadratic transfer function along with the incident wave elevation, through which it is possible to evaluate the second order wave exciting forces in the frequency

domain. Newman's approximation (Newman, 1974) has been widely applied in approximating the elements of the quadratic transfer function matrix while numerically evaluating the second order wave induced force. Through Newman's approximation, the off-diagonal elements can be numerically approximated with the diagonal elements and thus the numerical calculation efficiency can be enhanced. However, Newman's approximation assumes that the off-diagonal elements do not change significantly with the wave frequency and that only hydrodynamic phenomenon regarding the very low difference frequency are usually of interest. In Section 3, the full derivations and expression of the second order wave forces and moments applied to a floating structure are presented, through which the numerical results of the quadratic transfer function matrix including the diagonal and the off-diagonal elements are illustrated with the direct pressure integral. Through the comparison, it is found that Newman's approximation is less accurate when an element that is close to the diagonal line in the quadratic transfer function matrix shows an extremum if the corresponding wave frequency is close to the natural frequency of the certain motion. Therefore, Newman's approximation may not provide a satisfying result as the difference frequency increases. Considering this, the direct numerical evaluation of the full QTF matrix is of importance, for instance, while evaluating the 2^{nd}-order rotation motions. Moreover, the effects of water depth and difference frequency on the quadratic transfer function have also been investigated. This work provides the basis of efficiently evaluating the second order wave loads in the frequency domain. It should be noted that the 2^{nd}-order boundary value problem has not

been solved in this research. The contribution from the 2nd-order wave potential has been estimated by using Pinkster's approximation (Pinkster, 1980).

In many cases, the vessel's forward speed or current affects the 2nd-order wave loads, which is also called wave drift damping. In Section 4, Aranha's formula (Aranha, 1994), a far field method and the Neumann-Kelvin linearization (Brard, 1972; Guevel et al, 1974), a near field method have been applied and compared in a parallel study, to investigate the 2nd-order wave loads with forward speed and current. It is found that both Aranha's formula and Neumann-Kelvin linearization can provide a reasonable estimation at low Froude number. However, as the Froude number increases, the numerical results from Aranha's formula have a lack of physical meaning and the approximation meet its limitation, due to its restriction to low current speed. The Neumann-Kelvin linearization provides a more robust numerical estimation and converges to the expression of the mean 2nd-order forces and moments in our previous research when the basis flow reduces to zero.

This research involving the 2nd-order wave loads considering the effect of forward speed and current can be applied to the numerical evaluation of maneuvering in waves. Maneuvering in waves is a hydrodynamic phenomenon that involves both the seakeeping and maneuvering problems. The environmental loads, such as waves, wind, and current, have a significant impact on a maneuvering vessel, which makes it more complex than maneuvering in calm water. Wave effects are perhaps the most important factor among these environmental loads. In Section 5, a framework has been developed that simultaneously incorporates the maneuvering and seakeeping aspects that includes the

hydrodynamics effects corresponding to both. The maneuvering evaluations of the KVLCC (KRISO Very Large Crude Carrier) and KCS (KRISO Container Ship) models in calm water and waves have been conducted and compared with the model tests. Through the comparison with the experimental results, this framework had been proven to provide a convincing numerical prediction of the horizontal motions for a maneuvering vessel in regular waves. The current framework can be extended and contribute to the study of maneuvering in random waves and the IMO (International Maritime Organization) standards for determining the minimum propulsion power to maintain the maneuverability of vessels in adverse conditions.

In Section 6, with the improved hydrodynamic calculation of both 1st-order and 2nd-order hydrodynamic quantities, an optimization framework using genetic algorithms has been developed towards an automated parametric Octabuoy semi-submersible design. Compared with deep draft production units, the design of a shallow draught Octabuoy Semi-Submersible provides the floating system improved motion characteristics, while being less susceptible to vortex induced motions in loop currents. The relatively large water plane area results in the decreased natural heave period, which locates the floater in a wave period range with more wave energy. Considering this, the hull design of Octabuoy Semi-Submersible has been optimized to improve the floater's motion performance. The optimization has been conducted with optimized parameters of the pontoon's rectangular cross section area, the water surface parametric cone shaped section's height and diameter. Through the numerical evaluations of both the 1st-order and 2nd-order hydrodynamics, the

optimization using genetic algorithms has been proven to provide improved hydrodynamic performance, in terms of heave and pitch motions.

This research done for an improved wave structure interaction calculation with applications to the numerical evaluation of Green's function in shallow water, 2^{nd}-order wave loads, maneuvering in waves and floating systems hull optimization presents a meaningful framework as a reference in the process of floating system's design. This work can form the basis for additional future work including the study of maneuvering in random waves, the IMO standards for determining the minimum propulsion power to guarantee the maneuverability of vessels in adverse conditions and the optimization on the wave energy converter and the floating base of the floating wind turbine.

2. A MORE EFFICIENT NUMERICAL EVALUATION OF GREEN'S FUNCTION IN FINITE WATER DEPTH *

2.1. Introduction

The hydrodynamic motion and wave load response of offshore structures in finite water depth present different characteristics compared with those in deep water. Only when the precise solution of Green's function and its partial derivatives in finite water depth are obtained, is it possible to acquire an accurate motion response prediction of floating structures in finite water depth. Therefore, an accurate and efficient numerical evaluation of Green's function and its partial derivatives for a pulsating source in finite water depth is one of the most important aspects in the theory of potential flow applied to marine hydrodynamics. The development of fast computers makes it possible to conduct numerical calculations for three dimensional flows, which has also caused a search for expressions of Green's function in finite water depth with accurate and efficient numerical evaluation.

Noblesse (1982, 1983 and 1986) conducted the study concerned with Green's function and the general identity for the velocity potential of the potential flow theory about a body in regular waves in deep water. Using simple and global approximations

* Part of this section is reprinted with permission from "A More Efficient Numerical Evaluation of the Green Function in Finite Water Depth" by Zhitian Xie, Yuejie Liu and Jeffrey Falzarano, 2017. *Ocean Systems Engineering*, 7(4), 399-412, Copyright (2017) by Techno-Press.

involving elementary continuous functions within the entire flow region, Wu (2017) expressed Green's function of the theory of diffraction and radiation and its gradient in deep water as the sum of three components corresponding to the fundamental free-space singularity, a non-oscillatory local flow and waves. The expression for Green's function in finite water depth mainly has two forms. One is the series expression proposed by John (1950), and the other one is the integral form proposed by Wehausen and Laitone (1960). The series form presents a high computational efficiency. However, it is difficult to converge in the near field due to the existence of a singularity at R = 0, on one hand. On the other hand, the integral form presents a high accuracy but low computational efficiency in the far field. Therefore, to calculate Green's function and its partial derivatives in finite water depth, an algorithm has been proposed to utilize the integral form for the near field and the series form for the far field. For the integral form, due to the singularity in the Cauchy principal value integral and the oscillatory behavior of Bessel function, it is also one of the most challenging tasks to accurately evaluate Green's function in finite water depth. Li (2001) applied Gauss-Laguerre integration to numerically evaluate Green's function and its partial derivatives in finite water depth, which transfers the integral form to the summation form. Some results have been shown using this approach to investigate the effect of forward speed on the wave loads in restricted water depth by Guha (2016). In Li's method, the results from the Gauss-Laguerre integration are not stable in the far field and are slow to converge. Moreover, the result of Green's function with the field and source points near the water surface is not mentioned. In order to decrease the integral variable's order of the rest of the integral functions, Liu (2008) and Yang (2014) have

developed an improved Gauss-Laguerre method, using a reduced fraction to separate the parts that can be calculated by Green's function in infinite water depth. Unfortunately, the numerical results of this improved Gauss-Laguerre method may lose precision in some cases.

Therefore, this section is concerned with constructing an alternative integral method for Green's function from the theory of linearized potential flow due to a source of pulsating strength in finite water depth. Both the improved precision and computational efficiency of the Gauss-Legendre integral method proposed in this section are investigated. This work will present a meaningful reference with details to numerically evaluate the 1st-order hydrodynamic quantities and the 2nd-order wave loads on a floating structure.

2.2. Introduction of the Gauss-Laguerre Integral Method

Green's function in finite water depth can be expressed in terms of an integral as follows (Wehausen and Laitone, 1960):

$$G = \frac{1}{r} + \frac{1}{r^*} + G_{IR2} \tag{2.1}$$

Where:

$$G_{IR2} \cdot h = 2PV \int_0^\infty \frac{e^{-x} \cdot (x+Kh) \cdot \cosh(x(r_2+1)) \cdot \cosh(x(r_3+1)) \cdot J_0(xr_1)}{x \cdot \sinh(x) - Kh \cdot \cosh(x)} dx \tag{2.2}$$

$$K = \frac{\omega^2}{g} = k \cdot \tanh(kh)$$

$$r = [(x-\xi)^2 + (y-\eta)^2 + (z-\zeta)^2]^{\frac{1}{2}}$$

$$r^* = [(x-\xi)^2 + (y-\eta)^2 + (z+\zeta+2h)^2]^{\frac{1}{2}}$$

$$R = [(x-\xi)^2 + (y-\eta)^2]^{\frac{1}{2}}$$

$$r_1 = \frac{R}{h} \qquad r_2 = \frac{\zeta}{h} \qquad r_3 = \frac{z}{h}$$

$p = p(x, y, z)$ is the field point; $q = q(\xi, \eta, \zeta)$ is the source point; h is the water depth; k is the wave number. PV is the Cauchy principal value of the integral with a singularity $x_0 = k \bullet h$. J_0 indicates the first kind Bessel function with zero order.

The partial derivatives of Green's function in finite water depth can be so thus expressed as follows:

$$\frac{\partial G_{IR2}}{\partial R} . h^2 = -2PV \int_0^\infty \frac{e^{-x} \cdot x . (x+Kh) \cdot \cosh\,(x(r_2+1)) \cdot \cosh\,(x(r_3+1)) \cdot J_1(xr_1)}{x \cdot \sinh(x) - Kh \cdot \cosh\,(x)} dx \qquad (2.3)$$

$$\frac{\partial G_{IR2}}{\partial z} . h^2 = 2PV \int_0^\infty \frac{e^{-x} \cdot x . (x+Kh) \cdot \cosh\,(x(r_2+1)) \cdot \sinh\,(x(r_3+1)) \cdot J_0(xr_1)}{x \cdot \sinh(x) - Kh \cdot \cosh\,(x)} dx \qquad (2.4)$$

Considering the computational efficiency, a strategy has been proposed that the integral form can be applied when R/h $\leqslant$ 0.5 and the series form can be applied for R/h > 0.5 (Newman, 1985).

Li (2001) separated Green's function in finite water depth into two parts as follows:

$$G_{IR2} \cdot h$$

$$= 2PV \int_0^\infty e^{-x} \cdot \left[\frac{(x + Kh) \cdot \cosh\big(x(r_2 + 1)\big) \cdot \cosh\big(x(r_3 + 1)\big) \cdot J_0(xr_1)}{x \cdot \sinh(x) - Kh \cdot \cosh(x)} - \frac{(kh + Kh) \cdot \cosh\big(kh(r_2 + 1)\big) \cdot \cosh\big(kh(r_3 + 1)\big) \cdot J_0(r_1 \cdot kh)}{(x - kh) \cdot (\sinh(kh) + kh \cdot \cosh(kh) - Kh \cdot \sinh(kh))} \right] dx$$

$$- \; 2e^{-kh} Ei(kh) \frac{(kh+Kh) \cdot \cosh\big(kh(r_2+1)\big) \cdot \cosh\big(kh(r_3+1)\big) \cdot J_0(r_1 \cdot kh)}{\sinh(kh) + kh \cdot \cosh(kh) - Kh \cdot \sinh(kh)} \qquad (2.5)$$

$$PV \int_0^\infty \frac{1}{(x-a)} \cdot e^{-x} dx = -e^{-a} \cdot E_i(a) \qquad (2.6)$$

Therefore, the first part is the Cauchy principal value which can be approximated by the Gauss-Laguerre integral and the value of the second part can be calculated through the exponential integral. The Gauss-Laguerre quadrature can be expressed as follows:

$$\int_0^\infty e^{-x} f(x) dx \approx \sum_{j=1}^{N} \omega_j f(x_j) \tag{2.7}$$

Where: $x_j$is the j^{th} zero of the Laguerre polynomial $L_n(x)$ and ω_j is the weight.

The numerical results from this method are very slow to converge and may lose significant precision at high wave frequency. Liu (2008) separated the function in the Cauchy principal integral to isolate the exponential terms that cause the numerical error in the traditional Gauss-Laguerre integral method. In this scenario, the exponential term containing $e^{x(1+r_2+r_3)}$ to be integrated was particularly treated by using Green's function in infinite water depth. After that, Yang (2014) developed an improved Gauss-Laguerre integral method by handling the other exponential terms to obtain the accurate values of Green's function and its derivatives in finite water depth. This improved method could obtain the numerical value of Green's function correctly, but may lose precision in the far field and in some cases with high wave frequency.

2.3. The Gauss-Legendre Integral Method

From the previous research of Liu (2008) and Yang (2014), Green's function in finite water depth can be transformed as follows:

$$G_{IR2} \cdot h = 2PV \int_0^\infty \frac{e^{-x} \cdot (x + Kh) \cdot \cosh\left(x(r_2 + 1)\right) \cdot \cosh\left(x(r_3 + 1)\right) \cdot J_0(xr_1)}{x \cdot \sinh(x) - Kh \cdot \cosh(x)} dx$$

$$= PV \int_0^\infty \frac{(x + Kh) \cdot (e^{xr_2} + e^{x(-2-r_2)}) \cdot (e^{xr_3} + e^{x(-2-r_3)}) \cdot J_0(xr_1)}{(x - Kh) - e^{-2x}(x + Kh)} dx$$

$$= PV\int_0^{\infty}[1+\frac{2Kh+e^{-2x}(x+Kh)}{(x\cdot\tanh(x)-Kh)\cdot(1+e^{-2x})}]\cdot[e^{x(r_2+r_3)}+e^{x(-2-r_3+r_2)}$$

$$+e^{x(-2-r_2+r_3)}+\quad e^{x(-4-r_2-r_3)}]\cdot J_0(xr_1)dx \tag{2.8}$$

Considering the Bessel functions (Newman, 1984) and their integrals (Abramowitz and Stegun, 1964):

$$\int_0^{\infty}e^{-ax}J_0(bx)dx=\frac{1}{(a^2+b^2)^{0.5}}\,,\int_0^{\infty}xe^{-ax}J_0(bx)dx=\frac{a}{(a^2+b^2)^{1.5}}$$

$$\int_0^{\infty}e^{-ax}J_1(bx)dx=(1-\frac{a}{(a^2+b^2)^{0.5}})\frac{1}{b},\int_0^{\infty}xe^{-ax}J_1(bx)dx=\frac{b}{(a^2+b^2)^{1.5}} \tag{2.9}$$

Green's function and its partial derivatives can be expressed as follows:

$$G_{IR2}\cdot h\ =\frac{1}{(r_1^2+(r_2+r_3)^2)^{0.5}}+\frac{1}{(r_1^2+(2+r_3-r_2)^2)^{0.5}}+\frac{1}{(r_1^2+(2+r_2-r_3)^2)^{0.5}}+\frac{1}{(r_1^2+(4+r_2+r_3)^2)^{0.5}}+$$

$$PV\int_0^{\infty}\frac{2Kh+e^{-2x}(x+Kh)}{(x\cdot\tanh(x)-Kh)\cdot(1+e^{-2x})}\cdot[e^{x(r_2+r_3)}+e^{x(-2-r_3+r_2)}+e^{x(-2-r_2+r_3)}+$$

$$e^{x(-4-r_2-r_3)}]\cdot J_0(xr_1)dx \tag{2.10}$$

$$-\frac{\partial G_{IR2}}{\partial R}\cdot h^2=\frac{r_1}{(r_1^2+(r_2+r_3)^2)^{1.5}}+\frac{r_1}{(r_1^2+(2+r_3-r_2)^2)^{1.5}}$$

$$+\frac{r_1}{(r_1^2+(2+r_2-r_3)^2)^{1.5}}+\frac{r_1}{(r_1^2+(4+r_2+r_3)^2)^{1.5}}$$

$$+\ PV\int_0^{\infty}\frac{2Kh+e^{-2x}(x+Kh)}{(x\cdot\tanh(x)-Kh)\cdot(1+e^{-2x})}\cdot[e^{x(r_2+r_3)}$$

$$+\ e^{x(-2-r_3+r_2)}+e^{x(-2-r_2+r_3)}+e^{x(-4-r_2-r_3)}]\cdot x\cdot J_1(xr_1)dx \tag{2.11}$$

$$\frac{\partial G_{IR2}}{\partial z}\cdot h^2=\frac{-r_2-r_3}{(r_1^2+(r_2+r_3)^2)^{1.5}}-\frac{-r_2+r_3+2}{(r_1^2+(2+r_3-r_2)^2)^{1.5}}+\frac{-r_3+r_2+2}{(r_1^2+(2+r_2-r_3)^2)^{1.5}}$$

$$-\frac{4+r_2+r_3}{(r_1^2+(4+r_2+r_3)^2)^{1.5}}+\ PV\int_0^{\infty}\frac{2Kh+e^{-2x}(x+Kh)}{(x\cdot\tanh(x)-Kh)\cdot(1+e^{-2x})}\cdot[e^{x(r_2+r_3)}-$$

$$e^{x(-2-r_3+r_2)}+e^{x(-2-r_2+r_3)}-e^{x(-4-r_2-r_3)}]\cdot x\cdot J_0(xr_1)dx \tag{2.12}$$

For a Cauchy principal integral $PV\int_0^\infty\left(\frac{f(x)}{g(x)}-\frac{f(a)}{(x-a)\cdot g'(a)}\right)dx$, the point $x=a$ is the unique singularity of $\frac{f(x)}{g(x)}-\frac{f(a)}{(x-a)\cdot g'(a)}$, whose limitation at this point is $\frac{2f'(a)g'(a)-g''(a)f(a)}{2(g'(a))^2}$ obtained through l'Hôpital's Rule. Therefore, the integral with the integration interval from 0 to infinity can be divided into two integrals with finite integration intervals:

$$\int_0^\infty F(x)dx=\int_0^a F(x)dx+\int_0^{\frac{1}{a}}F(1/x)\cdot x^{-2}dx \tag{2.13}$$

The Gauss-Legendre integration formula is applied to approximate the integral with a finite integration interval as follows:

$$\int_a^{\mathrm{b}} f(y)dy\approx\frac{b-a}{2}\sum_{j=1}^{N}\omega_j f(y_j),\ \ y_j=\left(\frac{b-a}{2}\right)x_j+\frac{b+a}{2} \tag{2.14}$$

$x_j$is the j^{th} zero of the Legendre polynomial $P_n(x)$, $P_n(1)=1$. $\omega_j=2/\left(1-x_j^2\right)[P_n'(x_j)]^2$.

According to the definition, the term r_2+r_3 is from -2 to 0, while $-2\pm r_3-(\pm r_2)$ and $-2-r_3-r_2$ are from -3 to -1 and -4 to -2, respectively. When the field point and the source point are both close to the water surface, namely r_2+r_3 is from -0.2 to 0, the exponential term $e^{x(r_2+r_3)}$ converges much slower than the other three exponential terms. In this scenario, the integral with $e^{x(r_2+r_3)}$ is handled specially through Green's function in infinite water depth to leave the Bessel function in the integral to help the whole function $\left(\frac{f(x)}{g(x)}-\frac{f(a)}{(x-a)\cdot g'(a)}\right)\cdot e^{x(r_2+r_3)}\cdot J_0(xr_1)$ converge faster. Therefore, fewer zero points of the Legendre polynomial are needed to evaluate the integral with a certain accuracy, which contributes to a higher computational efficiency. The integral with

$e^{x(-2-r_3+r_2)} + e^{x(-2-r_2+r_3)} + e^{x(-4-r_2-r_3)}$ is evaluated by substituting Bessel function into the function $f(x)$, since the function $\left(\frac{f(x)}{g(x)} - \frac{f(a)}{(x-a)\cdot g'(a)}\right) \cdot (e^{x(-2-r_3+r_2)} + e^{x(-2-r_2+r_3)} + e^{x(-4-r_2-r_3)})$ itself converges fast enough. Therefore, the expressions of the integral forms are as follows:

For the integral containing $e^{x(r_2+r_3)}$:

$$PV \int_0^\infty \frac{f(x)}{g(x)} \cdot e^{x(r_2+r_3)} \cdot J_0(xr_1)dx$$

$$= PV \int_0^\infty \left(\frac{f(x)}{g(x)} - \frac{f(a)}{(x-a)\cdot g'(a)}\right) \cdot \ e^{x(r_2+r_3)} \cdot J_0(xr_1)dx$$

$$+ \frac{f(a)}{g'(a)} \cdot \ PV \int_0^\infty \frac{1}{(x-a)} \cdot e^{x(r_2+r_3)} \cdot J_0(xr_1)dx \qquad (2.15)$$

Where:

$$f(x) = 2Kh + e^{-2x}(x + Kh)$$

$$g(x) = (x \cdot \tanh(x) - Kh) \cdot (1 + e^{-2x})$$

$PV \int_0^\infty \frac{1}{(x-a)} \cdot e^{xr} \cdot J_0(xr_1)dx$ can be evaluated from Green's function in infinite water depth (Wang, 1992).

For the integral containing $e^{x(-2-r_3+r_2)} + e^{x(-2-r_2+r_3)} + e^{x(-4-r_2-r_3)}$:

$$PV \int_0^\infty \frac{f(x)}{g(x)} \cdot (e^{x(-2-r_3+r_2)} + e^{x(-2-r_2+r_3)} + e^{x(-4-r_2-r_3)})dx$$

$$= PV \int_0^\infty \left(\frac{f(x)}{g(x)} - \frac{f(a)}{(x-a)\cdot g'(a)}\right) \cdot \ (e^{x(-2-r_3+r_2)} + e^{x(-2-r_2+r_3)} + e^{x(-4-r_2-r_3)})\, dx$$

$$+ \frac{f(a)}{g'(a)} \cdot PV \int_0^\infty \frac{1}{(x-a)} \cdot (e^{x(-2-r_3+r_2)} + \ e^{x(-2-r_2+r_3)} + e^{x(-4-r_2-r_3)})dx \qquad (2.16)$$

Where:

$$PV\int_0^{\infty}\frac{1}{(x-a)}\cdot e^{-x}dx=-e^{-a}\cdot E_i(a)$$

$$f(x)=(2Kh+e^{-2x}(x+Kh))\cdot J_0(xr_1)$$

$$g(x)=(x\cdot\tanh(x)-Kh)\cdot(1+e^{-2x})$$

Similarly, the integral forms of Green's function's partial derivatives can be obtained.

$\frac{\partial G_{IR2}}{\partial R}\cdot h^2$, for the integral containing $e^{x(r_2+r_3)}$:

$$PV\int_0^{\infty}\frac{f(x)}{g(x)}\cdot e^{x(r_2+r_3)}\cdot x\cdot J_1(xr_1)dx$$

$$=PV\int_0^{\infty}\left(\frac{f(x)}{g(x)}-\frac{f(a)}{(x-a)\cdot g'(a)}\right)\cdot e^{x(r_2+r_3)}\cdot\ x\cdot J_1(xr_1)dx$$

$$+\ \frac{f(a)}{g'(a)}\cdot PV\int_0^{\infty}\frac{x}{(x-a)}\cdot e^{x(r_2+r_3)}\cdot J_1(xr_1)dx \qquad (2.17)$$

Where:

$$f(x)=2Kh+e^{-2x}(x+Kh)$$

$$g(x)=(x\cdot\tanh(x)-Kh)\cdot(1+e^{-2x})$$

For the integral containing $e^{x(-2-r_3+r_2)}+e^{x(-2-r_2+r_3)}+e^{x(-4-r_2-r_3)}$:

$$PV\int_0^{\infty}\frac{f(x)}{g(x)}\cdot(e^{x(-2-r_3+r_2)}+e^{x(-2-r_2+r_3)}+e^{x(-4-r_2-r_3)})dx$$

$$=PV\int_0^{\infty}\left(\frac{f(x)}{g(x)}-\frac{f(a)}{(x-a)\cdot g'(a)}\right)\cdot(e^{x(-2-r_3+r_2)}+e^{x(-2-r_2+r_3)}+e^{x(-4-r_2-r_3)})\,dx$$

$$+\frac{f(a)}{g'(a)}\cdot PV\int_0^{\infty}\frac{1}{(x-a)}\cdot(e^{x(-2-r_3+r_2)}+e^{x(-2-r_2+r_3)}+e^{x(-4-r_2-r_3)})dx \qquad (2.18)$$

Where:

$$f(x)=(2Kh+e^{-2x}(x+Kh))\cdot x\cdot J_1(xr_1)$$

$$g(x) = (x \cdot \tanh(x) - Kh) \cdot (1 + e^{-2x})$$

$\frac{\partial G_{IR2}}{\partial z} \cdot h^2$, for the integral containing $e^{x(r_2+r_3)}$:

$$PV \int_0^\infty \frac{f(x)}{g(x)} \cdot e^{x(r_2+r_3)} \cdot x \cdot J_0(xr_1)dx$$

$$= PV \int_0^\infty \left(\frac{f(x)}{g(x)} - \frac{f(a)}{(x-a) \cdot g'(a)}\right) \cdot e^{x(r_2+r_3)} \cdot x \cdot J_0(xr_1)dx$$

$$+ \frac{f(a)}{g'(a)} \cdot PV \int_0^\infty \frac{x}{(x-a)} \cdot e^{x(r_2+r_3)} \cdot J_0(xr_1)dx \quad (2.19)$$

Where:

$$f(x) = 2Kh + e^{-2x}(x + Kh)$$

$$g(x) = (x \cdot \tanh(x) - Kh) \cdot (1 + e^{-2x})$$

For the integral containing $e^{x(-2-r_3+r_2)} + e^{x(-2-r_2+r_3)} + e^{x(-4-r_2-r_3)}$:

$$PV \int_0^\infty \frac{f(x)}{g(x)} \cdot (-e^{x(-2-r_3+r_2)} + e^{x(-2-r_2+r_3)} - e^{x(-4-r_2-r_3)})dx$$

$$= PV \int_0^\infty \left(\frac{f(x)}{g(x)} - \frac{f(a)}{(x-a) \cdot g'(a)}\right) \cdot (-e^{x(-2-r_3+r_2)} + e^{x(-2-r_2+r_3)} - e^{x(-4-r_2-r_3)})\, dx$$

$$+ \frac{f(a)}{g'(a)} \cdot PV \int_0^\infty \frac{1}{(x-a)} \cdot (-e^{x(-2-r_3+r_2)} + e^{x(-2-r_2+r_3)} - e^{x(-4-r_2-r_3)})dx \quad (2.20)$$

Where:

$$f(x) = (2Kh + e^{-2x}(x + Kh)) \cdot x \cdot J_0(xr_1)$$

$$g(x) = (x \cdot \tanh(x) - Kh) \cdot (1 + e^{-2x})$$

Therefore, Green's function and its partial derivatives in finite water depth can be expressed as the summation of the special functions (Ei and Green's function in infinite water depth) and integrals through the Gauss-Legendre integral method.

2.4. Results and Discussion

Green's function and its partial derivatives in finite water depth can be regarded as functions of kh, R/h, z/h and ζ/h. The values of Green's function and its partial derivatives through the Gauss-Legendre integral method are compared with those from direct integral calculation using Romberg's (Romberg, 1955) method and series form both in the near field and far field to verify the accuracy of the new method proposed in this paper. The numerical calculations with two different wave frequencies (kh = 0.46268 and 2.06534) are conducted. Moreover, the cases with the field and source points near the water surface are also considered as a comparison with the cases with the field point near the bottom.

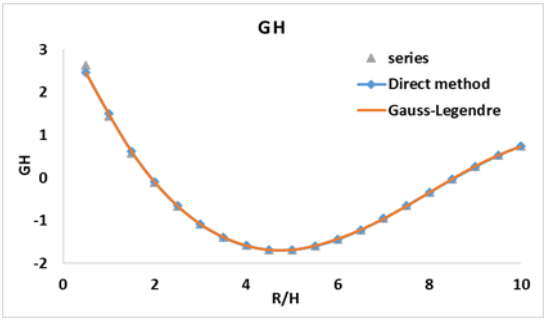

(a) Gh

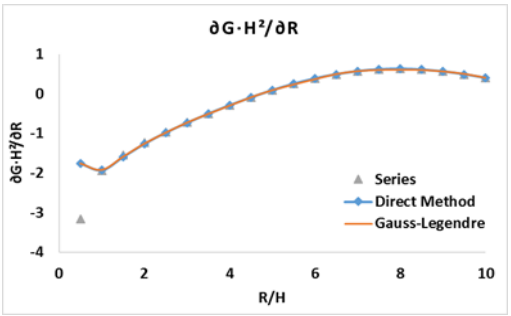

(b) $\frac{\partial G}{\partial R} \cdot h^2$

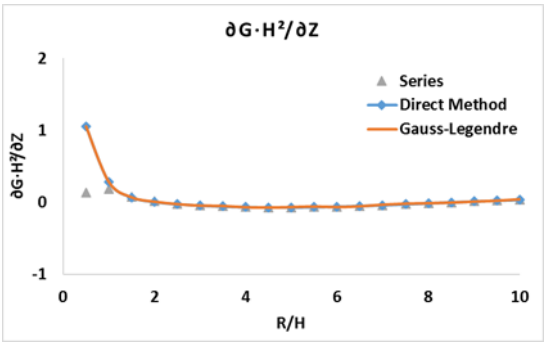

(c) $\frac{\partial G}{\partial z} \cdot h^2$

Figure 2.1. Green's function and its derivatives (kh = 0.46268, $\zeta/h = 0$, z/h = -0.80 for (c), z/h = -1 for (a) and (b)).

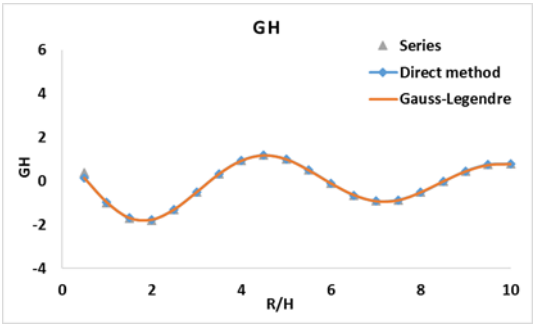

(a) Gh

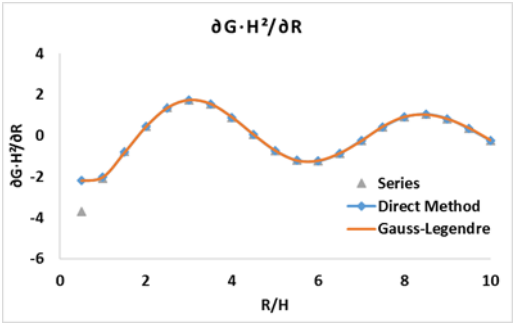

(b) $\frac{\partial G}{\partial R} \cdot h^2$

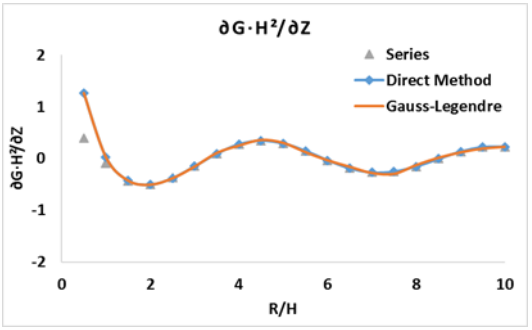

(c) $\frac{\partial G}{\partial z} \cdot h^2$

Figure 2.2. Green's function and its derivatives (kh = 1.19968, $\zeta/h = 0$, z/h = -0.80 for (c), z/h = -1 for (a) and (b)).

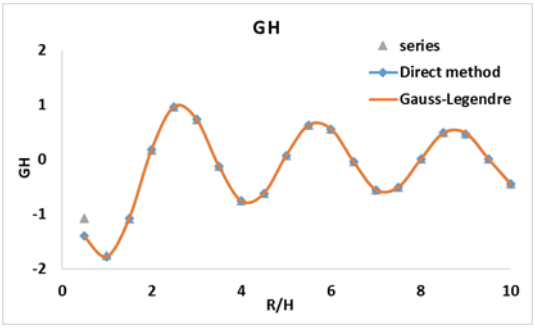

(a) Gh

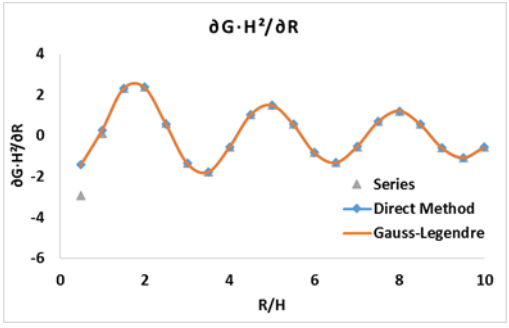

(b) $\frac{\partial G}{\partial R} \cdot h^2$

Figure 2.3. Green's function and its derivatives (kh = 2.06534, $\zeta/h = 0$, z/h = -0.80 for (c), z/h = -1 for (a) and (b)).

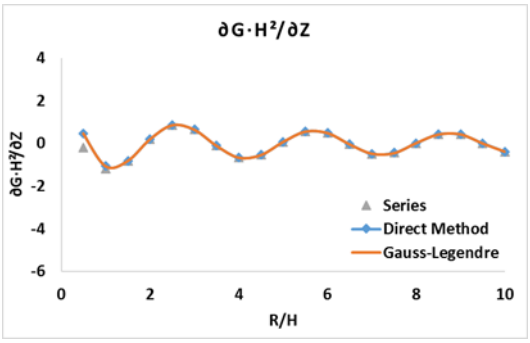

(c) $\frac{\partial G}{\partial z} \cdot h^2$

Figure 2.3. Continued.

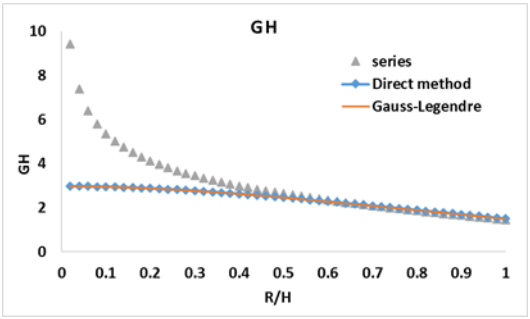

(a) Gh

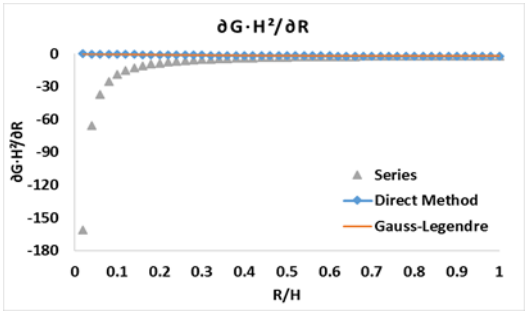

(b) $\frac{\partial G}{\partial R} \cdot h^2$

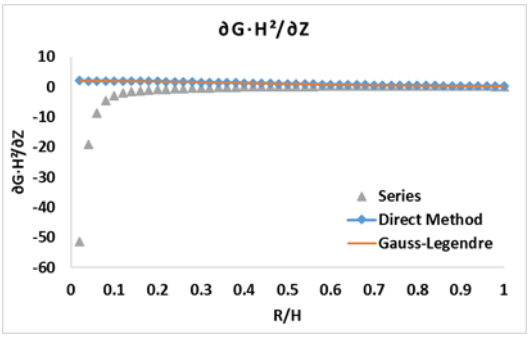

(c) $\frac{\partial G}{\partial z} \cdot h^2$

Figure 2.4. Green's function and its derivatives (Zoom in for **Figure 2.1**).

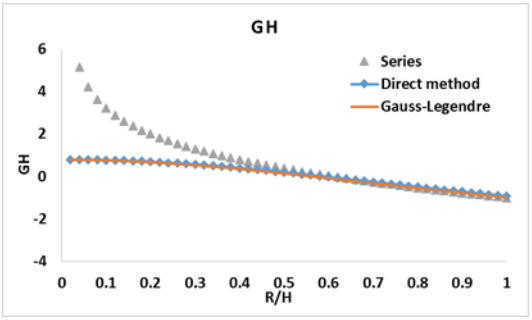

(a) Gh

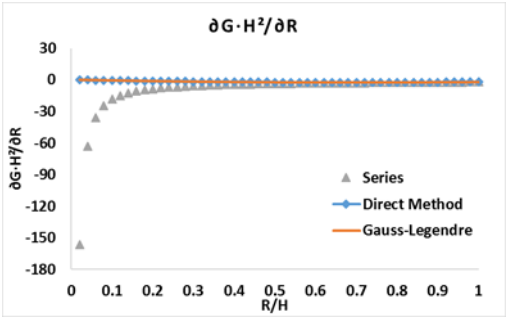

(b) $\frac{\partial G}{\partial R} \cdot h^2$

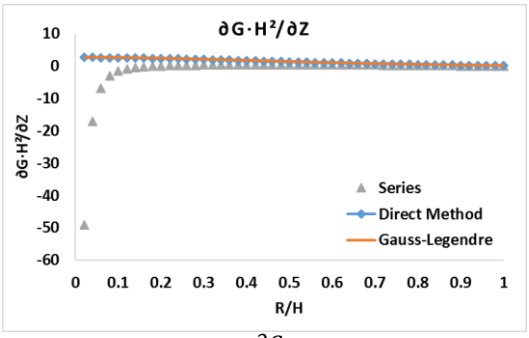

(c) $\frac{\partial G}{\partial z} \cdot h^2$

Figure 2.5. Green's function and its derivatives (Zoom in for **Figure 2.2**).

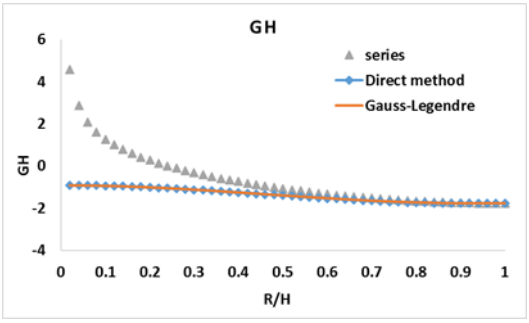

(a) Gh

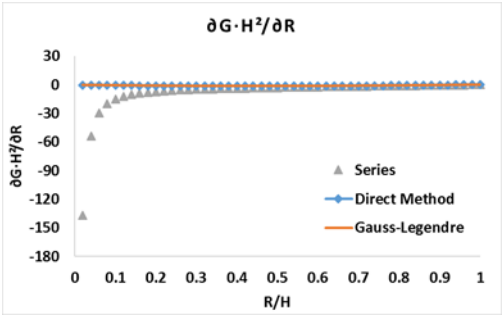

(b) $\frac{\partial G}{\partial R} \cdot h^2$

Figure 2.6. Green's function and its derivatives (Zoom in for **Figure 2.3**).

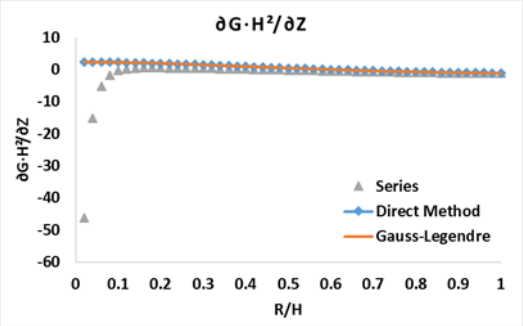

(c) $\frac{\partial G}{\partial z} \cdot h^2$

Figure 2.6. Continued.

Figures 2.1 to 2.3 present the numerical results of the cases with field points near the bottom of the water. Since the value of $\partial G/\partial z$ is always 0 when $z/h = -1$, thus $z/h = -0.8$ is chosen to present the numerical results of $\partial G/\partial z$. The numerical results through the Gauss-Legendre integral method show good agreements with the direct calculations using Romberg's method in both the near field and far field, which present an accurate numerical result. The results of the series form have a good coincidence with those from the Gauss-Legendre integral and direct integral calculation with high computational efficiency, but lose precision in the near field when R/h <1. As there are totally 20 zero points of Legendre polynomial applied to numerically evaluate Green's function and its derivatives in finite water depth, the Gauss-Legendre integral method presents a high computational efficiency in this scenario.

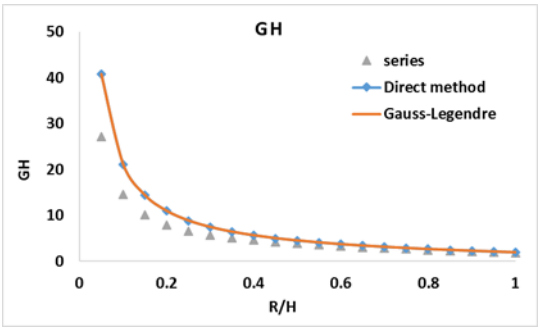

(a) Gh

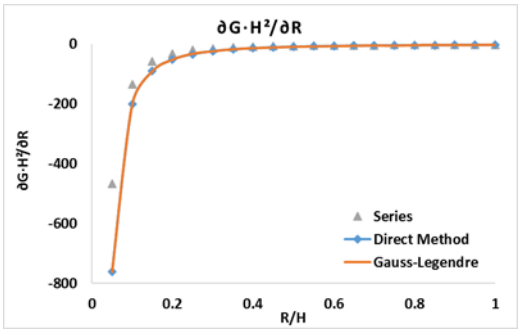

(b) $\frac{\partial G}{\partial R} \cdot h^2$

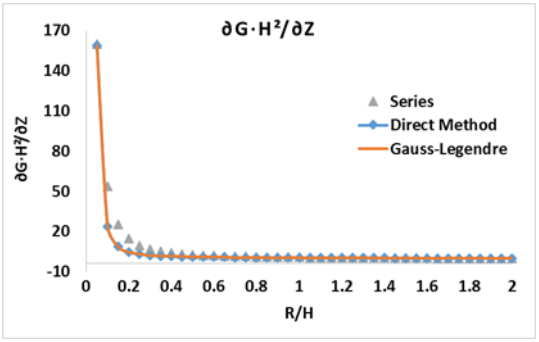

(c) $\frac{\partial G}{\partial z} \cdot h^2$

Figure 2.7. Green's function and its derivatives (kh = 0.46268, $\zeta/h = 0$, z/h = -0.01).

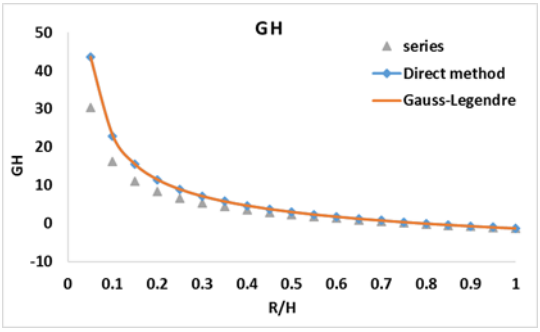

(a) Gh

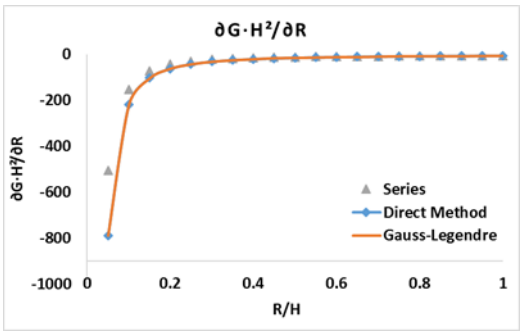

(b) $\frac{\partial G}{\partial R} \cdot h^2$

Figure 2.8. Green's function and its derivatives (kh = 1.19968, $\zeta/h = 0$, z/h = -0.01).

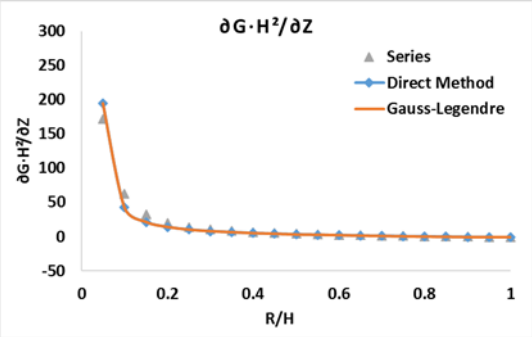

(c) $\frac{\partial G}{\partial z} \cdot h^2$

Figure 2.8. Continued.

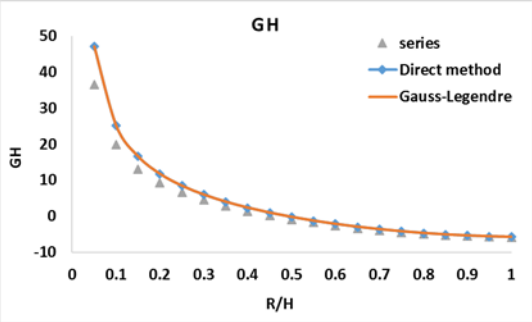

(a) Gh

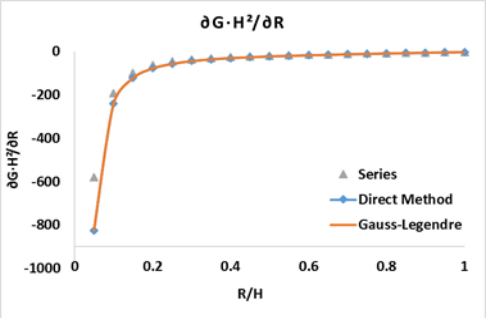

(b) $\frac{\partial G}{\partial R} \cdot h^2$

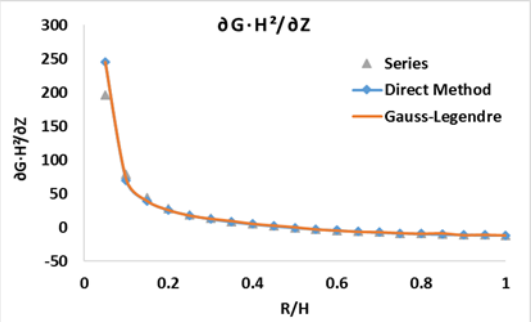

(c) $\frac{\partial G}{\partial z} \cdot h^2$

Figure 2.9. Green's function and its derivatives (kh = 2.06534, $\zeta/h = 0$, z/h = -0.01).

Figures 2.7 to 2.9 present the numerical results of the cases with field points near the water surface. The numerical results of the Gauss-Legendre integral method agree well with that of direct integral method using Romberg's method in both the near field and far field. As R/h increases, the difference between the results of series form and the other two methods decreases. It should be noted that there are about 100 zero points of the Legendre polynomial applied for the Gauss-Legendre integral method in the water surface case. One reason is that when the field point and source point are both close enough to the water surface, $e^{x(r_2+r_3)}$ mentioned previously converges slowly as x tends to positive infinity. Therefore, there are more Legendre polynomial zero points needed to accurately evaluate the second Gauss-Legendre integral. Through investigation, it can be concluded that less than 20 Legendre polynomial zero points are needed for $r_2 + r_3 \leq -0.2$, 50 points for $-0.2 < r_2 + r_3 \leq -0.05$ and about 100 points are needed for $-0.05 < r_2 + r_3 \leq -0$ to promise the numerical accuracy. Further investigation is needed in this scenario to evaluate Green's function and its derivatives with field point and source point extremely close to the water surface with a higher computational efficiency. The Gauss-Legendre integral method is practical to evaluate Green's function and its partial derivatives in finite water depth in the near field ($R/h \leq 1$) with a high computational efficiency, combined with series form in the far field ($R/h > 1$).

2.5. Conclusion

Green's function and its partial derivatives in finite water depth are numerically evaluated in this research to predict the hydrodynamic motion and load response of offshore structures. The Gauss-Legendre integral method is applied to evaluate the integral

form of Green's function, whose numerical results are compared with those of other numerical methods. By applying the Gauss-Legendre method to the in-house code (MDLHydroD), it takes 801 seconds to numerically evaluate the 1st-order hydrodynamic quantities of a vertical cylinder (with 1048 panels, 122 wave frequencies and 1 incident wave direction) with the water depth of 25 meters by using single core of Intel(R) Xeon(R) CPU E3-1225v3@3.2GHz with 16 GB RAM, while it takes 5880 seconds to complete the numerical calculation with the same configuration through the Gauss-Laguerre method in MDLHydroD. In this scenario, the integral method applied with the Gauss-Legendre presents an over 6 times increased numerical efficiency in calculating Green's function and its derivatives in finite water depth, compared with the Gauss-Laguerre method.

The results of the Gauss-Legendre method show a good agreement (within 0.001 percent discrepancy) with the direct integral method in both the near field. The computational efficiency of the case with the field point near the water bottom is higher than that of the case with the field point near the free surface, due to the convergence of the exponential term. It is found that the series form presents a high accuracy and computational efficiency in the far field, but loses precision in the near field.

Considering the computational efficiency and accuracy, it is suggested in this research to apply the Gauss-Legendre integral method while $R/h \leq 1$ and the series form while $R/h > 1$ to numerically evaluate Green's function and its derivatives in finite water depth. This provides the numerical basis in the 1st-order quantities for the higher order wave loads that will be introduced in the next section.

3. NUMERICAL EVALUATION OF THE QUADRATIC TRANSFER FUNCTION OF A FLOATING STRUCTURE*

3.1. Introduction

The knowledge of the 2nd-order wave loads along with various incident wave frequencies is the basis of numerically evaluating the slow-drift motion of a floating structure. Wave basin tests in regular waves and analytical investigations through the numerical evaluation of the 2nd-order wave loads have been conducted in the previous research (See e.g. Newman, 1974; Kim and Yue, 1990; Zhao et al, 2012). In the wave basin model tests, special attention has to be given to measure the low frequency 2nd-order force. When measuring the low frequency 2nd-order force, the model undergoes motions with frequencies that coincide with the frequencies of the 2nd-order forces. The constraint of the designed system must allow the model to move freely at wave frequencies while at the same time the 2nd-order low frequency motions corresponding to the low frequency wave drift force must be fully suppressed.

The 2nd-order mean drift forces have a significant impact on the stability criteria and integrity for the floating bogies and the mooring system design (See e. g. Masuda et al, 2002; Munipalli,et al, 2007; Wichers, 2001). To numerically evaluate the 2nd-order

* Part of this section is reprinted with permission from "A Numerical Evaluation of the Quadratic Transfer Function for a Floating Structure" by Zhitian Xie, Yuejie Liu and Jeffrey Falzarano, 2019. *Proceedings of the ASME 2019 38th International Conference on Ocean, Offshore and Arctic Engineering*, Copyright (2019) by ASME Publishing.

mean drift loads, there are two main methods: the far field method (Maruo, 1960) based on diffracted and radiated wave energy and the momentum flux at infinity and the near field method (See e.g. Boese, 1970; Pinkster, 1979). Compared with the far field method that provide forces in 3 DOF, the near field method is more intuitive and can provide forces in 6 DOF. In the analytical research, the numerical evaluation of the quadratic transfer function (QTF) is worth pursuing, through which the mean drift force in the irregular waves or regular waves can be approximated with the diagonal elements in the QTF matrix. While evaluating the 2nd-order wave drift force and moment, Newman's approximation has been widely applied in approximating the off-diagonal elements through the already obtained diagonal elements in the QTF matrix. The hydrodynamic phenomenon in irregular waves with relatively close wave frequencies, namely, the low difference frequency is usually of interest while considering the massive structures with low natural frequencies in the horizontal modes of motions. The off-diagonal elements corresponding to the low difference frequency in the QTF matrix are close to the diagonal line and thus do not change significantly with the wave frequency. If this is true, Newman's approximation can significantly enhance the computational efficiency.

However, when an element in the QTF matrix is close to the diagonal line it presents an extremum. The results from the Newman's approximation become less accurate. The extremums occur for instance along the diagonal line if $\omega_{j(k)}$ in $\omega_j - \omega_k$ is close to the natural frequency of the heave motion while at some time the heave damping is low. Moreover, as the difference frequency increases or as the water depth decreases, Newman's approximation may not provide a satisfying result, either. For instance, it is not

applicable when evaluating the 2nd-order roll motions. Therefore, the direct numerical evaluation of the full QTF matrix is necessary in many general cases.

The full expression of the 2nd-order force and moment through the near field method involve the 1st-order quantities including the floating structure's motion and the 2nd-order quantities including the 2nd-order wave potential with difference frequencies and summation frequencies. The 2nd-order incident wave potential with difference wave frequency $\Phi_I^{(2-)}$, especially for small difference frequencies, penetrates deeper into the field than the 2nd-order incident wave potential with summation of frequencies, $\Phi_I^{(2+)}$. This character for $\Phi_I^{(2-)}$ in narrow banded seas is of importance to deep-draft bodies.

In this section, the derivation and expression of the 2nd-order wave loads applied to a floating structure have been presented in the 1st-order and 2nd-order quantities, through which the numerical results of the QTF matrix including the diagonal and the off-diagonal elements of a vertical cylinder will be illustrated. This work presents a basis of numerically evaluating the second order forces in the frequency domain.

3.2. Coordinate Transformation and the Perturbation Theory

A point fixed on the floating structure's surface can be presented both in the global coordinate and the vessel-fixed coordinate system. Assuming small amplitudes of the floating structure's angular motion, the transformation between the global coordinate and the vessel-fixed coordinate can be presented as:

$$\boldsymbol{X} - \boldsymbol{X_0} = \boldsymbol{\eta} + \boldsymbol{X'} + \boldsymbol{\alpha} \times \boldsymbol{X'} + \varepsilon^2 \boldsymbol{H X'} \tag{3.1}$$

$$\boldsymbol{n} = \boldsymbol{n'} + \boldsymbol{\alpha} \times \boldsymbol{n'} + \varepsilon^2 \boldsymbol{H n'} \tag{3.2}$$

Through the perturbation theory, the wave pressure, the normal vector, the floating structure's motions, the wave potential and the wave elevation can be developed into the form of the summations of different orders:

$$p = p^{(0)} + \varepsilon p^{(1)} + \varepsilon^2 p^{(2)} + o(\varepsilon^3) \tag{3.3}$$

$$\boldsymbol{n} = \boldsymbol{n}^{(0)} + \varepsilon \boldsymbol{n}^{(1)} + \varepsilon^2 \boldsymbol{n}^{(2)} + \boldsymbol{o}(\varepsilon^3) \tag{3.4}$$

$$\boldsymbol{\eta} = \varepsilon \boldsymbol{\eta}^{(1)} + \varepsilon^2 \boldsymbol{\eta}^{(2)} + \boldsymbol{o}(\varepsilon^3) \tag{3.5}$$

$$\boldsymbol{\alpha} = \varepsilon \boldsymbol{\alpha}^{(1)} + \varepsilon^2 \boldsymbol{\alpha}^{(2)} + \boldsymbol{o}(\varepsilon^3) \tag{3.6}$$

$$\Phi = \varepsilon \Phi^{(1)} + \varepsilon^2 \Phi^{(2)} + o(\varepsilon^3) \tag{3.7}$$

$$\zeta = \varepsilon \zeta^{(1)} + \varepsilon^2 \zeta^{(2)} + o(\varepsilon^3) \tag{3.8}$$

Through the coordinate transformation, it can be expressed:

$$\boldsymbol{X} - \boldsymbol{X}' - \boldsymbol{X_0} = \varepsilon\left(\boldsymbol{\eta}^{(1)} + \boldsymbol{\alpha}^{(1)} \times \boldsymbol{X}'\right) + \varepsilon^2(\boldsymbol{\eta}^{(2)} + \boldsymbol{\alpha}^{(2)} \times \boldsymbol{X}' + \boldsymbol{H}\boldsymbol{X}') \tag{3.9}$$

$$\Phi|_S = \Phi|_{S_M} + [(\boldsymbol{X} - \boldsymbol{X}' - \boldsymbol{X_0}).\boldsymbol{\nabla}]\Phi|_{S_M} + o(\varepsilon^3) \tag{3.10}$$

Therefore:

$$\begin{aligned} \Phi|_S &= \varepsilon\Phi^{(1)}|_S + \varepsilon^2\Phi^{(2)}|_S + o(\varepsilon^3) \\ &= \Phi|_{S_M} + [(\boldsymbol{X} - \boldsymbol{X}' - \boldsymbol{X_0}).\boldsymbol{\nabla}]\Phi|_{S_M} + o(\varepsilon^3) \\ &= \varepsilon\Phi^{(1)}|_{S_M} + \varepsilon^2\Phi^{(2)}|_{S_M} \\ &\quad + \varepsilon^2\left[\left(\boldsymbol{\eta}^{(1)} + \boldsymbol{\alpha}^{(1)} \times \boldsymbol{X}'\right).\boldsymbol{\nabla}\right]\Phi^{(1)}|_{S_M} + o(\varepsilon^3) \end{aligned} \tag{3.11}$$

By applying the Bernoulli equation,

$$p = -\rho(gz + \frac{\partial \Phi}{\partial t} + \frac{1}{2}\boldsymbol{\nabla}\Phi.\boldsymbol{\nabla}\Phi) \tag{3.12}$$

The pressure on the floating structure can be expressed as:

$$
\begin{aligned}
p|_S \;&= -\rho\left(gz + \frac{\partial \Phi}{\partial t} + \frac{1}{2}\boldsymbol{\nabla}\Phi.\boldsymbol{\nabla}\Phi\right)|_{S_M} \\
&+(\boldsymbol{X} - \boldsymbol{X}' - \boldsymbol{X_0}).\boldsymbol{\nabla}[-\rho\left(gz + \frac{\partial \Phi}{\partial t} + \frac{1}{2}\boldsymbol{\nabla}\Phi.\boldsymbol{\nabla}\Phi\right)]|_{S_M} \\
&= -\rho\left(gz + \varepsilon\frac{\partial \Phi^{(1)}}{\partial t} + \varepsilon^2\frac{\partial \Phi^{(2)}}{\partial t} + \varepsilon^2\frac{1}{2}\boldsymbol{\nabla}\Phi^{(1)}.\boldsymbol{\nabla}\Phi^{(1)}\right)|_{S_M} \\
&+\left(\varepsilon\left(\boldsymbol{\eta^{(1)}} + \boldsymbol{\alpha^{(1)}} \times \boldsymbol{X'}\right) + \varepsilon^2\left(\boldsymbol{\eta^{(2)}} + \boldsymbol{\alpha^{(2)}} \times \boldsymbol{X'} + \boldsymbol{HX'}\right)\right). \\
&\boldsymbol{\nabla}[-\rho\left(gz + \varepsilon\frac{\partial \Phi^{(1)}}{\partial t} + \varepsilon^2\frac{\partial \Phi^{(2)}}{\partial t}\right)]|_{S_M}
\end{aligned} \tag{3.13}
$$

Therefore, by collecting the ε^0, ε and ε^2 terms, the wave pressure can be obtained in different orders:

$$
p^{(0)}|_S = -\rho g z|_{S_M} \tag{3.14}
$$

$$
p^{(1)}|_S = -[\rho\frac{\partial \Phi^{(1)}}{\partial t} + \rho g\boldsymbol{k}.\left(\boldsymbol{\eta^{(1)}} + \boldsymbol{\alpha^{(1)}} \times \boldsymbol{X'}\right)]|_{S_M} \tag{3.15}
$$

$$
\begin{aligned}
p^{(2)}|_S \;&= -[\rho\frac{\partial \Phi^{(2)}}{\partial t} + \frac{1}{2}\rho\boldsymbol{\nabla}\Phi^{(1)}.\boldsymbol{\nabla}\Phi^{(1)} \\
&+\rho g\boldsymbol{k}.\left(\boldsymbol{\eta^{(2)}} + \boldsymbol{\alpha^{(2)}} \times \boldsymbol{X'} + \boldsymbol{HX'}\right) \\
&+\left(\rho\frac{\partial}{\partial t}\boldsymbol{\nabla}\Phi^{(1)}\right).(\boldsymbol{\eta^{(1)}} + \boldsymbol{\alpha^{(1)}} \times \boldsymbol{X'})]|_{S_M}
\end{aligned} \tag{3.16}
$$

Similarly, the normal vector of the floating structure's wetted surface pointing into the fluid field can also be expressed in both global and vessel-fixed coordinate:

$$
\begin{aligned}
\boldsymbol{n} &= \boldsymbol{n'} + \boldsymbol{\alpha} \times \boldsymbol{n'} + \varepsilon^2\boldsymbol{Hn'} \\
&= \boldsymbol{n'} + \left(\varepsilon\boldsymbol{\alpha^{(1)}} + \varepsilon^2\boldsymbol{\alpha^{(2)}}\right) \times \boldsymbol{n'} + \varepsilon^2\boldsymbol{Hn'} \\
&= \boldsymbol{n^{(0)}} + \varepsilon\boldsymbol{n^{(0)}} + \varepsilon^2\boldsymbol{n^{(0)}}
\end{aligned} \tag{3.17}
$$

Therefore, normal vector can be obtained in different orders:

$$\boldsymbol{n}^{(\mathbf{0})} = \boldsymbol{n}' \tag{3.18}$$

$$\boldsymbol{n}^{(\mathbf{1})} = \boldsymbol{\alpha}^{(\mathbf{1})} \times \boldsymbol{n}' \tag{3.19}$$

$$\boldsymbol{n}^{(\mathbf{2})} = \boldsymbol{\alpha}^{(\mathbf{2})} \times \boldsymbol{n}' + \boldsymbol{H}\boldsymbol{n}' \tag{3.20}$$

3.3. The Derivation of the Second Order Force

In the previous sections, the wave pressure through the Bernoulli equation and the normal vectors have been obtained through the perturbation form in different orders, thus the direct integral of the wave pressure over the floating structure's surface can be developed to derive the wave forces in the corresponding orders.

$$\boldsymbol{F} = \boldsymbol{F}^{(\mathbf{0})} + \varepsilon\boldsymbol{F}^{(\mathbf{1})} + \varepsilon^2\boldsymbol{F}^{(\mathbf{2})} = -\iint_S \; p\boldsymbol{n}dS = -\iint_{S_M} p\boldsymbol{n}dS - \iint_{\Delta S} p\boldsymbol{n}dS \tag{3.21}$$

$$\begin{aligned} p\boldsymbol{n} \;\; &= p^{(0)}\boldsymbol{n}^{(0)} + \varepsilon\left(p^{(1)}\boldsymbol{n}^{(0)} + p^{(0)}\boldsymbol{n}^{(1)}\right) \\ &+\varepsilon^2\left(p^{(2)}\boldsymbol{n}^{(0)} + p^{(0)}\boldsymbol{n}^{(2)} + p^{(1)}\boldsymbol{n}^{(1)}\right) \end{aligned} \tag{3.22}$$

Therefore, the forces in the global coordinate in different orders can be expressed as:

$$\boldsymbol{F}^{(\mathbf{0})} \;\; = -\iint_{S_M} p^{(0)}\boldsymbol{n}^{(0)}\, dS = \iint_{S_M} \rho g z\boldsymbol{n}'\, dS \tag{3.23}$$

$$\begin{aligned} \boldsymbol{F}^{(\mathbf{1})} \;\; &= -\iint_{S_M} \left(p^{(1)}\boldsymbol{n}^{(\mathbf{0})} + p^{(0)}\boldsymbol{n}^{(\mathbf{1})}\right) dS \\ &= \iint_{S_M} [\rho g z\boldsymbol{\alpha}^{(\mathbf{1})} \times \boldsymbol{n}' \\ &\quad + \left(\rho\frac{\partial\Phi^{(1)}}{\partial t} + \rho g\left(\eta_3^{(1)} + \eta_4^{(1)}x_2' - \eta_5^{(1)}x_1'\right)\right)\boldsymbol{n}'] \, dS \end{aligned} \tag{3.24}$$

$$\boldsymbol{F}^{(\mathbf{2})} \;\; = -\iint_{S_M} \left(p^{(2)}\boldsymbol{n}^{(0)} + p^{(0)}\boldsymbol{n}^{(2)} + p^{(1)}\boldsymbol{n}^{(1)}\right) dS$$

$$-\frac{1}{2}\rho g \int_{WL} {\zeta_r^{(1)}}^2 \boldsymbol{n}'\, dl$$

$$= \iint_{S_M} [\rho g z\left(\boldsymbol{\alpha}^{(2)} \times \boldsymbol{n}' + \boldsymbol{H}\boldsymbol{n}'\right)$$

$$+\left(\rho \frac{\partial \Phi^{(1)}}{\partial t} + \rho g \begin{pmatrix} \eta_3^{(1)} + \eta_4^{(1)} x_2' \\ -\eta_5^{(1)} x_1' \end{pmatrix}\right)\begin{pmatrix} \boldsymbol{\alpha}^{(1)} \\ \times \boldsymbol{n}' \end{pmatrix}$$

$$+\rho(\frac{\partial \Phi^{(2)}}{\partial t} + \frac{1}{2}\boldsymbol{\nabla}\Phi^{(1)}.\boldsymbol{\nabla}\Phi^{(1)}$$

$$+ g\boldsymbol{k}.\left(\boldsymbol{\eta}^{(2)} + \boldsymbol{\alpha}^{(2)} \times \boldsymbol{X}' + \boldsymbol{H}\boldsymbol{X}'\right)$$

$$+(\frac{\partial}{\partial t}\boldsymbol{\nabla}\Phi^{(1)}).(\boldsymbol{\eta}^{(1)} + \boldsymbol{\alpha}^{(1)} \times \boldsymbol{X}'))\boldsymbol{n}']dS$$

$$-\frac{1}{2}\rho g \int_{WL} {\zeta_r^{(1)}}^2 \frac{\boldsymbol{n}'}{\sqrt{1 - {n_3'}^2}} dl \tag{3.25}$$

Through the simplification of the hydrostatics, it can be expressed as:

$$\boldsymbol{F}^{(0)} = \rho g \forall \boldsymbol{k} \tag{3.26}$$

$$\boldsymbol{F}^{(1)} = -\iint_{S_M} \left(p^{(1)}\boldsymbol{n}^{(0)} + p^{(0)}\boldsymbol{n}^{(1)}\right) dS$$

$$= \iint_{S_M} \left[\begin{array}{c} \rho g z \boldsymbol{\alpha}^{(1)} \times \boldsymbol{n}' \\ +\left(\rho \frac{\partial \Phi^{(1)}}{\partial t} + \rho g\left(\eta_3^{(1)} + \eta_4^{(1)} x_2' - \eta_5^{(1)} x_1'\right)\right)\boldsymbol{n}' \end{array}\right] dS$$

$$= -\rho g A_{WP}\left(\eta_3^{(1)} + \eta_4^{(1)} y_f - \eta_5^{(1)} x_f\right)\boldsymbol{k} + \iint_{S_M} \rho \frac{\partial \Phi^{(1)}}{\partial t}\boldsymbol{n}'\, dS \tag{3.27}$$

$$\boldsymbol{F^{(2)}} = -\frac{1}{2}\rho g\left(\eta_4^{(1)^2} + \eta_5^{(1)^2}\right)\forall \boldsymbol{k} + \rho g \forall\left(\eta_5^{(2)}\boldsymbol{i} - \eta_4^{(2)}\boldsymbol{j}\right)$$

$$+\boldsymbol{\alpha^{(1)}} \times \boldsymbol{F^{(1)}} + \iint_{S_M} \frac{1}{2}\rho \boldsymbol{\nabla}\Phi^{(1)}.\boldsymbol{\nabla}\Phi^{(1)}\boldsymbol{n}' dS$$

$$-\rho g \forall\left[\eta_4^{(1)}\eta_6^{(1)}\boldsymbol{i} + \eta_5^{(1)}\eta_6^{(1)}\boldsymbol{j} - \left(\eta_4^{(1)^2} + \eta_5^{(1)^2}\right)\boldsymbol{k}\right]$$

$$+ \iint_{S_M}\left(\frac{\partial}{\partial t}\rho \boldsymbol{\nabla}\Phi^{(1)}\right).\left(\boldsymbol{\eta^{(1)}} + \boldsymbol{\alpha^{(1)}} \times \boldsymbol{X'}\right)\boldsymbol{n}' dS$$

$$+ \iint_{S_M} \rho \frac{\partial \Phi^{(2)}}{\partial t}\boldsymbol{n}' dS$$

$$+\rho g(-A_{wp}\eta_3^{(2)} - y_f A_{wp}\eta_4^{(2)} + x_f A_{wp}\eta_5^{(2)})\boldsymbol{k}$$

$$-\rho g \forall(\eta_5^{(2)}\boldsymbol{i} - \eta_4^{(2)}\boldsymbol{j}) + \rho g \forall \eta_4^{(1)}\eta_6^{(1)}\boldsymbol{i}$$

$$+\rho g \forall \eta_5^{(1)}\eta_6^{(1)}\boldsymbol{j} + \rho g[-x_{cf}A_{wp}\eta_4^{(1)}\eta_6^{(1)} - y_{cf}A_{wp}\eta_5^{(1)}\eta_6^{(1)}$$

$$-\frac{1}{2}(\forall + z_0 A_{wp})(\eta_4^{(1)^2} + \eta_5^{(1)^2})]\boldsymbol{k} - \frac{1}{2}\rho g \int_{WL} \zeta_r^{(1)^2}\boldsymbol{n}'\, dl$$

$$= \boldsymbol{\alpha^{(1)}} \times \boldsymbol{F^{(1)}} + \iint_{S_M} \frac{1}{2}\rho \boldsymbol{\nabla}\Phi^{(1)}.\boldsymbol{\nabla}\Phi^{(1)}\boldsymbol{n}' dl$$

$$+ \iint_{S_M}\left(\frac{\partial}{\partial t}\rho \boldsymbol{\nabla}\Phi^{(1)}\right).\left(\boldsymbol{\eta^{(1)}} + \boldsymbol{\alpha^{(1)}} \times \boldsymbol{X'}\right)\boldsymbol{n}' dS$$

$$+\rho g[-x_{cf}A_{wp}\eta_4^{(1)}\eta_6^{(1)} - y_{cf}A_{wp}\eta_5^{(1)}\eta_6^{(1)}$$

$$-\frac{1}{2}z_0A_{wp}(\eta_4^{(1)^2} + \eta_5^{(1)^2})]\boldsymbol{k} - \frac{1}{2}\rho g \int_{WL} \zeta_r^{(1)^2} \frac{\boldsymbol{n}'}{\sqrt{1-n_3'^2}} dl$$

$$+\iint_{S_M} \rho \frac{\partial \Phi^{(2)}}{\partial t}\boldsymbol{n}' dS + \rho g(-A_{wp}\eta_3^{(2)} - y_f A_{wp}\eta_4^{(2)}$$

$$+x_f A_{wp}\eta_5^{(2)})\boldsymbol{k} \tag{3.28}$$

It can be observed that the 2nd-order force contains the products of the floating structure's motions and wave potential up to the 2nd-order. While evaluating the mean drift force, the contribution from the 2nd-order wave potential and motion will not be considered, since this part will be zero after taking a time-average in regular waves. In irregular waves, due to the radiation difficulty, the contributions of the 2nd-order wave potential to the 2nd-order wave loads can be approximated through the Pinkster's approximation, which will be introduced in the later section.

It should be noted that the term $\frac{1}{2}\rho g \int_{WL} \zeta_r^{(1)^2} \frac{\boldsymbol{n}'}{\sqrt{1-n_3'^2}} dl = \frac{1}{2}\rho g \int_{WL} \Big(\zeta^{(1)} - (\eta_3^{(1)} + \eta_4^{(1)}x_2' - \eta_5^{(1)}x_1')\Big)^2 \frac{\boldsymbol{n}'}{\sqrt{1-n_3'^2}} dl$ will be taken into consideration while evaluating the 2nd-order wave loads. The normal vector $\boldsymbol{n}'$ of the waterline panel towards the fluid field plays an important role that is also called the flare angle effect determining the whole term's contribution, where n_3' is the normal vector in the vertical Z direction. For a wall-sided waterline panel, the amplification of the flare angle effect is 1. However, as the

normal vector's vertical Z direction component increases from 0 to 1, this amplification increases significantly, in that situations cautious treatment should be taken.

3.4. The Derivation of the Second Order Moment

Similarly, the wave moment on the floating structure can also be derived by the direct pressure integral into a perturbation form.

$$\begin{aligned} \boldsymbol{M} &= \boldsymbol{M}^{(0)} + \varepsilon \boldsymbol{M}^{(1)} + \varepsilon^2 \boldsymbol{M}^{(2)} \\ &= -\iint_{S} p(\boldsymbol{X} - \boldsymbol{X_0}) \times \boldsymbol{n} dS \\ &= -\iint_{S_M} p(\boldsymbol{X} - \boldsymbol{X_0}) \times \boldsymbol{n} dS - \iint_{\Delta S} p(\boldsymbol{X} - \boldsymbol{X_0}) \times \boldsymbol{n} dS \end{aligned} \tag{3.29}$$

Consider:

$$\boldsymbol{X}' \times \left(\boldsymbol{\alpha}^{(\mathbf{1\ or\ 2})} \times \boldsymbol{n}'\right) + \left(\boldsymbol{\alpha}^{(\mathbf{1\ or\ 2})} \times \boldsymbol{X}'\right) \times \boldsymbol{n}' = \boldsymbol{\alpha}^{(\mathbf{1\ or\ 2})} \times (\boldsymbol{X}' \times \boldsymbol{n}') \tag{3.30}$$

$$\boldsymbol{X}' \times (\boldsymbol{H}\boldsymbol{n}') + (\boldsymbol{H}\boldsymbol{X}') \times \boldsymbol{n}' + \left(\boldsymbol{\alpha}^{(\mathbf{1})} \times \boldsymbol{X}'\right) \times \left(\boldsymbol{\alpha}^{(\mathbf{1})} \times \boldsymbol{n}'\right) = \boldsymbol{H}(\boldsymbol{X}' \times \boldsymbol{n}') \tag{3.31}$$

It can be obtained:

$$\begin{aligned} (\boldsymbol{X} - \boldsymbol{X_0}) \times \boldsymbol{n} &= \boldsymbol{X}' \times \boldsymbol{n}' + \varepsilon \begin{pmatrix} \boldsymbol{\eta}^{(1)} \times \boldsymbol{n}' \\ +\boldsymbol{\alpha}^{(1)} \times (\boldsymbol{X}' \times \boldsymbol{n}') \end{pmatrix} \\ &\quad + \varepsilon^2 \begin{pmatrix} \boldsymbol{\eta}^{(1)} \times \left(\boldsymbol{\alpha}^{(1)} \times \boldsymbol{n}'\right) \\ +\boldsymbol{H}(\boldsymbol{X}' \times \boldsymbol{n}') \\ +\boldsymbol{\eta}^{(2)} \times \boldsymbol{n}' \\ +\boldsymbol{\alpha}^{(2)} \times (\boldsymbol{X}' \times \boldsymbol{n}') \end{pmatrix} \end{aligned} \tag{3.32}$$

$$\iint_{S_M} p(\boldsymbol{X} - \boldsymbol{X_0}) \times \boldsymbol{n} dS = \iint_{S_M} \left(p^{(0)} + \varepsilon p^{(1)} + \varepsilon^2 p^{(2)}\right) [\boldsymbol{X}' \times \boldsymbol{n}'$$

$$+\varepsilon\left(\boldsymbol{\eta}^{(1)}\times\boldsymbol{n}'\right)$$

$$+\varepsilon\left(\boldsymbol{\alpha}^{(1)}\times(\boldsymbol{X}'\times\boldsymbol{n}')\right)+\varepsilon^2\boldsymbol{\alpha}^{(2)}\times(\boldsymbol{X}'\times\boldsymbol{n}')$$

$$+\varepsilon^2\begin{pmatrix}\boldsymbol{\eta}^{(1)}\times\left(\boldsymbol{\alpha}^{(1)}\times\boldsymbol{n}'\right)+\boldsymbol{H}(\boldsymbol{X}'\times\boldsymbol{n}')\\+\boldsymbol{\eta}^{(2)}\times\boldsymbol{n}'\end{pmatrix}]dS \tag{3.33}$$

Through the simplification of the hydrostatics, it can be obtained:

$$\boldsymbol{M}^{(0)} = \iint_{S_M} -p^{(0)}(\boldsymbol{X}'\times\boldsymbol{n}')dS = \iint_{S_M}\rho gz(\boldsymbol{X}'\times\boldsymbol{n}')dS$$

$$= \rho g\iint_{S_M}(z'+z_0)((n_3'y'-n_2'z')\boldsymbol{i}+(n_1'z'-n_3'x')\boldsymbol{j}+(n_2'x'\\-n_1'y')\boldsymbol{k})dS$$

$$= \rho g y_{CB}\forall\boldsymbol{i}-\rho g x_{CB}\forall\boldsymbol{j} \tag{3.34}$$

$$\boldsymbol{M}^{(1)} = \iint_{S_M}[-p^{(0)}\left(\boldsymbol{\eta}^{(1)}\times\boldsymbol{n}'+\boldsymbol{\alpha}^{(1)}\times(\boldsymbol{X}'\times\boldsymbol{n}')\right)-p^{(1)}(\boldsymbol{X}'\times\boldsymbol{n}')]dS$$

$$= \iint_{S_M}\rho gz\left(\boldsymbol{\eta}^{(1)}\times\boldsymbol{n}'+\boldsymbol{\alpha}^{(1)}\times(\boldsymbol{X}'\times\boldsymbol{n}')\right)+(\rho\frac{\partial\Phi^{(1)}}{\partial t}$$

$$+\rho g\left(\eta_3^{(1)}+\eta_4^{(1)}y'-\eta_5^{(1)}x'\right))(\boldsymbol{X}'\times\boldsymbol{n}')dS$$

$$= \rho g\forall\left(x_{CB}\eta_6^{(1)}+y_{CB}\eta_6^{(1)}\right)\boldsymbol{j}-\rho g\forall\left(x_{CB}\eta_4^{(1)}+y_{CB}\eta_5^{(1)}\right)\boldsymbol{k}$$

$$+\rho g\left(\forall\eta_2^{(1)}\boldsymbol{i}-\forall\eta_1^{(1)}\boldsymbol{j}\right)+\iint_{S_B}\rho\frac{\partial\Phi^{(1)}}{\partial t}(\boldsymbol{X}'\times\boldsymbol{n}')dS$$

$$+\rho g\left(-y_{cf}A_{WP}\eta_3^{(1)}-I_{YY}^A\eta_4^{(1)}-z_{CB}\forall\eta_4^{(1)}+I_{XY}^A\eta_5^{(1)}\right)\boldsymbol{i}$$

$$+\rho g\left(x_{cf}A_{WP}\eta_3^{(1)} + I_{XY}^{A}\eta_4^{(1)} - z_{CB}\forall\eta_5^{(1)} - I_{XX}^{A}\eta_5^{(1)}\right)\boldsymbol{j}$$

$$+\rho g\left(x_{CB}\forall\eta_4^{(1)} + y_{CB}\forall\eta_5^{(1)}\right)\boldsymbol{k}$$

$$= \iint_{S_B} \rho\frac{\partial\boldsymbol{\Phi}^{(1)}}{\partial t}(\boldsymbol{X}'\times\boldsymbol{n}')dS$$

$$+\rho g\begin{pmatrix} x_{CB}\forall\eta_6^{(1)} + \forall\eta_2^{(1)} - y_{cf}A_{WP}\eta_3^{(1)} - I_{YY}^{A}\eta_4^{(1)} - z_{CB}\forall\eta_4^{(1)} \\ +I_{XY}^{A}\eta_5^{(1)}\end{pmatrix}\boldsymbol{i}$$

$$+\rho g\begin{pmatrix} y_{CB}\forall\eta_6^{(1)} - \forall\eta_1^{(1)} + x_{cf}A_{WP}\eta_3^{(1)} + I_{XY}^{A}\eta_4^{(1)} - z_{CB}\forall\eta_5^{(1)} \\ -I_{XX}^{A}\eta_5^{(1)}\end{pmatrix}\boldsymbol{j} \qquad (3.35)$$

$$\boldsymbol{M^{(2)}} = \iint_{S_M}\begin{bmatrix} -p^{(0)}(\boldsymbol{\eta}^{(1)}\times\left(\boldsymbol{\alpha}^{(1)}\times\boldsymbol{n}'\right) + \boldsymbol{H}(\boldsymbol{X}'\times\boldsymbol{n}') + \boldsymbol{\eta}^{(2)}\times\boldsymbol{n}' \\ +\boldsymbol{\alpha}^{(2)}\times(\boldsymbol{X}'\times\boldsymbol{n}')\end{bmatrix}$$

$$-p^{(1)}\left(\boldsymbol{\eta}^{(1)}\times\boldsymbol{n}' + \boldsymbol{\alpha}^{(1)}\times(\boldsymbol{X}'\times\boldsymbol{n}')\right) - p^{(2)}(\boldsymbol{X}'\times\boldsymbol{n}')]\,dS$$

$$-\frac{1}{2}\rho g\int_{WL}{\zeta_r^{(1)}}^2(\boldsymbol{X}'\times\boldsymbol{n}')\,dl$$

$$= \boldsymbol{\alpha}^{(1)}\times\boldsymbol{M}^{(1)} + \boldsymbol{\eta}^{(1)}\times\boldsymbol{F}^{(1)} - \frac{1}{2}\rho g\int_{WL}{\zeta_r^{(1)}}^2(\boldsymbol{X}'\times\boldsymbol{n}')\,dl$$

$$+\iint_{S_M}\frac{1}{2}\rho\boldsymbol{\nabla}\boldsymbol{\Phi}^{(1)}.\boldsymbol{\nabla}\boldsymbol{\Phi}^{(1)}(\boldsymbol{X}'\times\boldsymbol{n}')dS$$

$$+\iint_{S_M}[(\frac{\partial}{\partial t}\rho\boldsymbol{\nabla}\boldsymbol{\Phi}^{(1)}).(\boldsymbol{\eta}^{(1)} + \boldsymbol{\alpha}^{(1)}\times\boldsymbol{X}')](\boldsymbol{X}'\times\boldsymbol{n}')dS$$

$$-\rho g[I_{XY}^{A}\eta_4^{(1)}\eta_6^{(1)} + I_{YY}^{A}\eta_5^{(1)}\eta_6^{(1)} + \forall z_{CB}\eta_5^{(1)}\eta_6^{(1)}$$

$$+\frac{1}{2}\forall y_{CB}\left(\eta_4^{(1)^2}-\eta_6^{(1)^2}\right)+\frac{1}{2}y_{cf}z_0A_{wp}(\eta_4^{(1)^2}+\eta_5^{(1)^2})$$

$$-\forall x_{CB}\eta_4^{(1)}\eta_5^{(1)}+\forall\eta_1^{(1)}\eta_6^{(1)}]\boldsymbol{i}$$

$$-\rho g[-I_{XY}^A\eta_5^{(1)}\eta_6^{(1)}-I_{XX}^A\eta_4^{(1)}\eta_6^{(1)}-\forall z_{CB}\eta_4^{(1)}\eta_6^{(1)}$$

$$+\frac{1}{2}\forall x_{CB}(\eta_6^{(1)^2}-\eta_5^{(1)^2})-\frac{1}{2}x_{cf}z_0A_{wp}(\eta_4^{(1)^2}$$

$$+\eta_5^{(1)^2})+\forall\eta_2^{(1)}\eta_6^{(1)}]\boldsymbol{j}$$

$$-\rho g\forall[y_{CB}\eta_4^{(1)}\eta_6^{(1)}-x_{CB}\eta_5^{(1)}\eta_6^{(1)}-\eta_1^{(1)}\eta_4^{(1)}-\eta_2^{(1)}\eta_5^{(1)}]\boldsymbol{k}$$

$$+\iint_{S_B}\rho\frac{\partial\boldsymbol{\Phi}^{(2)}}{\partial t}(\boldsymbol{X}'\times\boldsymbol{n}')dS+\rho g[\forall\eta_2^{(2)}-A_{wp}y_{cf}\eta_3^{(2)}-(I_{YY}^A$$

$$+\forall z_{CB})\eta_4^{(2)}+I_{XY}^A\eta_5^{(2)}+\forall x_{CB}\eta_6^{(2)}]\boldsymbol{i}$$

$$+\rho g[-\forall\eta_1^{(2)}+A_{wp}x_{cf}\eta_3^{(2)}-(I_{XX}^A+\forall z_{CB})\eta_5^{(2)}+I_{XY}^A\eta_4^{(2)}$$

$$+\forall y_{CB}\eta_6^{(2)}]\boldsymbol{j} \tag{3.36}$$

3.5. Another Expression of the First Order Force and Moment

Considering that in the expressions of $\boldsymbol{F^{(2)}}$ and $\boldsymbol{M^{(2)}}$ in the previous parts, there are still some cross product terms such as $\boldsymbol{\alpha^{(1)}}\times\boldsymbol{F^{(1)}}$, $\boldsymbol{\eta^{(1)}}\times\boldsymbol{F^{(1)}}$ and $\boldsymbol{\alpha^{(1)}}\times\boldsymbol{M^{(1)}}$ that need to be further expanded. In this scenario, another expression of $\boldsymbol{F^{(1)}}$ and $\boldsymbol{M^{(1)}}$ is applied to simplify these cross product terms, considering that they can lead to a more direct relation with the 1st-order motions, through the momentum conservation and the angular momentum conservation.

Through the momentum conservation, the relation between the floating structures' motions and the forces of different orders can be directly developed.

$$\boldsymbol{F} = m\boldsymbol{a} = m\ddot{\boldsymbol{X}}_{\boldsymbol{g}} = \boldsymbol{F^{(0)}} + \varepsilon\boldsymbol{F^{(1)}} + \varepsilon^2\boldsymbol{F^{(2)}} - mg\boldsymbol{k} \tag{3.37}$$

$$\boldsymbol{F^{(0)}} = mg\boldsymbol{k} \tag{3.38}$$

$$\boldsymbol{F^{(1)}} = m(\ddot{\boldsymbol{\eta}}^{(1)} + \ddot{\boldsymbol{\alpha}}^{(1)} \times \boldsymbol{X_g}') \tag{3.39}$$

$$\boldsymbol{F^{(2)}} = m(\ddot{\boldsymbol{\eta}}^{(2)} + \ddot{\boldsymbol{\alpha}}^{(2)} \times \boldsymbol{X_g}' + \ddot{\boldsymbol{H}}\boldsymbol{X_g}') \tag{3.40}$$

Similarly, through the angular momentum conservation (without external load), the moment on the floating structure could be also developed as:

$$\iiint_m (\boldsymbol{X} - \boldsymbol{X_0}) \times \frac{\partial^2(\boldsymbol{X} - \boldsymbol{X_0})}{\partial t^2} dm$$

$$= \boldsymbol{M^{(0)}} + \varepsilon\boldsymbol{M^{(1)}} + \varepsilon^2\boldsymbol{M^{(2)}} + \left(\boldsymbol{X_g} - \boldsymbol{X_0}\right) \times (-mg\boldsymbol{k}) \tag{3.41}$$

$$\boldsymbol{M^{(0)}} = mgy_g'\boldsymbol{i} - mgx_g'\boldsymbol{j} \tag{3.42}$$

$$\begin{aligned} \boldsymbol{M^{(1)}} &= \left(\boldsymbol{\eta^{(1)}} + \boldsymbol{\alpha^{(1)}} \times \boldsymbol{X_g'}\right) \times mg\boldsymbol{k} \\ &+ \iiint_{\boldsymbol{m}} \boldsymbol{X'} \times (\ddot{\boldsymbol{\eta}}^{(1)} + \ddot{\boldsymbol{\alpha}}^{(1)} \times \boldsymbol{X'}) dm \end{aligned} \tag{3.43}$$

$$\begin{aligned} \boldsymbol{M^{(2)}} &= \left(\boldsymbol{\eta^{(2)}} + \boldsymbol{\alpha^{(2)}} \times \boldsymbol{X_g'} + \boldsymbol{H}\boldsymbol{X_g'}\right) \times mg\boldsymbol{k} \\ &+ \iiint_{\boldsymbol{m}} (\boldsymbol{X'} \times (\ddot{\boldsymbol{\eta}}^{(2)} + \ddot{\boldsymbol{\alpha}}^{(2)} \times \boldsymbol{X'} + \ddot{\boldsymbol{H}}\boldsymbol{X_g'}) \\ &+ \left(\boldsymbol{\eta^{(1)}} + \boldsymbol{\alpha^{(1)}} \times \boldsymbol{X_g'}\right) \times (\ddot{\boldsymbol{\eta}}^{(1)} + \ddot{\boldsymbol{\alpha}}^{(1)} \times \boldsymbol{X_g}'))dm \end{aligned} \tag{3.44}$$

The 1st-order force's expressions in 6 DOF through the 1st-order motion can be expressed as:

$$F_x^{(1)} = m(\ddot{\eta}_1^{(1)} + \ddot{\eta}_5^{(1)} Z_g' - \ddot{\eta}_6^{(1)} Y_g') \tag{3.45}$$

$$F_y^{(1)} = m(\ddot{\eta}_2^{(1)} + \ddot{\eta}_6^{(1)} X_g' - \ddot{\eta}_4^{(1)} Z_g') \tag{3.46}$$

$$F_z^{(1)} = m(\ddot{\eta}_3^{(1)} + \ddot{\eta}_4^{(1)} Y_g' - \ddot{\eta}_5^{(1)} X_g') \tag{3.47}$$

$$\begin{aligned} M_x^{(1)} = & -mZ_g'\ddot{\eta}_2^{(1)} + mY_g'\ddot{\eta}_3^{(1)} + \left(I_{Y'Y'}^B + I_{Z'Z'}^B\right)\ddot{\eta}_4^{(1)} \\ & -I_{X'Y'}^B\ddot{\eta}_5^{(1)} - I_{X'Z'}^B\ddot{\eta}_6^{(1)} + mg(\eta_2^{(1)} + X_g'\eta_6^{(1)} - Z_g'\eta_4^{(1)}) \end{aligned} \tag{3.48}$$

$$\begin{aligned} M_y^{(1)} = & mZ_g'\ddot{\eta}_1^{(1)} - mX_g'\ddot{\eta}_3^{(1)} + \left(I_{X'X'}^B + I_{Z'Z'}^B\right)\ddot{\eta}_5^{(1)} \\ & -I_{X'Y'}^B\ddot{\eta}_4^{(1)} - I_{Y'Z'}^B\ddot{\eta}_6^{(1)} - mg(\eta_1^{(1)} - Y_g'\eta_6^{(1)} + Z_g'\eta_5^{(1)}) \end{aligned} \tag{3.49}$$

$$\begin{aligned} M_z^{(1)} = & -mY_g'\ddot{\eta}_1^{(1)} + mX_g'\ddot{\eta}_2^{(1)} + \left(I_{X'X'}^B + I_{Y'Y'}^B\right)\ddot{\eta}_6^{(1)} \\ & -I_{X'Z'}^B\ddot{\eta}_4^{(1)} - I_{Y'Z'}^B\ddot{\eta}_5^{(1)} \end{aligned} \tag{3.50}$$

Therefore, the terms $\boldsymbol{\alpha}^{(1)} \times \boldsymbol{F}^{(1)}$ in $\boldsymbol{F}^{(2}$, $\boldsymbol{\eta}^{(1)} \times \boldsymbol{F}^{(1)}$ and $\boldsymbol{\alpha}^{(1)} \times \boldsymbol{M}^{(1)}$ in $\boldsymbol{M}^{(2}$ can be expressed directly through the 1st-order motion.

$$\begin{aligned} \boldsymbol{\alpha}^{(1)} \times \boldsymbol{F}^{(1)} = & \left(\eta_5^{(1)} F_z^{(1)} - \eta_6^{(1)} F_y^{(1)}\right)\boldsymbol{i} + \left(\eta_6^{(1)} F_x^{(1)} - \eta_4^{(1)} F_z^{(1)}\right)\boldsymbol{j} \\ & + \left(\eta_4^{(1)} F_y^{(1)} - \eta_5^{(1)} F_x^{(1)}\right)\boldsymbol{k} \\ = & \, m \begin{pmatrix} \eta_5^{(1)}\ddot{\eta}_3^{(1)} + Y_g'\eta_5^{(1)}\ddot{\eta}_4^{(1)} \\ -X_g'\eta_5^{(1)}\ddot{\eta}_5^{(1)} - \eta_6^{(1)}\ddot{\eta}_2^{(1)} \\ -X_g'\eta_6^{(1)}\ddot{\eta}_6^{(1)} + Z_g'\eta_6^{(1)}\ddot{\eta}_4^{(1)} \end{pmatrix} \boldsymbol{i} \\ & + m \begin{pmatrix} \eta_6^{(1)}\ddot{\eta}_1^{(1)} + Z_g'\eta_6^{(1)}\ddot{\eta}_5^{(1)} \\ -Y_g'\eta_6^{(1)}\ddot{\eta}_6^{(1)} - \eta_4^{(1)}\ddot{\eta}_3^{(1)} \\ -Y_g'\eta_4^{(1)}\ddot{\eta}_4^{(1)} + X_g'\eta_4^{(1)}\ddot{\eta}_5^{(1)} \end{pmatrix} \boldsymbol{j} \end{aligned}$$

$$+m\begin{pmatrix}\eta_4^{(1)}\ddot{\eta}_2^{(1)}+X_g'\eta_4^{(1)}\ddot{\eta}_6^{(1)}\\-Z_g'\eta_4^{(1)}\ddot{\eta}_4^{(1)}-\eta_5^{(1)}\ddot{\eta}_1^{(1)}\\-Z_g'\eta_5^{(1)}\ddot{\eta}_5^{(1)}+Y_g'\eta_5^{(1)}\ddot{\eta}_6^{(1)}\end{pmatrix}\boldsymbol{k} \tag{3.51}$$

$$\begin{aligned}\boldsymbol{\eta^{(1)}}\times\boldsymbol{F^{(1)}} &= \left(\eta_2^{(1)}F_z^{(1)}-\eta_3^{(1)}F_y^{(1)}\right)\boldsymbol{i}+\left(\eta_3^{(1)}F_x^{(1)}-\eta_1^{(1)}F_z^{(1)}\right)\boldsymbol{j}\\ &+\left(\eta_1^{(1)}F_y^{(1)}-\eta_2^{(1)}F_x^{(1)}\right)\boldsymbol{k}\\ &= m\begin{pmatrix}\eta_2^{(1)}\ddot{\eta}_3^{(1)}+Y_g'\eta_2^{(1)}\ddot{\eta}_4^{(1)}\\-X_g'\eta_2^{(1)}\ddot{\eta}_5^{(1)}-\eta_3^{(1)}\ddot{\eta}_2^{(1)}\\-X_g'\eta_3^{(1)}\ddot{\eta}_6^{(1)}+Z_g'\eta_3^{(1)}\ddot{\eta}_4^{(1)}\end{pmatrix}\boldsymbol{i}\\ &+m\begin{pmatrix}\eta_3^{(1)}\ddot{\eta}_1^{(1)}+Z_g'\eta_3^{(1)}\ddot{\eta}_5^{(1)}\\-Y_g'\eta_3^{(1)}\ddot{\eta}_6^{(1)}-\eta_1^{(1)}\ddot{\eta}_3^{(1)}\\-Y_g'\eta_1^{(1)}\ddot{\eta}_4^{(1)}+X_g'\eta_1^{(1)}\ddot{\eta}_5^{(1)}\end{pmatrix}\boldsymbol{j}\\ &+m\begin{pmatrix}\eta_1^{(1)}\ddot{\eta}_2^{(1)}+X_g'\eta_1^{(1)}\ddot{\eta}_6^{(1)}\\-Z_g'\eta_1^{(1)}\ddot{\eta}_4^{(1)}-\eta_2^{(1)}\ddot{\eta}_1^{(1)}\\-Z_g'\eta_2^{(1)}\ddot{\eta}_5^{(1)}+Y_g'\eta_2^{(1)}\ddot{\eta}_6^{(1)}\end{pmatrix}\boldsymbol{k}\end{aligned} \tag{3.52}$$

$$\begin{aligned}\boldsymbol{\alpha^{(1)}}\times\boldsymbol{M^{(1)}} &= \left(\eta_5^{(1)}M_z^{(1)}-\eta_6^{(1)}M_y^{(1)}\right)\boldsymbol{i}+\left(\eta_6^{(1)}M_x^{(1)}-\eta_4^{(1)}M_z^{(1)}\right)\boldsymbol{j}\\ &+\left(\eta_4^{(1)}M_y^{(1)}-\eta_5^{(1)}M_x^{(1)}\right)\boldsymbol{k}\\ &= \begin{pmatrix}-mY_g'\eta_5^{(1)}\ddot{\eta}_1^{(1)}+mX_g'\eta_5^{(1)}\ddot{\eta}_2^{(1)}\\-I_{X'Z'}^B\eta_5^{(1)}\ddot{\eta}_4^{(1)}-I_{Y'Z'}^B\eta_5^{(1)}\ddot{\eta}_5^{(1)}\\+\left(I_{X'X'}^B+I_{Y'Y'}^B\right)\eta_5^{(1)}\ddot{\eta}_6^{(1)}\\-mZ_g'\eta_6^{(1)}\ddot{\eta}_1^{(1)}+mX_g'\eta_6^{(1)}\ddot{\eta}_3^{(1)}\\+I_{X'Y'}^B\eta_6^{(1)}\ddot{\eta}_4^{(1)}+I_{Y'Z'}^B\eta_6^{(1)}\ddot{\eta}_6^{(1)}\\-\left(I_{X'X'}^B+I_{Z'Z'}^B\right)\eta_6^{(1)}\ddot{\eta}_5^{(1)}\\+mg(\eta_6^{(1)}\eta_1^{(1)}-Y_g'\eta_6^{(1)}\eta_6^{(1)}\\+Z_g'\eta_6^{(1)}\eta_5^{(1)})\end{pmatrix}\boldsymbol{i}\end{aligned}$$

$$+\begin{pmatrix} -mZ'_g\eta_6^{(1)}\ddot{\eta}_2^{(1)} + mY'_g\eta_6^{(1)}\ddot{\eta}_3^{(1)} \\ -I^B_{X'Z'}\eta_6^{(1)}\ddot{\eta}_6^{(1)} - I^B_{X'Y'}\eta_6^{(1)}\ddot{\eta}_5^{(1)} \\ +\left(I^B_{Y'Y'} + I^B_{Z'Z'}\right)\eta_6^{(1)}\ddot{\eta}_4^{(1)} \\ +mY'_g\eta_4^{(1)}\ddot{\eta}_1^{(1)} - mX'_g\eta_4^{(1)}\ddot{\eta}_2^{(1)} \\ +I^B_{X'Z'}\eta_4^{(1)}\ddot{\eta}_4^{(1)} + I^B_{Y'Z'}\eta_4^{(1)}\ddot{\eta}_5^{(1)} \\ -\left(I^B_{X'X'} + I^B_{Y'Y'}\right)\eta_4^{(1)}\ddot{\eta}_6^{(1)} \\ +mg(\eta_6^{(1)}\eta_2^{(1)} + X'_g\eta_6^{(1)}\eta_6^{(1)} \\ -Z'_g\eta_6^{(1)}\eta_4^{(1)}) \end{pmatrix}\boldsymbol{j}$$

$$+\begin{pmatrix} mZ'_g\eta_4^{(1)}\ddot{\eta}_1^{(1)} - mX'_g\eta_4^{(1)}\ddot{\eta}_3^{(1)} \\ -I^B_{X'Y'}\eta_4^{(1)}\ddot{\eta}_4^{(1)} - I^B_{Y'Z'}\eta_4^{(1)}\ddot{\eta}_6^{(1)} \\ +\left(I^B_{X'X'} + I^B_{Z'Z'}\right)\eta_4^{(1)}\ddot{\eta}_5^{(1)} \\ +mZ'_g\eta_5^{(1)}\ddot{\eta}_2^{(1)} - mY'_g\eta_5^{(1)}\ddot{\eta}_3^{(1)} \\ +I^B_{X'Y'}\eta_5^{(1)}\ddot{\eta}_5^{(1)} + I^B_{X'Z'}\eta_5^{(1)}\ddot{\eta}_6^{(1)} \\ -\left(I^B_{Y'Y'} + I^B_{Z'Z'}\right)\eta_5^{(1)}\ddot{\eta}_4^{(1)} \\ -mg\begin{pmatrix}\eta_5^{(1)}\eta_2^{(1)} + X'_g\eta_5^{(1)}\eta_6^{(1)} \\ -Z'_g\eta_5^{(1)}\eta_4^{(1)}\end{pmatrix} \\ -mg(\eta_4^{(1)}\eta_1^{(1)} - Y'_g\eta_4^{(1)}\eta_6^{(1)} \\ +Z'_g\eta_4^{(1)}\eta_5^{(1)}) \end{pmatrix}\boldsymbol{k} \tag{3.53}$$

3.6. The Quadratic Transfer Function

The full expressions of the 2nd-order force and moment have been presented in the previous sections, where there are several components of various orders:

- The cross product of the 1st-order force/moment and the 1st-order motion.
- The integral of the square of the fluid velocity on the body surface.

- The integral of the product of the fluid velocity's time-gradient and the 1st-order motion on the body surface.
- The integral of the square of the relative free surface's elevation on the waterline.
- The additional terms containing the product of the 1st-order motion/acceleration.
- The contribution from the 2nd-order potential.

In irregular waves which is approximated using multiple regular waves with different frequencies, the wave loads, the fluid velocity, the floating structure's motion and acceleration, the free surface elevation in 1st-order can all be developed as the summation of the harmonic terms corresponding to the various wave frequencies. Therefore, the products and cross products of these terms can be developed into a double summation form. In this scenario, the products of the 1st-order motion and the acceleration components are presented as a brief illustration.

Considering that the 1st-order motion can be expressed through their RAO's directly, the terms such as $\eta_x^{(1)}\eta_y^{(1)}$ and $\eta_x^{(1)}\ddot{\eta}_y^{(1)}$ through their RAO's along with the incident wave can be expressed.

An incident wave containing the components with multiple wave frequencies can be expressed as:

$$\zeta = \sum_{j=1}^{N} A_j e^{i(-\omega_j t+\beta_j)} \tag{3.54}$$

The corresponding 1st- order motion can be expressed as:

$$\eta_x^{(1)} = \sum_{j=1}^{N} A_j \left|RAO_x(\omega_j)\right| e^{i(-\omega_j t+\beta_j+\theta_{xj})} \tag{3.55}$$

Where x indicates the 1st-order motions in 6 DOF and the corresponding RAO in complex value can be expressed as:

$$RAO_x(\omega) = |RAO_x(\omega)|e^{i(\theta_x)} \tag{3.56}$$

Keep the real part of the complex, it can be expressed:

$$\eta_x^{(1)} = \sum_{j=1}^{N} A_j \left|RAO_x(\omega_j)\right| \cos\left(-\omega_j t + \beta_j + \theta_{xj}\right) \tag{3.57}$$

$$\ddot{\eta}_y^{(1)} = \sum_{k=1}^{N} \begin{pmatrix} -\omega_k^2 A_k \left|RAO_y(\omega_k)\right| \\ .\cos\left(-\omega_k t + \beta_k + \theta_{yk}\right) \end{pmatrix} \tag{3.58}$$

While calculating the second order force and moment with the multiple incident wave frequencies, the terms such as $\eta_x^{(1)}\ddot{\eta}_y^{(1)}$ contained in the full expressions of the 2nd-order forces and moments can be expressed as:

$$\begin{aligned} \eta_x^{(1)}\ddot{\eta}_y^{(1)} &= \sum_{j=1}^{N}\sum_{k=1}^{N} -\omega_k^2 A_j A_k \left|RAO_x(\omega_j)\right|\left|RAO_y(\omega_k)\right| \\ &\quad \cos\left(-\omega_j t + \beta_j + \theta_{xj}\right)\cos\left(-\omega_k t + \beta_k + \theta_{yk}\right) \\ &= \sum_{j=1}^{N}\sum_{k=1}^{N} \frac{1}{2} -\omega_k^2 A_j A_k \left|RAO_x(\omega_j)\right|\left|RAO_y(\omega_k)\right| \\ &\quad \left(\cos\left(-(\omega_j - \omega_k)t + (\beta_j - \beta_k) + (\theta_{xj} - \theta_{yk})\right)\right. \\ &\quad \left. + \cos\left(-(\omega_j + \omega_k)t + (\beta_j + \beta_k) + (\theta_{xj} + \theta_{yk})\right)\right) \end{aligned} \tag{3.59}$$

While $j = k$, the product of two cosine terms can be transformed into the summation of a constant component and a time dependent component with the sum frequency that is usually not of interest due to the resonant period of the floating structure. Therefore, these constant components finally contribute to the constant force called the mean drift force.

While $j \neq k$, the resulting components with the difference frequencies are of interest and can be expressed as the summation of the in-phase term and the out-phase

term, corresponding to each pair of $\omega_j - \omega_k$. For each integral term in the full expression of the 2nd-order force and moment, there is a unique in-phase term and out-phase term, all of which will be collected later on after numerically evaluating all the integrals to obtain the final in-phase term and out-phase term, corresponding to each pair of $\omega_j - \omega_k$. Therefore, a unique amplitude and phase of a harmonic function of the drift force and moment with the difference frequency $\omega_j - \omega_k$ can be obtained through the final in-phase and out-phase terms.

It can be observed that the 2nd-order force and moment can be expressed as the product of $A_j A_k$ and a harmonic transfer function in the full expression. This transfer function is called the quadratic transfer function (QTF) and can be expressed through the matrix form containing $N \times N$ components, each of which can be interpreted as the force amplitude operator from two isolated incident waves. Therefore, each diagonal element in the full QTF matrix can be applied to evaluate the mean drift force for that particular frequency while the off-diagonal element can be applied to evaluate the 2nd-order drift force and moment in the difference frequency. Therefore, through the numerically evaluated diagonal and off-diagonal elements, the second order mean and drift wave force and moment in the irregular waves can be numerically evaluated, respectively.

3.7. The Numerical Evaluation of the Second Order Potential's Force (Pinkster's Approximation)

Through the expressions of the second-order force (or moment), it can be seen that there are mainly two parts: the first part are the quadratic terms of the 1st-order quantities from the 1st-order diffraction and radiation problem, the second part is the contribution

from the 2nd-order potential. As the water depth decreases or the difference frequency increases, the importance of taking the second-order potential's contribution into consideration increases. The total contribution from the 2nd-order potential includes the 2nd-order incident, diffraction and radiation potentials. However, due to the nonhomogeneous free surface boundary conditions of the 2nd-order hydrodynamics problems, it requires huge computational efforts to evaluate the 2nd-order diffraction and radiation potentials. In this scenario, a methodology proposed by Pinkster is applied to approximate the contribution from the 2nd-order potential to the total 2nd-order force (or moment).

According to the 1st-order and 2nd-order free surface boundary condition and the bottom condition, the corresponding 1st-order and 2nd-order monochromatic incident wave potentials can be analytically obtained through the Laplace governing equation. Considering a bichromatic wave with frequencies ω_i and ω_j ($\omega_i > \omega_j$), the 1st-order incident wave potential corresponding to each regular wave (or monochromatic wave) can be superimposed to obtain the 1st-order incident wave potential in a bichromatic wave, while the 2nd-order incident wave potential in a bichromatic wave can be given as:

$$\Phi_{inc}^{(2)} = \sum_{i=1}^{N}\sum_{j=1}^{N} A_i^{(1)} A_j^{(1)} . \frac{\cosh[(k_i - k_j)(Z+h)]}{\cosh(k_i - k_j)\,h} . \sin[(k_i - k_j)X - (\omega_i - \omega_j)t - (\varepsilon_i - \varepsilon_j)]$$

$$\cdot\frac{g^2}{2}\frac{\left(\begin{array}{c}\frac{k_i^2}{\omega_i cosh^2 k_i h}-\frac{k_j^2}{\omega_j cosh^2 k_j h}\\ +\frac{\left(\begin{array}{c}2k_i k_j(\omega_i-\omega_j)\\ .(1+\tanh k_i h\tanh k_j h)\end{array}\right)}{\omega_i\omega_j}\end{array}\right)}{(\omega_i-\omega_j)^2-(k_i-k_j)g.\tanh(k_i-k_j)h} \tag{3.60}$$

In the wave diffraction problem, the incoming waves due to the low frequency 2nd-order potential with frequency and wave number equal to $\omega_i - \omega_j$ and $k_i - k_j$ has a scattered wave with the same difference frequency but a different wave number k, following the dispersion relation. By considering that the floating body surface's boundary condition needs to be satisfied, the impact from a different wave number of the scattered wave will occur far away from the floating body. Thus $k_i - k_j$ is assumed to be the scattered wave number to take k's place, simplifying the situation and leading to a fictious gravity acceleration in the dispersion relation.

$$g_{ij} = \frac{(\omega_i-\omega_j)^2}{(k_i-k_j).\tanh(k_i-k_j)h} \tag{3.61}$$

By rebuilding the 2nd-order incident potential into the form of the 1st-order component, it can be obtained:

$$\begin{aligned}\Phi_{ij}^{(2)} &= \sum_{i=1}^{N}\frac{A_a^{(1)}g_{ij}}{(\omega_i-\omega_j)}.\frac{\cosh\{(k_i-k_j)(Z+h)\}}{\cosh(k_i-k_j)h}.\sin\{(k_i-k_j)X\\ &-(\omega_i-\omega_j)t-(\varepsilon_i-\varepsilon_j)\}\end{aligned} \tag{3.62}$$

The 2nd-order force due to the 2nd-order difference frequency potential can be approximated through the 1st-order force, considering that the 1st-order force is proportional to the wave amplitude and the gravity acceleration.

$$F_{ij}^{(2)} = F^{(1)} A_i^{(1)} A_j^{(1)} (\omega_i - \omega_j)$$

$$\frac{\frac{g}{2}\left(\frac{k_i^2}{\omega_i cosh^2 k_i h} - \frac{k_j^2}{\omega_j cosh^2 k_j h} + \frac{\left(\begin{matrix} 2k_i k_j (\omega_i - \omega_j) \\ .\left(1 + \tanh k_i h \tanh k_j h\right) \end{matrix} \right)}{\omega_i \omega_j} \right)}{(\omega_i - \omega_j)^2 - (k_i - k_j) g . \tanh(k_i - k_j) h} \quad (3.63)$$

Therefore, the contribution to the second-order drift force from the 2nd-order diffraction potential can be approximated through the 1st-order load. Considering that the main interest of the 2nd-order potential's contribution is in the 2nd-order diffraction problem, this approximation on the 2nd-order force due to the 2nd-order potential will give a satisfying result when the 1st-order diffraction and radiation are small. Moreover, there are also 1st-order diffraction and motions of the floating structure that make the significant contribution to the total 2nd-order force, the error due to this approximation regarding the 2nd-order potential's contribution remains small relative to the total 2nd-order force.

3.8. The Numerical Calculation of the QTF

The numerical evaluation of the QTF of a vertical cylinder was conducted, according to the derivations in this paper. The estimations of the corresponding components of the mean drift force coefficients have been presented and the summation of these components have been compared with the numerical results from an industry

standard commercial software as a reference. The diameter of the vertical cylinder is 40 meters and its draft is 10 m. The center of the gravity is 5 meters above the equilibrium free surface. The incident wave direction in this numerical evaluation is 180 deg and the water depth is 1500 meters.

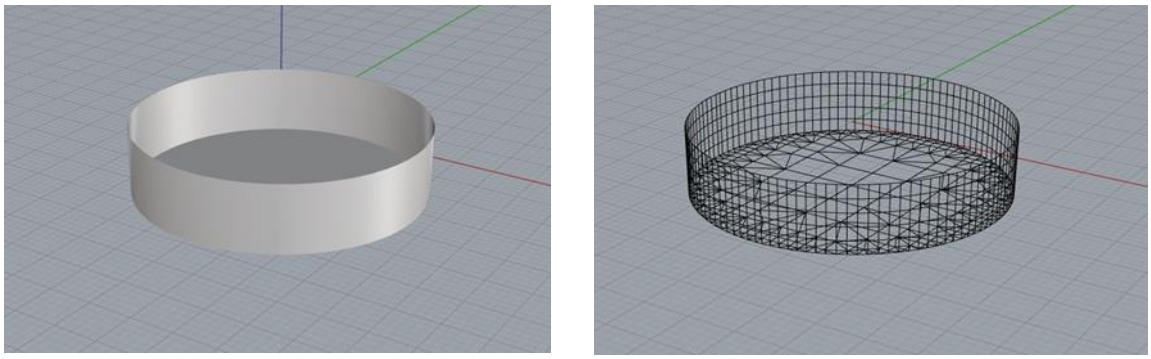

Figure 3.1. The numerical model of the vertical cylinder and the mesh of the body surface.

While numerically evaluating the mean drift force, the actual contribution of the 2^{nd}-order potential has been neglected, since its time-averaged value is zero. The contributions from other components in the full expression of the 2^{nd}-order force and moment and the mean drift force coefficient from the summation have been presented. Due to the symmetry of the vertical cylinder, the 2^{nd}-order force in X and Z axis of the global coordinate and the moment in Y axis of the vessel-fixed coordinate have been considered.

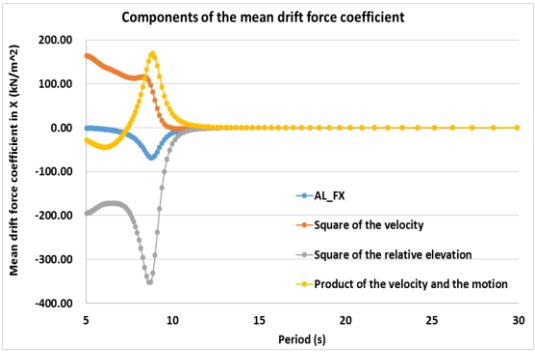

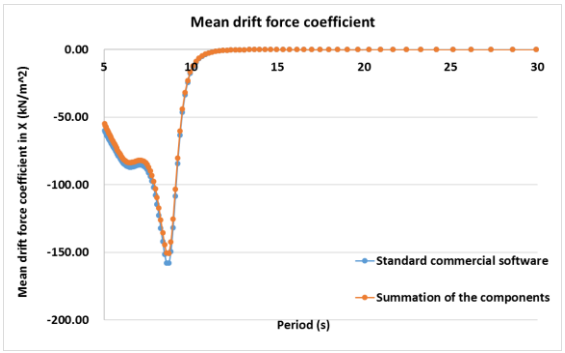

Figure 3.2. The mean drift force coefficient and its components in X direction.

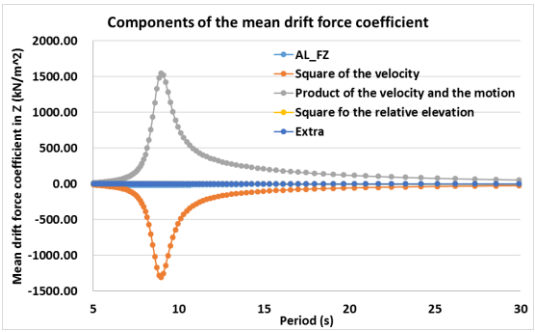

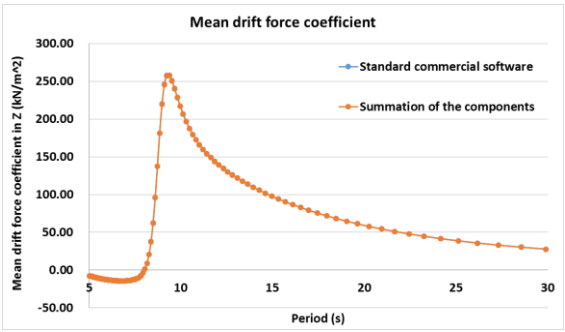

Figure 3.3. The mean drift force coefficient and its components in Z direction.

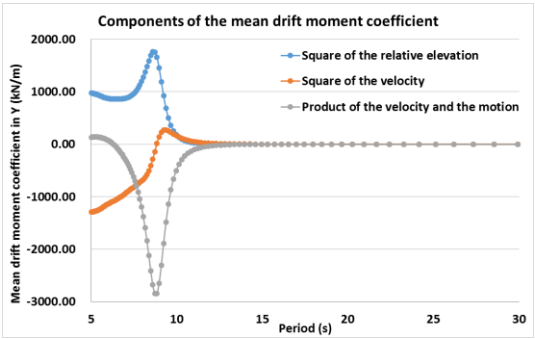

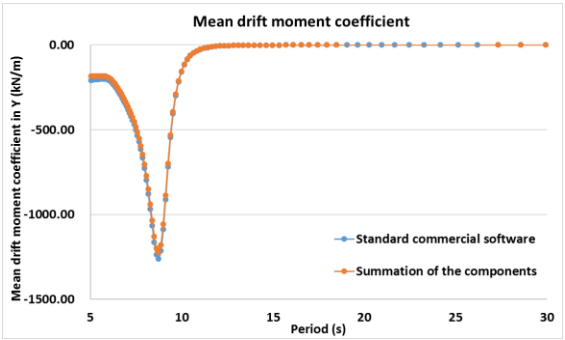

Figure 3.4. The mean drift moment coefficient and its components in Y direction.

From Figures 3.2 to 3.4, it can be seen that among the various components of a mean drift force coefficients that the contribution of integration of the relative wave elevation term along the floating hull's waterline on the free surface dominates. Therefore, care must be taken while considering the relative vertical motion terms including the motions of heave, roll and pitch. Another issue in this scenario is the normal vector of the wetted surface panel on the free surface. Due to the mathematical formulation's characteristic of the term $\frac{1}{2}\rho g \int_{WL} {\zeta_r^{(1)}}^2 \frac{\boldsymbol{n}'}{\sqrt{1-{n_3'}^2}} dl$, a panel's normal vector that projects a small value on the horizontal plane would lead to a singularity in the 2nd-order wave loads.

Due to the symmetry of the vertical cylinder and the incident wave direction, the components that are zero in the numerical evaluation have been neglected in Figure 3.4 while evaluating the 2nd-order pitch moment.

It can be observed that the summation of the various integral components of the 2nd-order force and moment match very well with the numerical results regarding the mean drift force and moment coefficients from the standard commercial software (Lee, 2013) using the direct pressure integral method. The comparison provides a convincing numerical reference while considering the amplitudes of the off-diagonal elements in the full QTF matrix, corresponding to the wave drift force and moment with difference frequencies. Through the direct pressure integral method, the off-diagonal elements in the full QTF matrix can be numerically evaluated and presented in Figure 3.5.

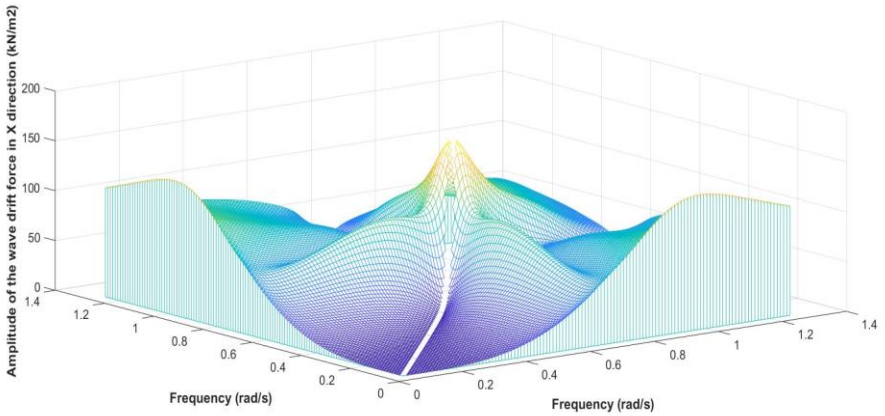

(a)

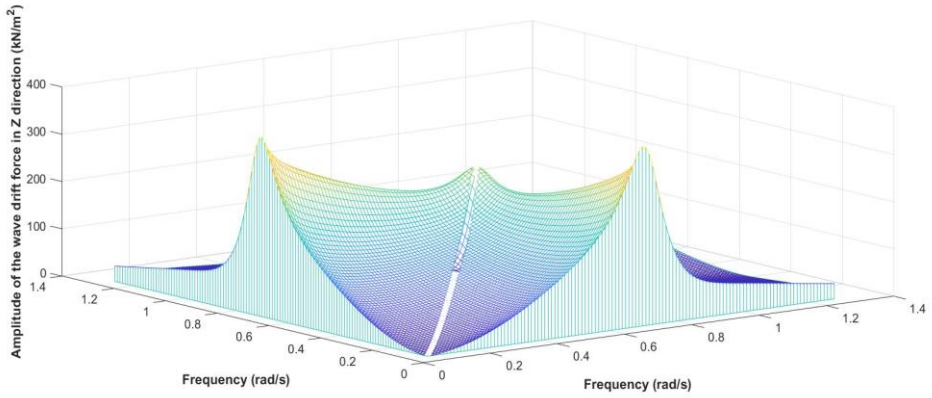

(b)

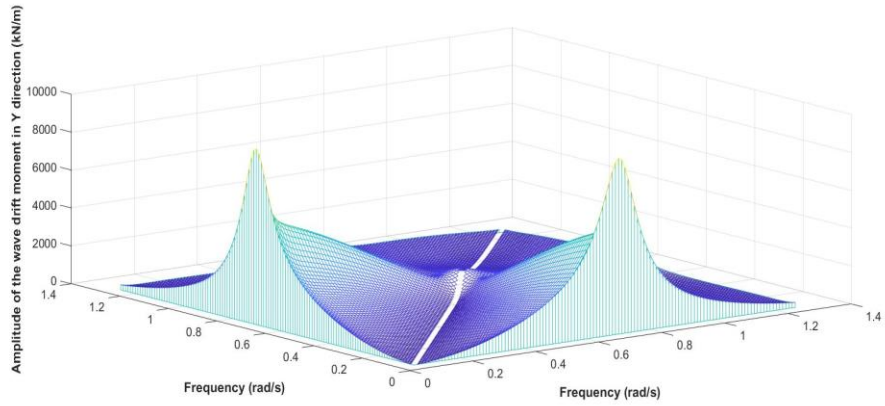

(c)

Figure 3.5. The amplitudes of the drift force coefficients with respect to wave frequencies (rad/s): (a) amplitude of the wave drift force in X direction (kN/m^2); (b) amplitude of the wave drift force in Z direction (kN/m^2); (c) amplitude of the wave drift moment in Y direction (kN/m).

From Figure 3.5, the vertical value of each element is the amplitude of the 2nd-order wave drift force and moment coefficient, corresponding to each pair of the difference of the incident wave frequencies projected onto the horizontal plane. It can be observed that the off-diagonal elements present a symmetrical characteristic regarding the principal diagonal line, namely the mean drift force and moment coefficient. The vertical values of the elements relatively close to the principal diagonal do not present an obvious difference from the diagonal elements nearby. However, when an element in the full QTF matrix is relatively far from the principal diagonal or close to the diagonal but presents the extremum, significant changes from the diagonal elements regarding the vertical values can be observed.

In Newman's approximation and several following modified approximations, a basic assumption is that the difference wave frequency is relatively low, which means the off-diagonal element is relatively close to the principal diagonal line. Based on this, the approximation of the QTF can be conducted through the mean drift force and moment coefficients on the principal diagonal line in the full QTF matrix. Some comparisons among these approximations have been previously conducted (See e.g. Molin, 2002; Chen and Duan, 2007). Variants of Newman's approximation can be presented as:

$$F(\omega_1, \omega_2) \approx F(\omega_1, \omega_1) \tag{3.64}$$

from the original Newman's approximation (Newman, 1974).

$$F(\omega_1, \omega_2) \approx sign(F)\sqrt{F(\omega_1, \omega_1)F(\omega_2, \omega_2)} \tag{3.65}$$

from the modification suggested by Molin (2002).

$$F(\omega_1, \omega_2) \approx \frac{F(\omega_1, \omega_1) + F(\omega_2, \omega_2)}{2} \tag{3.66}$$

from the modification suggested by Chen and Duan (2007).

From Figures 3.6 to 3.8, the comparisons of the QTF in different degrees of motions through the direct pressure integral and various approximations have been presented, while the difference wave frequency is respectively 0.05 rad/s and 0.25 rad/s.

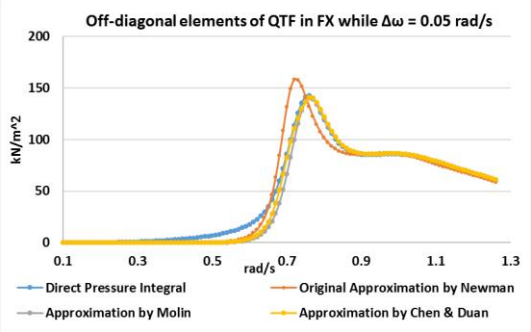

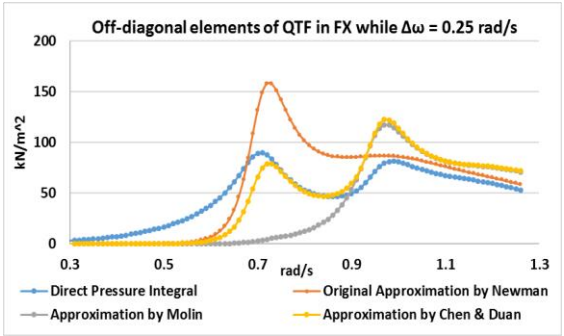

Figure 3.6. Comparison among various numerical evaluations of the wave drift force in X direction.

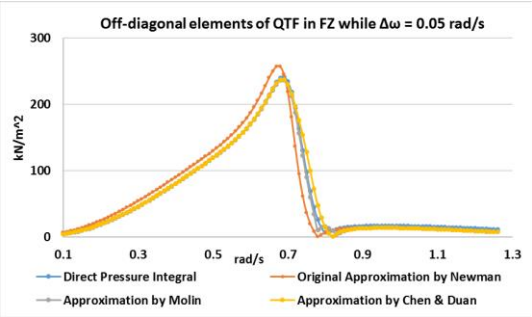

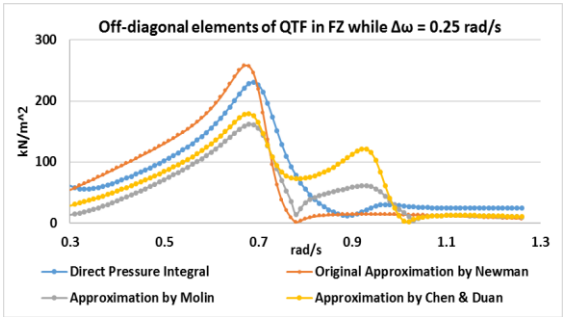

Figure 3.7. Comparison among various numerical evaluations of the wave drift force in Z direction.

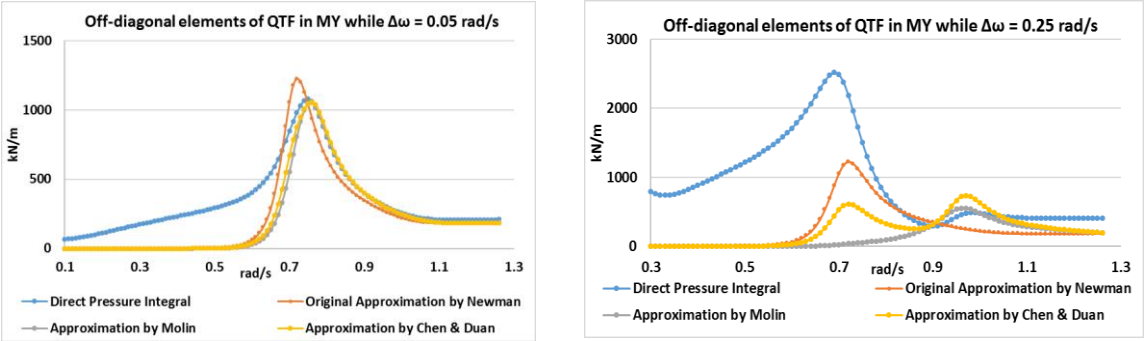

Figure 3.8. Comparison among various numerical evaluations of the wave drift moment in Y direction.

It can be observed that the differences among the direct pressure integral and two later forms of Newman's approximations are relatively small regarding the QTF in the motions of surge and heave, while the difference wave frequency is 0.05 rad/s. As the difference wave frequency increases to 0.25 rad/s, obvious discrepancies can be observed among these different numerical evaluations. This matches with the observation in Figure 3.5 that the off-diagonal elements of the QTF matrix present a significant change from the principal diagonal elements. Therefore, Newman's approximation may not provide an accurate result. Considering this, the direct numerical evaluation of the full QTF matrix is of importance, for instance, while evaluating the 2nd-order rotation motions or the difference wave frequency is relatively high.

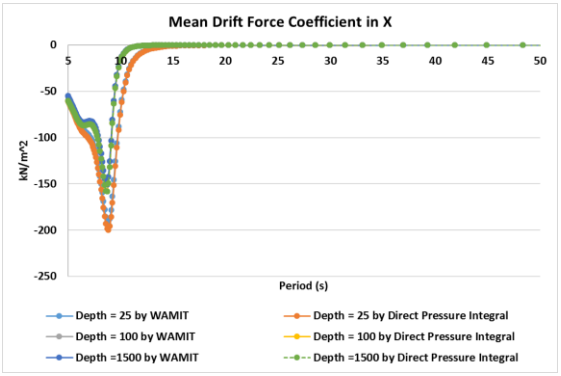

(a)

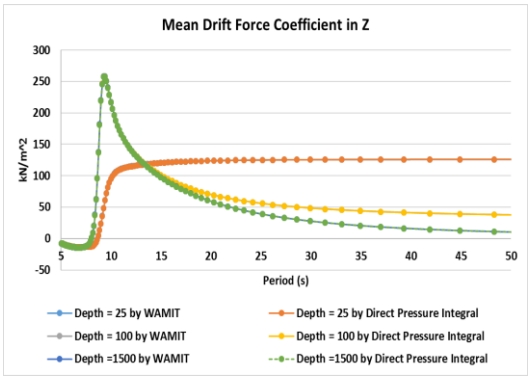

(b)

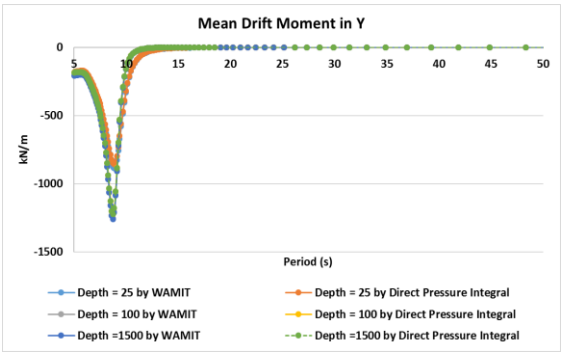

(c)

Figure 3.9. The mean drift force and moment coefficients through direct pressure integral in different water depths: (a) amplitude of the wave drift force in X direction (kN/m^2); (b) amplitude of the wave drift force in Z direction (kN/m^2); (c) amplitude of the wave drift moment in Y direction (kN/m).

In Figure 3.9, the numerically evaluated mean drift force and moment coefficients in X, Y and Z direction with water depths of 1500m, 100m and 25m are presented. It can be observed that the numerical results of the mean drift load coefficients through the direct pressure integral and the industry standard commercial software (Lee, 2013) match very well in the corresponding modes and water depths. The verified numerical mean drift force

(or moment) coefficients through the direct pressure integral method in this paper can provide a solid basis to evaluate the off-diagonal elements in the full QTF matrix later.

It is interesting to find that the mean drift force and moment coefficients with water depth of 25m are slightly different from the results in 1500m and 100m, in X and Y direction respectively, but present an obvious difference regarding the mean drift force coefficient in Z direction. As for the mean drift force coefficient in Z direction corresponding to each water depth, the numerical result presents a nearly constant value as the wave period increases. It can be seen that as the water depth decreases, the corresponding constant value increases significantly and the difference between the results in 25m and 100m is 3 times larger than that between the results in 100m and 1500m. It can be also observed that there is no peak in the water depth of 25m, which is an interesting phenomenon.

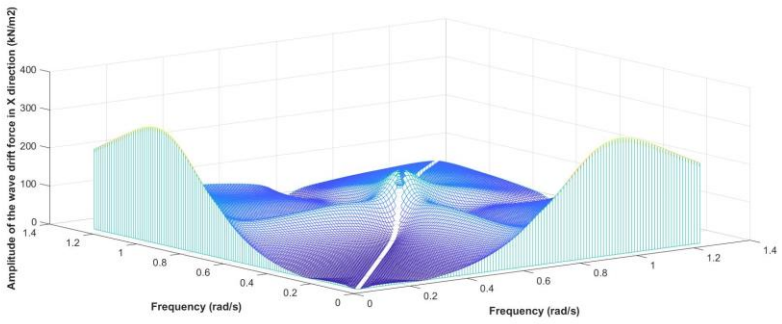

Figure 3.10. The amplitude of the drift force coefficient in X and Z direction and moment coefficient in Y direction with water depth of 100 m.

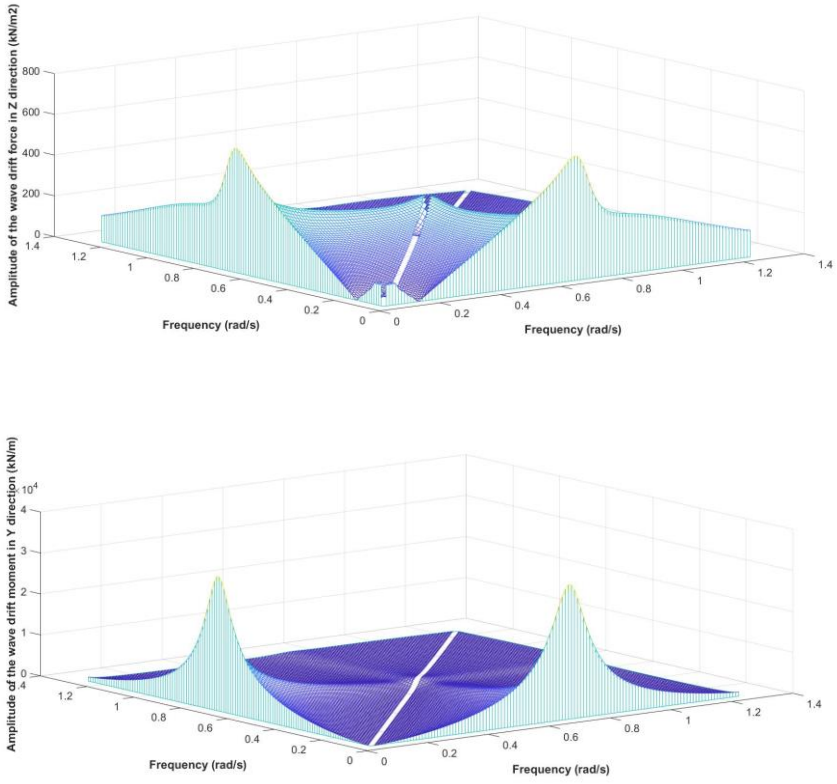

Figure 3.10. Continued.

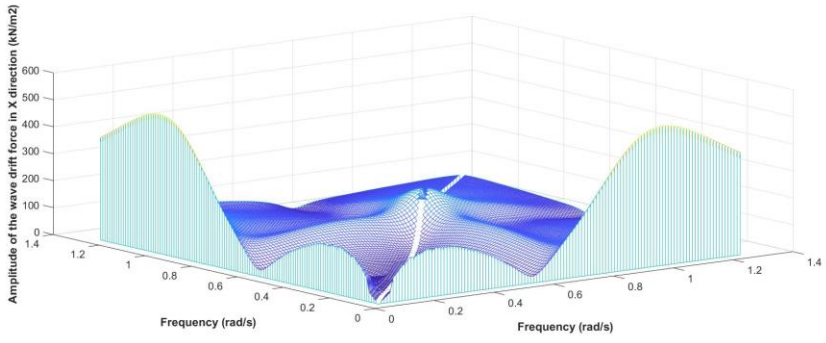

Figure 3.11. The amplitude of the drift force coefficient in X and Z direction and moment coefficient in Y direction with water depth of 25 m.

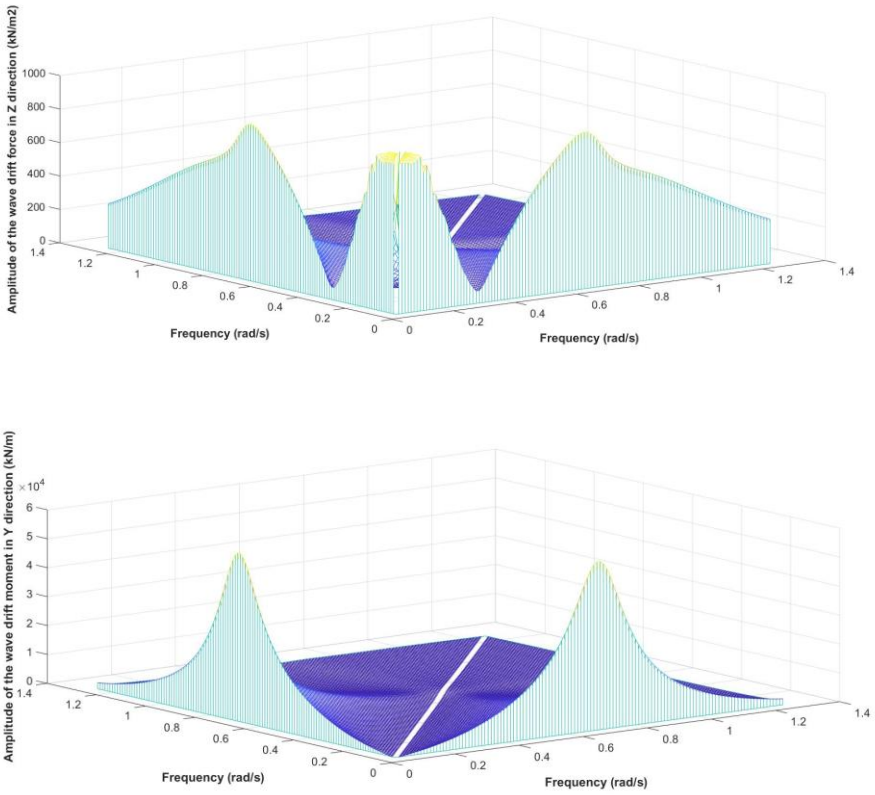

Figure 3.11. Continued.

From Figures 3.10 to 3.11, the amplitudes of the drift force and moment coefficients, namely the amplitudes of the QTFs with different water depths are presented. In the above figures, each point's horizontal position corresponds to a difference frequency pair and the corresponding vertical value is the QTF's amplitude regarding that difference frequency.

It can be observed that as the water depth decreases, the drift force and moment coefficients present a more significant response, especially for a frequency pair close to the QTF matrix's edge. Another phenomenon is that as the frequency pair's horizontal

position moves further from the principal diagonal line, the corresponding vertical value develops a more obvious difference from that of the nearest principal diagonal point.

It should be mentioned that when the water depth is 25m, the amplitude of the drift force coefficient in Z direction presents a significant response as the frequency pair moves towards the origin point. The reason of this phenomenon is the significant contribution from the 2nd-order wave potential through Pinkster's approximation. When the water depth is 1500m and 100m, the amplification factor mentioned in Pinkster's approximation is relatively small, therefore the 2nd-order wave potential's contribution to the total drift force and moment remains relatively small. However, as the water depth decreases to 25m, the wave number corresponding to the wave frequency is different from that with larger water depth, according to the dispersion relation. Due to the mathematical expression, the amplification factor in Pinkster's approximation increases significantly as the water depth decreases to 25m, when the frequency pair moves close to the origin point. Therefore, the approximated contribution from the 2nd-order wave potential becomes dominated in the total drift force coefficient and undermines Pinkster's approximation's premise. Considering this, further investigation needs to be conducted to precisely evaluate the 2nd-order wave potential's contribution in shallow water regarding the frequency pairs close to the origin in the full QTF matrix.

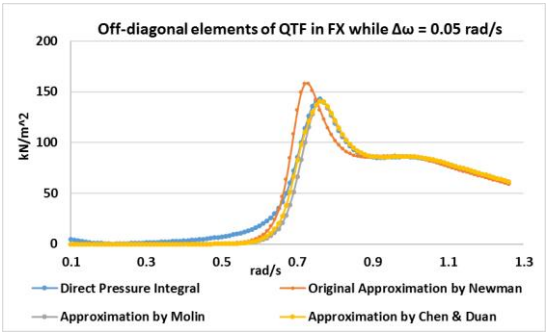

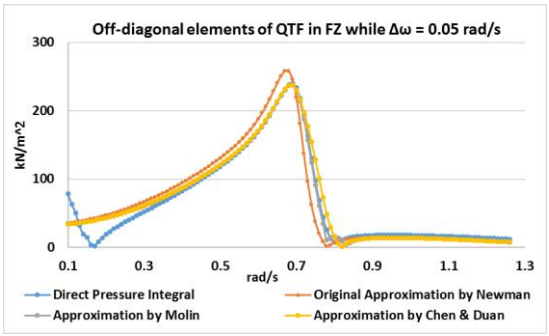

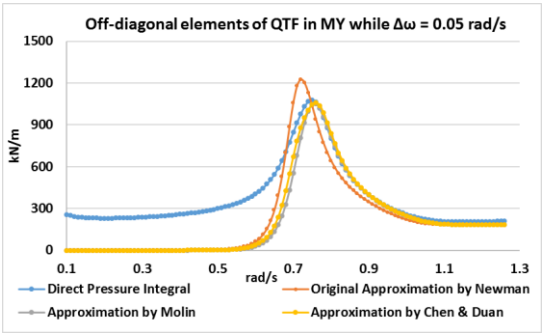

Figure 3.12. Numerical evaluations of the wave drift force with 0.05 rad/s in water depth of 100 m.

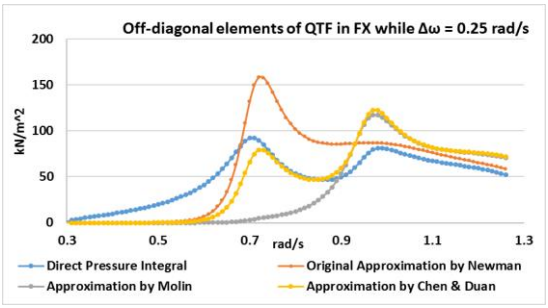

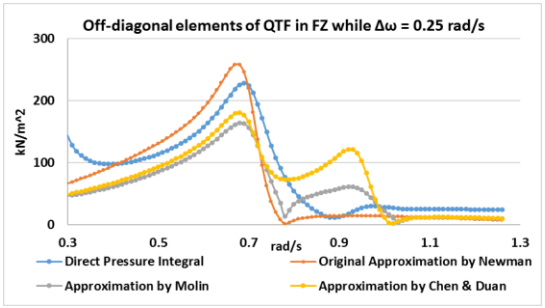

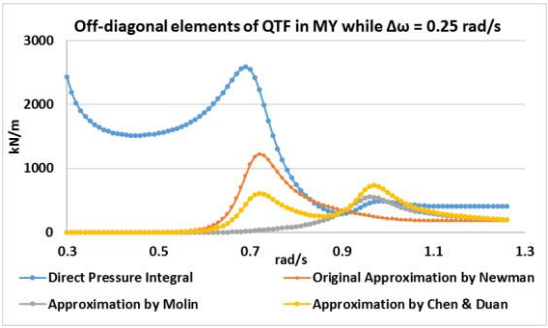

Figure 3.13. Numerical evaluations of the wave drift force with 0.25 rad/s in water depth of 100 m.

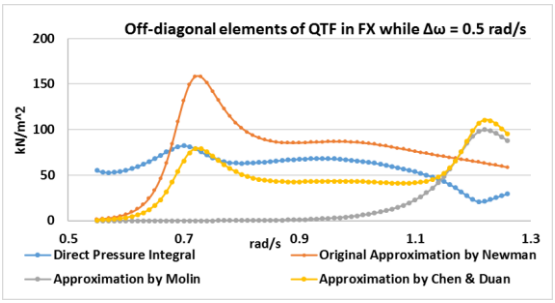

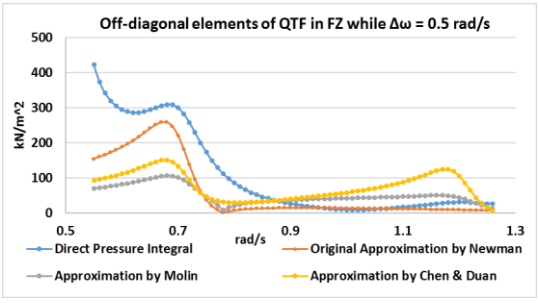

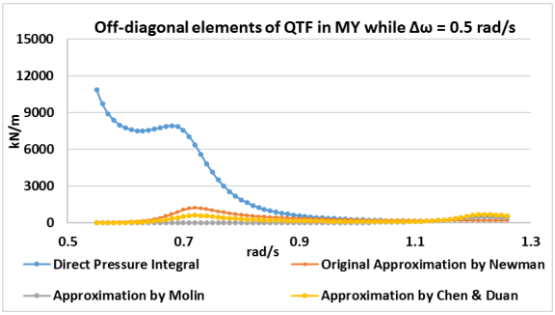

Figure 3.14. Numerical evaluations of the wave drift force with 0.5 rad/s in water depth of 100 m.

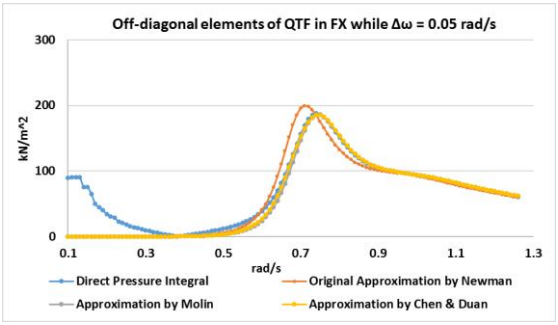

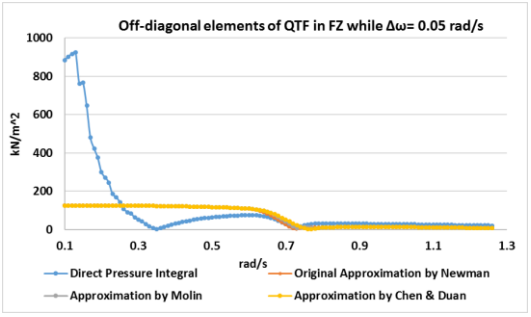

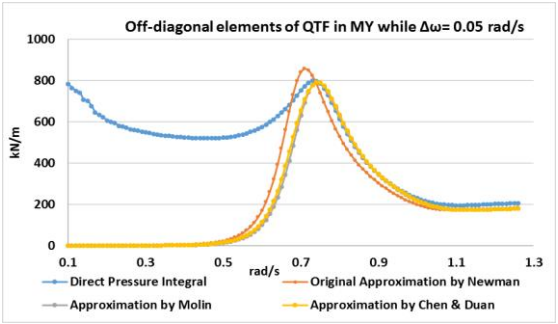

Figure 3.15. Numerical evaluations of the wave drift force with 0.05 rad/s in water depth of 25 m.

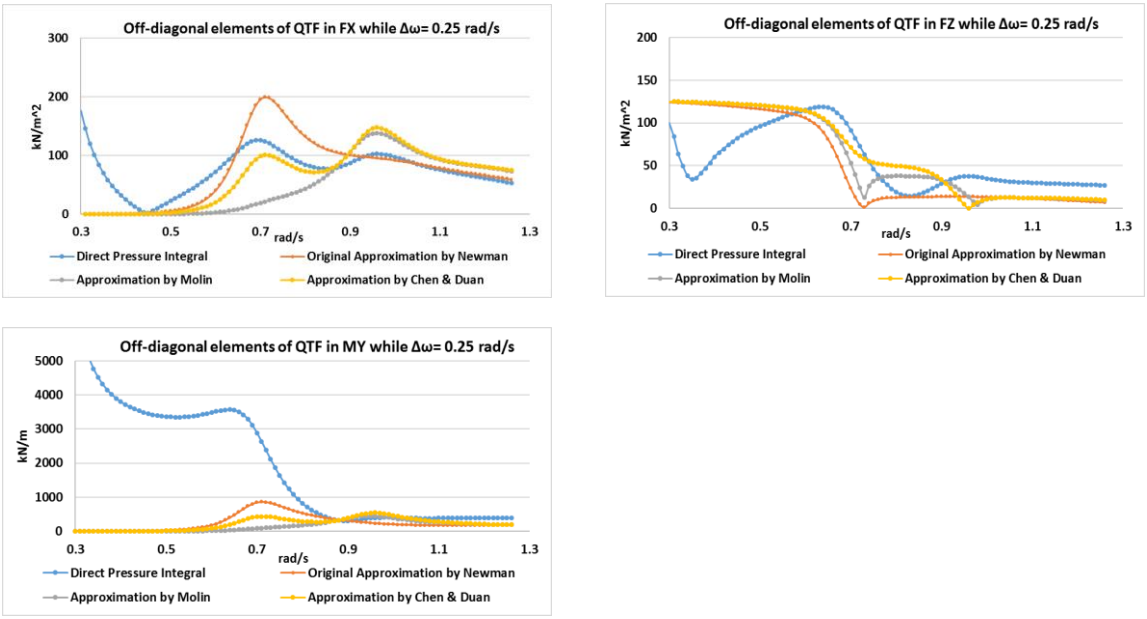

Figure 3.16. Numerical evaluations of the wave drift force with 0.25 rad/s in water depth of 25 m.

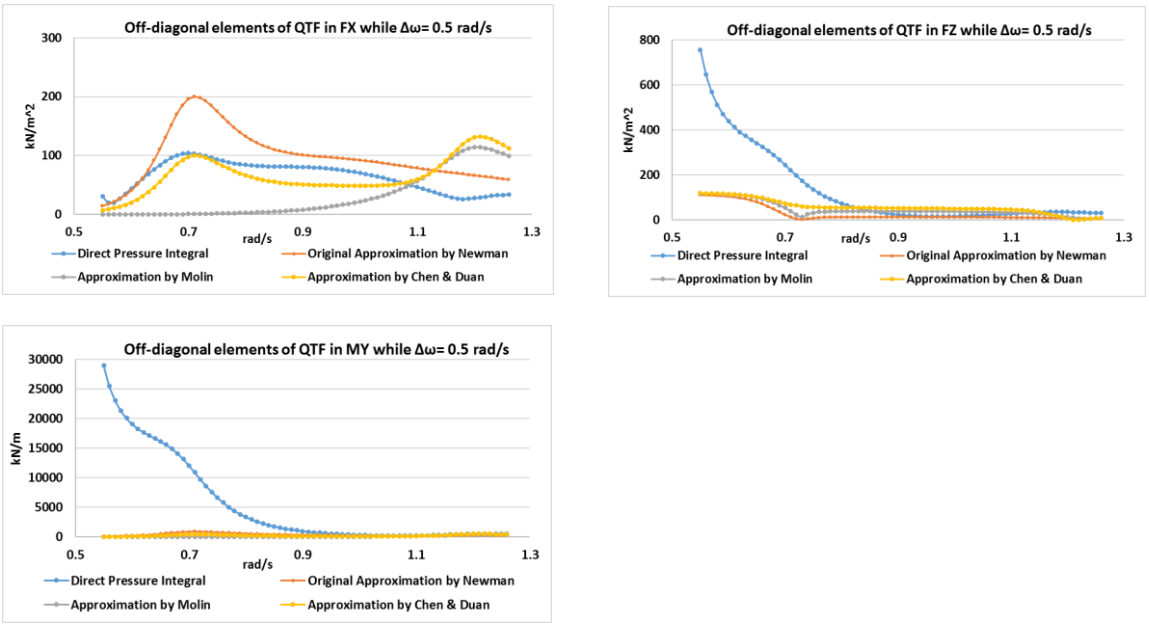

Figure 3.17. Numerical evaluations of the wave drift force with 0.5 rad/s in water depth of 25 m.

Figures 3.12 to 3.17 present the comparisons among the numerically evaluated QTFs through the direct pressure integral method and Newman's approximation. When the water depth is 1500m and the difference frequency is 0.05 rad/s, Newman's approximation and its two modified approximations can provide convincing QTF results, compared with the direct pressure integral method. As the difference frequency increases to 0.25 rad/s, the numerical results through Newman's approximation and the modified approximations becomes less satisfying. When the difference frequency increases further to 0.5 rad/s, the approximated QTFs present an obvious discrepancy from the ones through the direct pressure integral method and thus cannot be applied in this scenario. Similar results can be drawn when the water depth is 100m. This matches with the observation that the off-diagonal elements of the full QTF matrix present a significant change in their vertical values from those of the principal diagonal elements as the corresponding horizontal position moves further from the principal diagonal line. However, as the water depth decreases to 25m, the discrepancies between the direct pressure integral and Newman's approximation are more obvious for all these three difference frequencies. As the water depth decreases and the difference frequency increases, the premise of Newman's approximation and the two following modified approximations on the drift force coefficients is no longer valid. Therefore, the numerical evaluation through the direct pressure integral method is necessary and available to obtain the 2^{nd}-order wave loads involving the 1^{st}-order quantities in this scenario.

3.9. Conclusion

The derivation and the full expression of the 2nd-order force and moment applied to a floating structure have been presented through the 1st-order and 2nd-order quantities. While evaluating the contribution from the 2nd-order wave potential to the total drift force and moment, an approximation proposed by Pinkster (1980) has been applied. Pinkster's approximation considers the error due to this approximation regarding the 2nd-order potential's contribution remains small relative to the total 2nd-order force and moment.

The mean drift force coefficients on the principal diagonal of the QTF matrix for a vertical cylinder have been calculated through the summation of the integrals in the expressions presented in this section. The results compare well with the mean drift force coefficients obtained through the industry standard commercial software (Lee, 2013), providing a convincing numerical reference while calculating the off-diagonal elements in the QTF matrix. The off-diagonal elements present a symmetrical characteristic regarding the mean drift force coefficients. When an element in the full QTF matrix is far from the principal diagonal or close to the diagonal but presents an extremum, significant changes from the diagonal element can be observed. This means as the difference frequency increases, Newman's approximation may not provide an accurate result. Considering this, the direct numerical evaluation of the full QTF matrix is of importance, for instance, while evaluating the 2nd-order rotation motions.

The mean drift force in vertical Z direction with water depth of 25m presents a significant difference from the ones with the water depths of 1500m and 100m. In general, as the water depth decreases, the nearly constant mean drift force coefficient in Z direction

at relatively higher wave period increases and the QTFs present a more significant response. At the water depth of 25m, the amplification factor in Pinkster's approximation (Pinkster, 1980) increases significantly when the frequency pair moves towards the origin, due to the dispersion relation. The dominated 2^{nd}-order wave contribution neglects the actual physical meaning, which means Pinkster's approximation may meet its limitation in shallow water in estimating the off-diagonal QTF elements. Therefore, it is necessary to apply the direct pressure integral method to numerically evaluate the full QTF matrix, which can be presented as a meaningful reference. In the next section, the effect of the current or vessel's forward speed on the 2^{nd}-order wave loads will be comparatively investigated.

4. A COMPARATIVE STUDY OF 2ND-ORDER WAVE LOADS WITH FORWARD SPEED THROUGH ARANHA'S FORMULA AND NEUMANN-KELVIN LINEARIZATION*

4.1. Introduction

A derivation of the full expression of the 2nd-order wave loads acting on a floating body was presented in our previous section through the direct pressure integral method, in which both the mean drift wave forces and moments coefficients and full quadratic transfer function have been presented. This was compared with Newman's approximation (Newman, 1974) while evaluating the off-diagonal elements in the full QTF matrix. The direct pressure integral method presents its importance and necessity, especially when the difference wave frequency increases and water depth decreases.

While considering the mean wave forces and moments acting on a floating body in a current or with forward speed, several numerical solutions have been proposed and applied including the far field method and the near field method. Aranha (1994) proposed a far field-based formula to consider the effect of current or a floating body's forward speed on the mean wave forces and moments. This formula has been widely applied in the offshore engineering field due to its relative simplicity, but has a limitation assumption of

---

* Part of this section is reprinted with permission from "Study on 2nd-Order Wave Loads with Forward Speed through Aranha's Formula and Neumann-Kelvin Linearization" by Zhitian Xie, Jeffrey Falzarano, 2020. *Proceedings of the ASME 2020 39th International Conference on Ocean, Offshore and Arctic Engineering*, Copyright (2020) by ASME Publishing.

relatively low current velocity or forward speed. As for the near field methodology, Joncquez (2009) discussed two linearization, Neumann-Kelvin and Double-Body flow linearization. Through his comparisons, it was found that Neumann-Kelvin linearization works better for the Series 60 and Wigley hull III and is more robust and less sensitive to the smoothness of the hull geometry. A similar conclusion was drawn by Kim (2010), who also indicated that Neumann-Kelvin linearization showed generally better results in the case of higher Froude numbers and slender bodies. Yu (2017) conducted a comparative study of the Neumann-Kelvin and Rankine source method for wave resistance and found that the Rankine source method can give satisfactory results for a wider range of ship models, but with a quite expensive numerical calculation cost, compared with Neumann-Kelvin linearization. Moreover, the Neumann-Kelvin has the additional benefit of using the same panelization as used in solving the wave body interaction problem.

In this section, the effect of the current or the floating body's forward speed on the mean wave forces has been numerically computed through Aranha's formula and the Neumann-Kelvin linearization. An arbitrary basis flow including the lateral speed and yaw rate has also been taken into consideration and the corresponding analysis has been given. The current work in this section will provide a meaningful numerical basis for the research of combined seakeeping and maneuvering in waves.

4.2. Introduction of Aranha's Formula

The irregular wave consists of many different components with different wave frequencies. Therefore, the slow-drift excitation can be written as

$$F^{SD}(t) = \sum_{j=1}^{N}\sum_{k=1}^{N} A_j A_k \{T_{jk}^{ic} \cos[(w_k - w_j)t + (\varepsilon_k - \varepsilon_j)] + T_{jk}^{ic} \sin[(w_k - w_j)t + (\varepsilon_k - \varepsilon_j)]\} \quad (4.1)$$

Take the mean value of this slow-drift excitation over time, the average value can be written as

$$\overline{F^{SD}} = \sum_{j=1}^{N} A_j{}^2 T_{jj}^{ic}(w_j) \quad (4.2)$$

Where $T_{jj}^{ic}(w_j)$ is the diagonal component of the full QTF matrix. According to Newman's approximation,

$$T_{jk}^{ic} = T_{kj}^{ic} = 0.5(T_{jj}^{ic} + T_{kk}^{ic}) \text{ and } T_{jk}^{is} = 0. \quad (4.3)$$

From Maruo's theory, the mean drift force with a regular wave in finite water depth can be obtained through

$$\bar{F} = \frac{1}{4}\rho g(A_I^2 + A_R^2 - A_T^2) \cdot (1 + \frac{2kh}{\sinh(2kh)}) \quad (4.4)$$

According to the energy conservation, this formula in deep water can be rewritten as

$$\overline{F(w)} = \frac{1}{2}\rho g A_R^2 = \frac{1}{2}\rho g A_I^2(w) \cdot |R(w)|^2 \quad (4.5)$$

Where R indicates the wave reflection coefficient. Therefore, according to 4.2 and 4.4 the diagonal component of the full QTF matrix can be written as

$$T_{jj}^{ic}(w_j) = \frac{1}{2}\rho g |R(w_j)|^2 \quad (4.6)$$

According to Aranha's theory, due to the effect of wave damping (assume the current velocity U is opposite to the wave propagation direction), the relation between the wave reflection and transmit coefficients can be written as

$$\big(1-2(U/c)\big)|T(w_e;U)|^2+\big(1+2(U/c)\big)|R(w_e;U)|^2$$

$$=1-2(U/c),\ c=g/w \tag{4.7}$$

Disregarding the terms of $(U/c)^2$, one could obtain:

$$|T(w_e;U)|^2+\frac{|R(w_e;U)|^2}{\big(1-4(U/c)\big)}=1 \tag{4.8}$$

Considering $|T(w_e)|^2+|R(w_e)|^2=1$ and $|T(w_e)|=\ |T(w)|$, one could obtain:

$$|R(w_e;U)|^2=(1-4(U/c))|R(w_e)|^2 \tag{4.9}$$

Therefore, the QTF with wave frequency $w_j$and the wave drift damping effect can be written as:

$$T_{jj}^{ic}\big(w_j;U\big)=\ T_{jj}^{ic}(w_e)\cdot(1-4(U/c)) \tag{4.10}$$

Where $(1-4(U/c))$ is Aranha's factor and w_e indicates the encounter wave frequency,

$$w_e=w_j(1-U/c) \tag{4.11}$$

Using a Taylor expansion for $R(w_e)=R(w_j(1-U/c))$ and disregarding the terms of order $(U/c)^2$, the formula turns out to be

$$T_{jj}^{ic}\big(w_j;U\big)=\ T_{jj}^{ic}\big(w_j\big)-U(\frac{w^2}{g}T_{jj}^{ic}\big(w_j\big)+4\frac{w}{g}T_{jj}^{ic}\big(w_j\big)) \tag{4.12}$$

4.3. The Neumann-Kelvin and Double-Body Linearization

A well-known linearization scheme in ship hydrodynamics is the Neumann-Kelvin linearization with respect to the forward speed *U*, whose assumption is that the radiation potential caused by the floating body is less significant than the uniform flow (Kim and Kim, 2010). Moreover, the Kelvin ship waves effects on the free surface and the impact on the flow potential due to the floating body's shape are negligible, which simplifies the

boundary conditions. Therefore, it is also called uniform-flow linearization and applicable for a slender floating body, whose total potential can be expressed as:

$$\Phi_{total}(x,y,z,t) = -|U| \cdot x \cdot cos\beta - |U| \cdot y \cdot sin\beta + \Phi(x,y,z,t) \tag{4.13}$$

where:

$$\Phi(x,y,z,t) = \begin{pmatrix} \Phi_I(\boldsymbol{x},\omega_0,\beta) + \Phi_S(\boldsymbol{x},\omega_0,\beta) \\ +i\omega \sum_{j=1}^{6} \eta_i \psi_{Rj}(\boldsymbol{x},\omega_e,U) \end{pmatrix} \cdot e^{-i\omega_e t} \tag{4.14}$$

In this scenario, Φ denotes the wave potential, η_i denotes the vessel's motions in 6 degrees of freedom, ω_0 denotes the wave frequency while ω_e is the encounter frequency. ψ_R denotes the radiation wave potential, and β is the wave direction with respect to the vessel-fixed coordinate.

The double-body flow linearization was introduced by Dawson (1977), who considers both the forward speed U and the shape of the ship hull. The steady potential on the hull through the Double-Body is calculated by assuming the symmetry of the ship hull with respect to the free surface at z = 0 (Kim and Kim, 2010). In the previous research, the numerically estimated added resistances through these two methodologies show discrepancies, due to the radiation components from different body-boundary conditions.

The total potential:

$$\Phi_{total} = \varphi + \Phi \tag{4.15}$$

where φ is the steady base flow that is of $O(1)$ and Φ is the perturbation potential, which is of $O(\varepsilon)$.

The linearized boundary condition for the perturbation potential in the Neumann-Kelvin linearization can be expressed as:

$$\left[\frac{\partial}{\partial t} - \boldsymbol{W}\cdot\boldsymbol{\nabla}\right]\zeta = \frac{\partial \Phi}{\partial z} \quad on\ z = 0 \tag{(4.16)}$$

$$\left[\frac{\partial}{\partial t} - \boldsymbol{W}\cdot\boldsymbol{\nabla}\right]\Phi = -g\zeta \quad on\ z = 0$$

$$\frac{\partial \Phi}{\partial n} = \sum_{j=1}^{6}\left(\frac{\partial \eta_j}{\partial t} n_j + \eta_j m_j\right) \text{ on } S_B$$

The linearized boundary condition for the perturbation potential in double-body flow linearization can be expressed as:

$$\left[\frac{\partial}{\partial t} - (\boldsymbol{W} - \boldsymbol{\nabla}\varphi)\cdot\boldsymbol{\nabla}\right]\zeta = \frac{\partial^2 \varphi}{\partial z^2}\zeta + \frac{\partial \Phi}{\partial z} \quad on\ z = 0 \tag{4.17}$$

$$\left[\frac{\partial}{\partial t} - (\boldsymbol{W} - \boldsymbol{\nabla}\varphi)\cdot\boldsymbol{\nabla}\right]\Phi = -g\zeta + \boldsymbol{W}\cdot\boldsymbol{\nabla}\varphi - \frac{1}{2}\boldsymbol{\nabla}\varphi\cdot\boldsymbol{\nabla}\varphi \quad on\ z = 0$$

$$\frac{\partial \Phi}{\partial n} = \sum_{j=1}^{6}\left(\frac{\partial \eta_j}{\partial t} n_j + \eta_j m_j\right) \text{ on } S_B$$

where $\boldsymbol{W} = (U\text{-}\Omega_R y)\boldsymbol{i} + (V + \Omega_R x)\boldsymbol{j}$, where U and V are the vessel's forward and lateral speed, respectively; Ω_R is the vessel's yaw's angular speed; ζ is the wave elevation on the free surface. m_i is the m-term containing the interaction between the steady and unsteady solutions. In Neumann-Kelvin linearization with only forward speed U for example: (m_1, m_2, m_3, m_4, m_5, m_6) = (0, 0, 0, 0, Un_3, $-Un_2$); with only lateral speed V for example: (m_1, m_2, m_3, m_4, m_5, m_6) = (0, 0, 0, $-Vn_3$, 0, Vn_1). On the other hand, in the double-body flow linearization, the m-terms can be expressed as:

$$(m_1, m_2, m_3) = (\boldsymbol{n}\cdot\boldsymbol{\nabla})(\boldsymbol{W} - \boldsymbol{\nabla}\varphi) \tag{4.18}$$

$$(m_4, m_5, m_6) = (\boldsymbol{n}\cdot\boldsymbol{\nabla})\left(\boldsymbol{x}\times(\boldsymbol{W} - \boldsymbol{\nabla}\varphi)\right)$$

The boundary condition has been modified, due to the vessel's forward speed. The scattered wave potential Φ_S in this scenario and Green's function G should be evaluated at ω_0 and ω_e, respectively.

$$2\pi\Phi_S(\boldsymbol{x},\omega_0) + \iint_{S_M} \Phi_S(\boldsymbol{x},\omega_0)\frac{\partial G(\boldsymbol{x},\omega_e)}{\partial n_\xi} dS = -\iint_{S_M} G(\boldsymbol{x},\omega_e)\frac{\partial \Phi_I(\boldsymbol{x},\omega_0)}{\partial n_\xi} dS \quad (4.19)$$

Through Greens identity and a variant of Stokes theorem that the forward speed boundary value problem can be solved through obtaining the boundary condition at zero speed and a modification (Guha and Falzarano, 2015) due to the vessel's forward speed. The wave loads from the scattered wave potential can be evaluated.

$$\frac{\partial \Psi}{\partial n} = \sum_{j=1}^{6}\left(\frac{\partial \eta_j}{\partial t} n_j + \eta_j m_j\right) \text{ on } S_B \quad (4.20)$$

For normal vectors direction towards the fluid domain, the above equation can be written as:

$$\frac{\partial \varphi_R}{\partial n} = \sum_{j=1}^{6}(i\omega n_j + m_j) \quad (4.21)$$

where:

$$\Phi_R = \sum_{j=1}^{6} \varphi_{Rj}\eta_j \quad (4.22)$$

To evaluate the 1st-order wave forces and moments due to the scattered potential, its expression through direct pressure integration can be written as:

$$\boldsymbol{F}_{sca}^{(1)} = \iint_{S_M} \rho \frac{\partial \Phi_{sca}^{(1)}}{\partial t}\boldsymbol{n}^{(\mathbf{0})} dS = -i\omega\rho \iint_{S_M} \Phi_{sca}^{(1)}\boldsymbol{n}^{(\mathbf{0})} dS \quad (4.23)$$

Therefore, while there is an arbitrary basis flow including head seas and quartering seas, $F^{(1)}_{sca}$ in *jth* mode can be thus expressed as:

$$F_{sca}^{(1)}(j) = -\rho \iint_{S_M} \varphi_{Rj}^{(1)} \frac{\partial \Phi_I}{\partial n} dS \qquad \text{for j = 1, 2, 3}$$

$$= -\rho \iint_{S_M} \varphi_{Rj}^{(1)} \frac{\partial \Phi_I^{(1)}}{\partial n} dS + \frac{\rho U_y}{i\omega} \iint_{S_M} \varphi_{R3}^{(1)} \frac{\partial \Phi_I^{(1)}}{\partial n} dS \qquad \text{for j = 4}$$

$$= -\rho \iint_{S_M} \varphi_{Rj}^{(1)} \frac{\partial \Phi_I^{(1)}}{\partial n} dS + \frac{\rho U_x}{i\omega} \iint_{S_M} \varphi_{R3}^{(1)} \frac{\partial \Phi_I^{(1)}}{\partial n} dS \qquad \text{for j = 5}$$

$$= -\rho \iint_{S_M} \varphi_{Rj}^{(1)} \frac{\partial \Phi_I^{(1)}}{\partial n} dS - \frac{\rho U_x}{i\omega} \iint_{S_M} \varphi_{R2}^{(1)} \frac{\partial \Phi_I^{(1)}}{\partial n} dS$$

$$- \frac{\rho U_y}{i\omega} \iint_{S_M} \varphi_{R1}^{(1)} \frac{\partial \Phi_I^{(1)}}{\partial n} dS - \frac{\rho U_y}{i\omega} \iint_{S_M} \varphi_{R1}^{(1)} \frac{\partial \Phi_I^{(1)}}{\partial n} dS \qquad \text{for j = 6} \qquad (4.24)$$

According to Kim and Kim (2010), the added resistance due to the forward speed or current in waves is the longitudinal component of the mean drift force, whose expression based on the double-body linearization scheme can be written as:

$$\overline{\boldsymbol{F}^{(2)}} = -\frac{1}{2}\rho g \int_{WL} \zeta_r^{(1)^2} \frac{\boldsymbol{n}'}{\sqrt{1 - n_3'^2}} dl + \rho \iint_{S_M} g z_0 \, \boldsymbol{n}^{(2)} ds$$

$$+\rho \int_{WL} \left(-U \frac{\partial \varphi}{\partial x} + \frac{1}{2} \nabla\varphi \cdot \nabla\varphi\right) \times \zeta_r^{(1)} \cdot \frac{\boldsymbol{n}'}{\sqrt{1 - n_3'^2}} dl$$

$$+\rho \int_{WL} \begin{bmatrix} \left(\boldsymbol{\eta}^{(1)} + \boldsymbol{\alpha}^{(1)} \times \boldsymbol{X}'\right) \\ \cdot \boldsymbol{\nabla}\left(-U \frac{\partial \varphi}{\partial x} + \frac{1}{2} \nabla\varphi \cdot \nabla\varphi\right) \times \zeta_r^{(1)} \\ \cdot \frac{\boldsymbol{n}'}{\sqrt{1 - n_3'^2}} \end{bmatrix} dl$$

$$+\rho \iint_{S_M} \begin{bmatrix} \left(\boldsymbol{\eta}^{(1)} + \boldsymbol{\alpha}^{(1)} \times \boldsymbol{X}'\right) \\ \cdot \boldsymbol{\nabla}(-U \frac{\partial \Phi_1}{\partial x} + \nabla\varphi \cdot \nabla\Phi^{(1)} \\ + \frac{\partial \Phi^{(1)}}{\partial t}) \end{bmatrix} \boldsymbol{n}' ds$$

$$+\rho \iint_{S_M} \left(\boldsymbol{\eta}^{(1)} + \boldsymbol{\alpha}^{(1)} \times \boldsymbol{X}'\right) \cdot \boldsymbol{\nabla}(-U\frac{\partial \varphi}{\partial x} + \frac{1}{2}\nabla\varphi \cdot \nabla\varphi)\, \boldsymbol{n}' ds$$

$$+\rho \iint_{S_M} (gz_1 + \frac{\partial \Phi_1}{\partial t} - U\frac{\partial \Phi_1}{\partial x} + \nabla\varphi \cdot \nabla\Phi^{(1)}) \cdot \boldsymbol{n}' ds$$

$$+ \iint_{S_M} \frac{1}{2}\rho \boldsymbol{\nabla}\Phi^{(1)} . \boldsymbol{\nabla}\Phi^{(1)} \boldsymbol{n}' dS$$

$$+\rho \iint_{S_M} (-U\frac{\partial \varphi}{\partial x} + \frac{1}{2}\nabla\varphi \cdot \nabla\varphi)\, \boldsymbol{n}^{(2)} ds \tag{4.25}$$

By substituting φ as zero, the mean drift force of the Neumann-Kelvin linearization scheme can be obtained.

4.4. Numerical Study on Aranha's Formula and Neumann-Kelvin Linearization

The numerical evaluation of the QTF and mean drift force with and without forward speed or current velocity of a vertical cylinder was conducted, according to the derivations in this paper. The diameter of the vertical cylinder is 40 meters and its draft is 10 meters. The center of gravity is 5 meters above the equilibrium free surface. The incident wave direction in this numerical evaluation is 180 deg and the water depth is 1500 meters. The estimations of the mean drift force coefficients have been presented and compared with the numerical results from an industry standard commercial software as a reference (Lee, 2013).

In Figure 4.1, the numerical results of the longitudinal mean drift loads with different forward speeds have been presented through Aranha's formula and the Neumann-Kelvin linearization, to consider the wave drift damping effect. Generally speaking, the mean drift damping, namely the impact of the forward speed or the current

velocity on the mean drift force presents two facts. One is the shift impact of the frequency, which is consistent with Doppler effect, another is an amplification factor which enhances the mean drift coefficient. At a relatively low Froude number, the mean drift forces through Aranha's far field method and the Neumann-Kelvin linearization match each other well. However, as the Froude number increases, the shift impact and the enhancement factor between these two methodologies significantly differ.

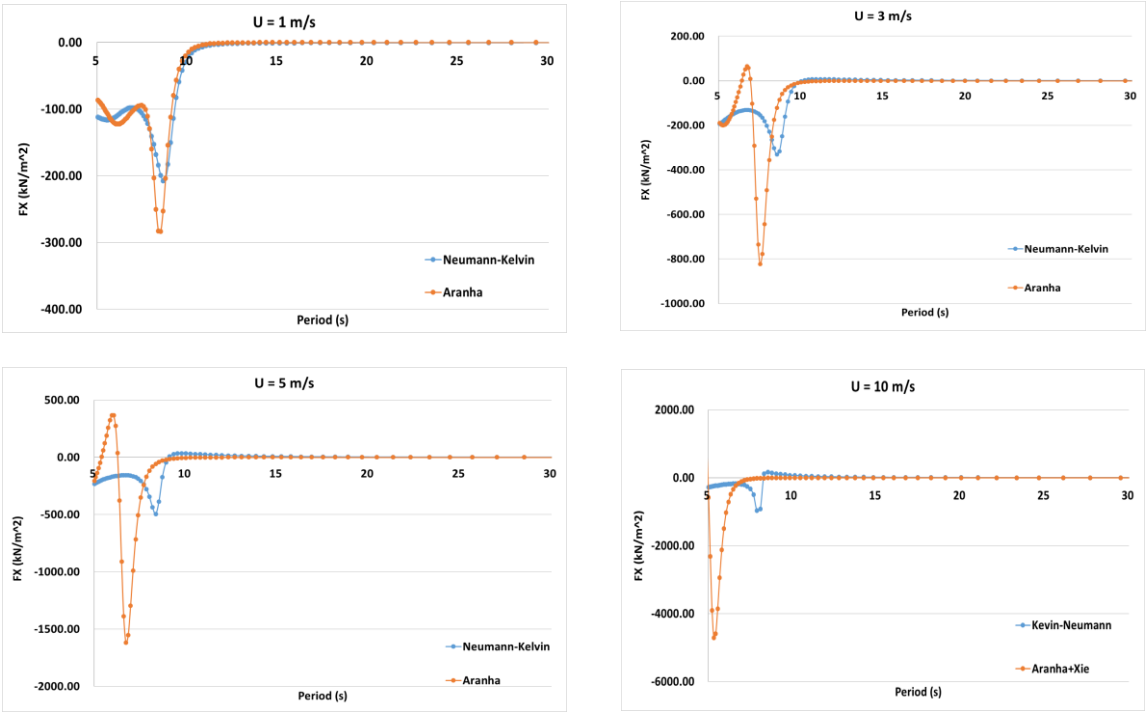

Figure 4.1. The mean drift force in X direction through Aranha's method and the Neumann-Kelvin linearization, with wave direction = cur direction = 180 deg, U = 1m/s, 3m/s, 5m/s, 10m/s (Fn = 0.051, 0.152, 0.253, 0.505).

One of the assumptions in Aranha's method is the $(U/c)^2$ (where c = g/ω) is a small number. It can be seen that as the current velocity or forward speed increases, $(U/c)^2$ increases significantly. As a result, for certain frequency points the mean drift force presents an opposite direction of the incident wave, which lacks physical meaning. On the other hand, it has a problem of numerical stability for short waves, whose reason is that the diffraction effects are not considered within this momentum and energy method. Therefore, Aranha's far field formula may meet limitations with either a relatively high forward speed or short waves.

4.5. Numerical Study of the Mean Drift Force with an Arbitrary Basis Flow

In seakeeping problems, mean drift loads with forward speed or current with respect to the vessel's fixed longitudinal direction have been mainly considered. However, in maneuvering problems, lateral speed and angular velocity in yaw motion should also be taken into consideration. The vessel's speed or the current velocity can be written as:

$$\boldsymbol{W} = (U - \Omega_R y')\boldsymbol{i} + (V + \Omega_R x')\boldsymbol{j} \tag{4.26}$$

Where U and V are the forward and lateral speed, Ω_R is the angular velocity in yaw motion. x' and y' are the vessel-fixed coordinates. By substituting this speed into the second-order wave loads, the mean drift force can be numerically estimated with an arbitrary basis flow through the Neumann-Kelvin linearization.

In this study, an FPSO hull form was selected for the numerical model. Numerical results of the mean drift loads in the vessel's fixed longitudinal and lateral direction that are considered as crucial parameters in maneuvering in waves have been presented with multiple wave and current directions.

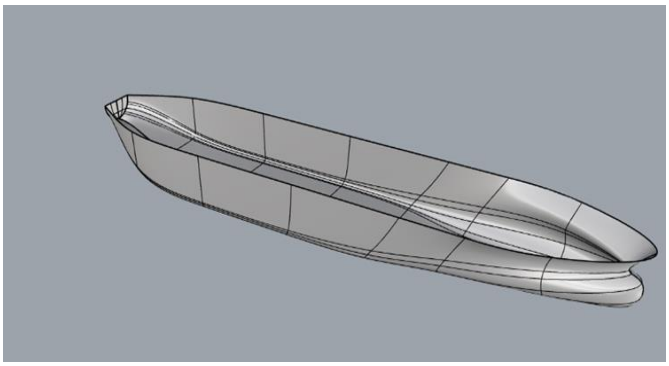

Figure 4.2 Numerical model of an FPSO

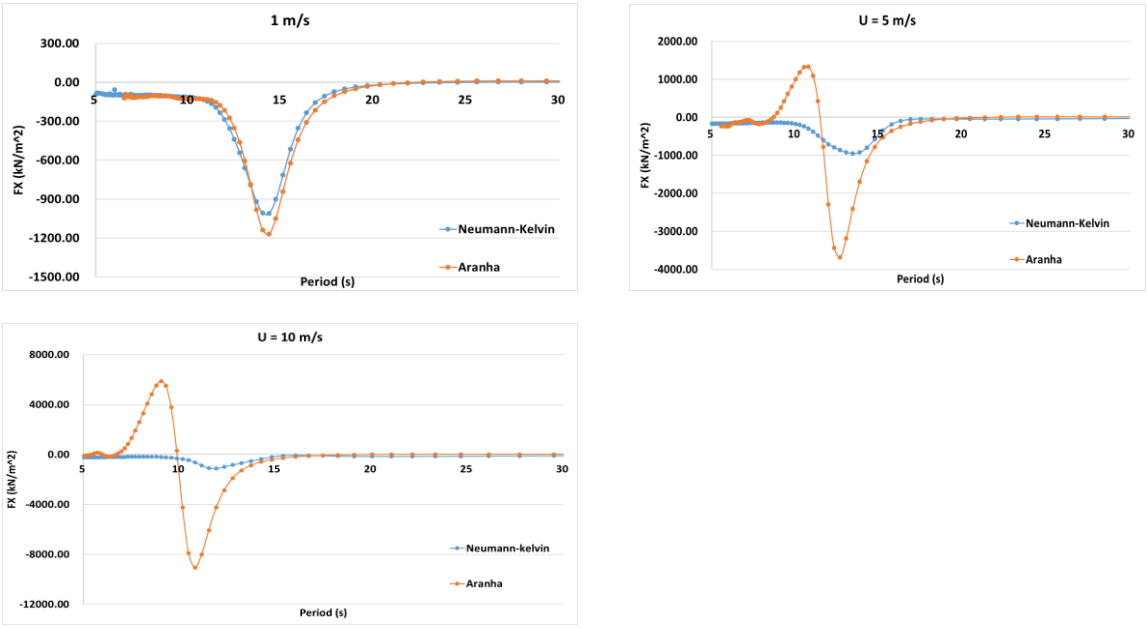

Figure 4.3. Comparison of the mean drift force in X direction through Aranha's far field method and the Neumann-Kelvin linearization, wave direction = cur direction = 180 deg, U = 1m/s, 5m/s, 10m/s (Fn = 0.018, 0.092, 0.184).

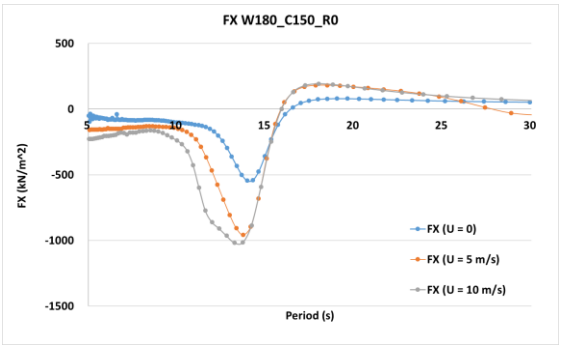

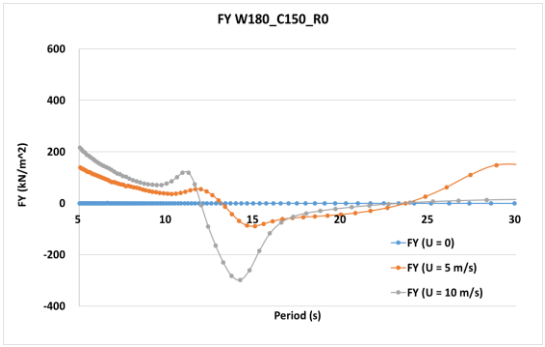

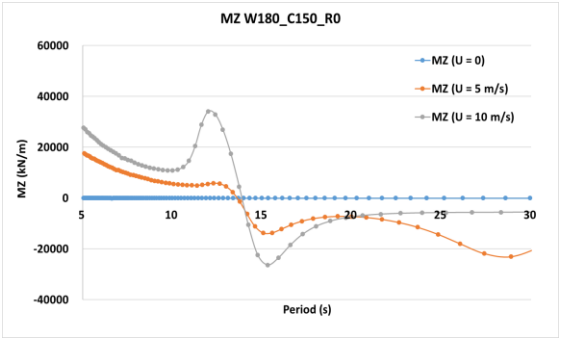

Figure 4.4. Mean drift loads in waves and currents with multiple directions (wave direction = 180 deg, current direction = 150 deg, Ω_R = 0 rad/s).

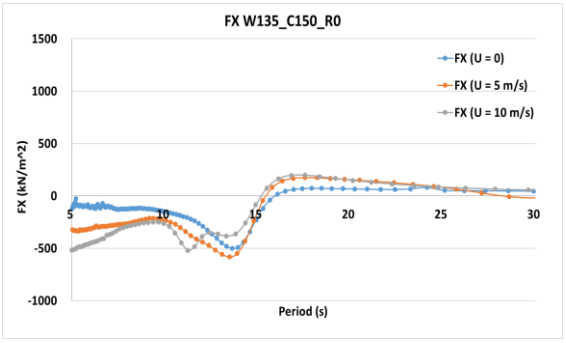

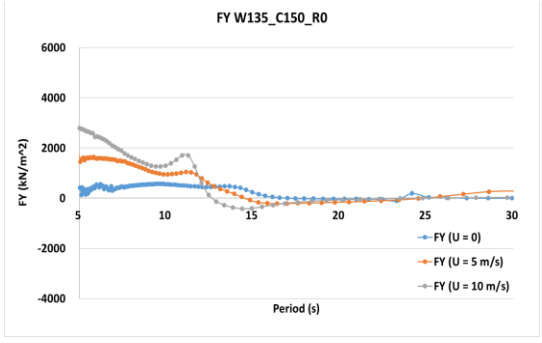

Figure 4.5. Mean drift loads in waves and currents with multiple directions (wave direction = 135 deg, current direction = 150 deg, Ω_R = 0 rad/s).

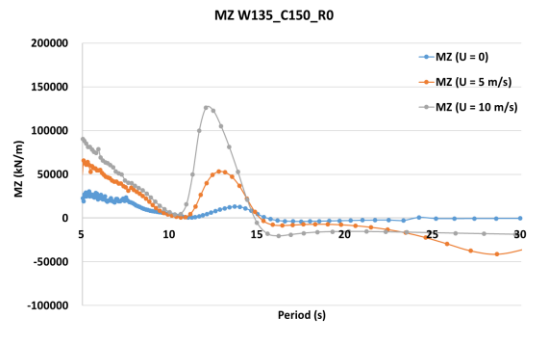

Figure 4.5. Continued.

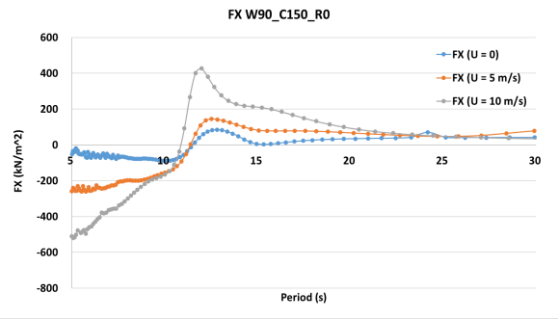

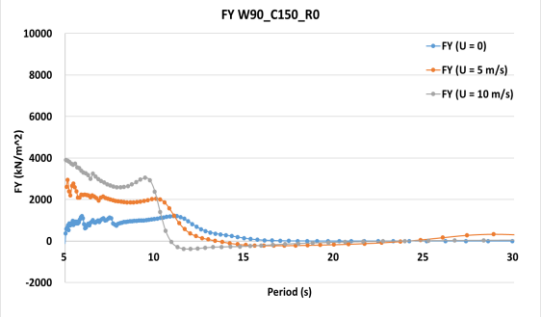

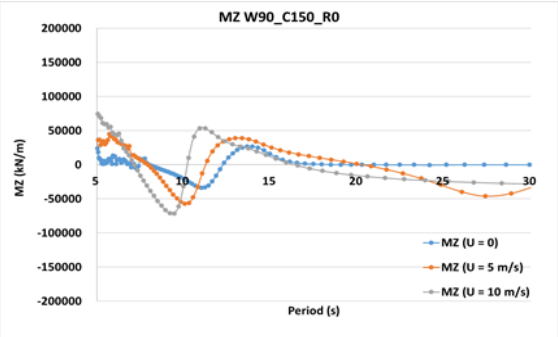

Figure 4.6. Mean drift loads in waves and currents with multiple directions (wave direction = 90 deg, current direction = 150 deg, Ω_R = 0 rad/s).

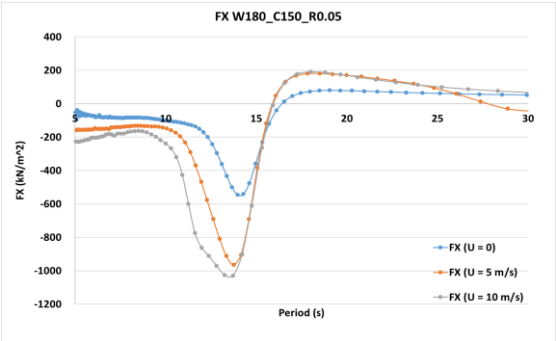

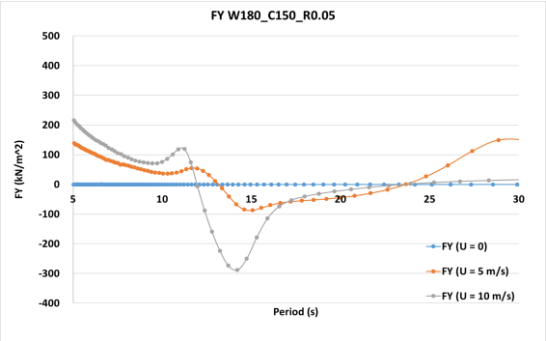

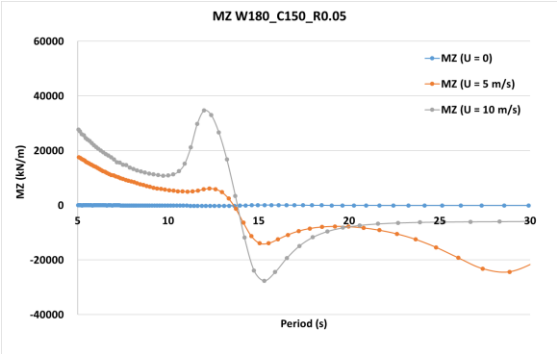

Figure 4.7. Mean drift loads in waves and currents with multiple directions (wave direction = 180 deg, current direction = 150 deg, Ω_R = 0.05 rad/s).

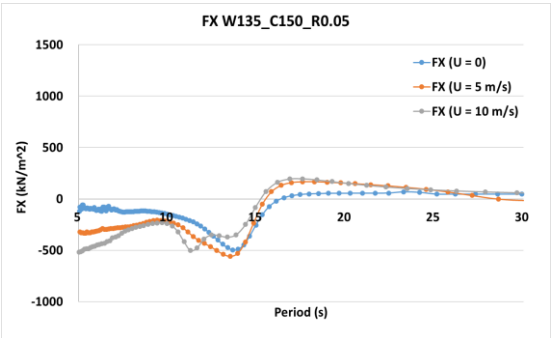

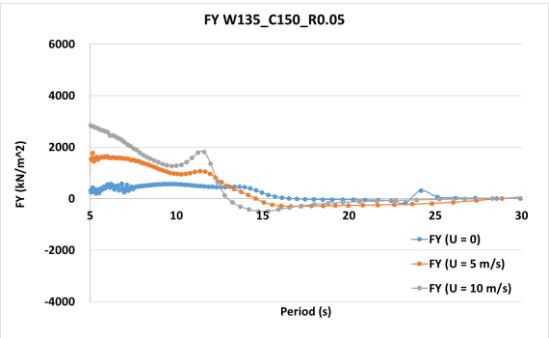

Figure 4.8. Mean drift loads in waves and currents with multiple directions (wave direction = 135 deg, current direction = 150 deg, Ω_R = 0.05 rad/s).

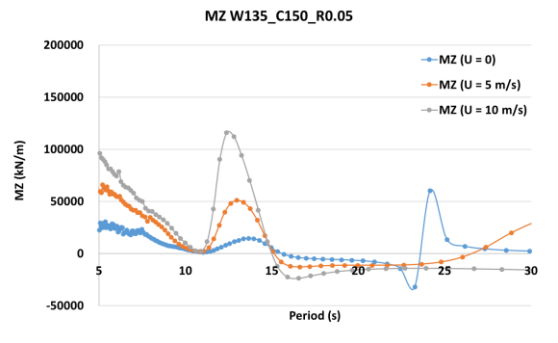

Figure 4.8. Continued.

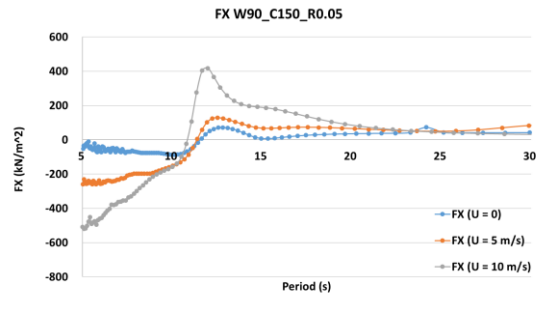

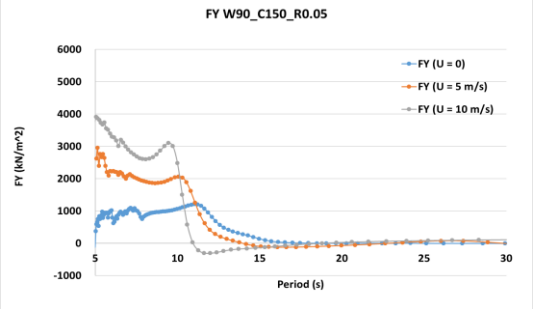

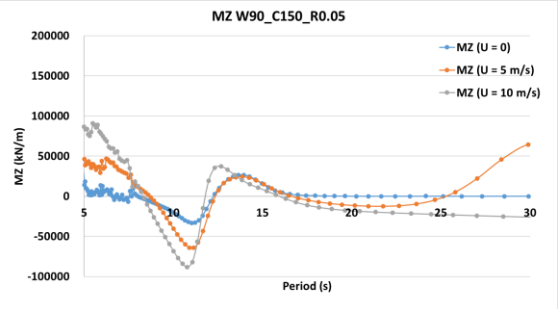

Figure 4.9. Mean drift loads in waves and currents with multiple directions (wave direction = 90 deg, current direction = 150 deg, Ω_R = 0.05 rad/s).

From Figures 4.3 to 4.9, the parameters including the 2nd-order horizontal mean drift loads that are crucial in maneuvering in waves have been numerically estimated through the Neumann-Kelvin linearization. It can be seen that the effect of angular velocity on the mean drift loads in waves is not obvious, compared with the effect of the vessel's forward speed and the wave direction with respect to the vessel's longitudinal direction. When the vessel's speed is zero, the numerical results are the mean drift loads in the wave only case. As the vessel's speed increases, the mean drift loads present the shifting effect and the coefficient amplitude corresponding to each encounter frequency also varies. It should be noted that as the encounter frequency increases, the effect of the vessel's velocity on the mean drift loads increases, which presents an obvious discrepancy compared with the low wave frequency cases. Therefore, the mean drift loads of a maneuvering vessel in waves is a complex function of wave direction, vessel's speed with respect to the vessel's longitudinal direction and the angular velocity in yaw motion.

4.6. Conclusion

The mean 2nd-order wave forces and moments from a seakeeping linearized problem with current was estimated through Aranha's formula, a far field method and Neumann-Kelvin linearization, a near field pressure integration method.

In the numerical study, both Aranha's formula and the Neumann-Kelvin linearization provide a reasonable estimation at low Froude number for a vertical cylinder. As the Froude number increases, the numerical results from Aranha's formula lack of physical meaning, due to its assumption of low current speed. The Neumann-Kelvin linearization provides a more robust numerical estimation and converges to the expression

of the mean 2nd-order forces and moments in the previous research when the basis flow reduces to zero.

In the problem of maneuvering in waves, an arbitrary basis flow including lateral speed and angular velocity that are usually not considered in the seakeeping problems should be taken into consideration. A numerical FPSO hull form model has been considered and the corresponding horizontal mean drift loads with an arbitrary flow that are crucial in studying the maneuvering behaviors in waves have been numerically estimated. Through the comparison of the horizontal wave loads in various wave directions and speeds, it can be concluded that the mean drift loads of a maneuvering vessel in waves is a complex function of environmental conditions. This work provides a meaningful numerical contribution for the investigation of the maneuvering in waves problem in the next section.

5. A FRAMEWORK OF NUMERICALLY EVALUATING A MANEUVERING VESSEL IN WAVES*

5.1. Introduction

A ship's maneuverability is typically only considered in calm water in most previous research (See e.g., Nomoto et al, 1957, Barr and Webster, 2021), while a seagoing vessel maneuvering in waves is more often the actual critical scenario. This research on maneuvering in waves is practically significant, considering navigation safety. This is particularly true considering the IMO Energy Efficiency Design Index (EEDI) to reduce greenhouse gas and the attraction of significantly reducing the propulsion power in a vessel so much so that it may not be able to safely maneuver in a storm. Therefore, the minimum power must be determined considering its ability to safely navigate or maneuver in waves. There are several existing methods to study ship maneuverability in waves, such as model tests and numerical simulation that can be generally classified as CFD methods, two-time scale methods, and hybrid approaches.

The experimental method is a practical and reliable methodology to investigate the ship's maneuverability in waves. Turning circles and zig-zag tests in regular waves have been conducted to analyze various parameters such as wave length, wave direction and

* Part of this section is reprinted with permission from "A Framework of Numerically Evaluating the Maneuvering Vessel in Waves" by Zhitian Xie, Jeffrey Falzarano, 2020. *Journal of Marine Science and Engineering*, 8(6), 392, Copyright (2020) by MDPI.

ship's loading condition's effects on maneuvering motions (Ueno et al, 2003; Kim et al, 2019). However, specific model tests are time consuming, expensive, and should only be considered for the validation of more general numerical approaches.

As for the numerical simulation, CFD methods in principle consider all physics but still needs further development in order to reach the level of industrial applicability. Islam et al. (2018) applied an open source RANS solver, OpenFOAM to simulate hydrodynamic derivatives and his results matched well with two sets of experimental data, with the exception of the pure yaw cases. Uharek et al (2018) showed that the RANS code Neptuno was able to predict the mean drift loads for vessels maneuvering in oblique regular waves and that the inertial contributions cannot be neglected. Wang et al (2018) applied a CFD solver based on OpenFOAM and applied the overset grid technique and six DoF module to solve for the motion of the free-running ship with twin rotating propellers and turning rudders. However, CFD's current large requirement of computational resources and technical difficulties has confined it to the research communities worldwide. The application to propellers and rudder models under large attack angle suggest that fulfillment of the real time simulation requirement is hardly to be satisfied from a realistic point of view (Zhang et al, 2017). An alternative to CFD methods are the two-time scale method and the hybrid approach, both of which are based on potential flow methods to consider the wave effect. As for the hybrid approach, it combines the maneuvering motion and wave-induced motion into the rigid body motion equations to simulate a vessel's maneuverability (Skejic, 2013; Bailey et al, 1997), but ignores the effect of the second-order wave loads. Through the investigation by Lee et al

(2009) regarding the effects of waves on ship's maneuverability, it can be concluded that the second-order wave loads present a significant effect on the trajectory of turning and zig-zag tests. On the other hand, the two-time scale method considers and separates the ship motions into the wave frequency and low frequency components, and by doing this, it is possible to consider the second-order wave loads and motions to improve its accuracy. Skejic and Faltinsen (2008) applied the two-time scale approach to analyze ship maneuvering in regular waves, by evaluating the wave drift forces through four different strip theory methods and considering that when the ship has a mean forward speed and undertakes maneuvering in waves, the wave-frequency problem is affected by the slowly-varying maneuvering. Seo and Kim (2008) developed a coupled analysis of the maneuvering and seakeeping problems through a two-time scale approach, where the wave loads were estimated using a Rankine panel method in the time domain. Lee and Kim (2020) used a 3D time-domain Rankine panel method to analyze the ship motion due to the waves and near-field method to consider the wave drift loads. It can be concluded that the seakeeping quantities, such as ship motion and wave drift force, are significantly affected by both forward speed and side slip speed. Moreover, the accuracy of turning simulation results are also closely related to the prediction of wave drift loads. Chillcce and Moctar's (2018) solution assumed that the calm water hydrodynamic parameters and the wave induced forces do not interact and applied a RANS approach to obtain the calm water forces and a 3D Rankine source boundary element method to consider the wave-induced second-order loads. Their results showed that the ship's drift in turning circle can be accurately captured by considering the mean second-order wave loads.

A derivation and full expression of the second-order wave loads acting on a floating body was presented in our previous sections through a direct pressure integral method. While considering the mean wave forces and moments acting on a floating body with speed, the Neumann-Kelvin linearization has been investigated and compared with Aranha's far field formula and proven to be robust and less sensitive in high Froud number.

With the numerical tool in calculating the 2^{nd}-order wave loads and the effect of the forward speed or current, the research herein introduces and explains the theoretical derivations and the framework of coupling the seakeeping and maneuvering modules to numerically model a maneuvering vessel in waves involving the second-order wave loads. The combination work on seakeeping problems herein is based upon our original and systematic perturbation approach to derive the hydrodynamic forces acting upon the hull of a floating body in waves. The Neumann-Kelvin linearization method has been applied to consider the vessel forward speed's effect in the seakeeping problem and then coupled with the maneuvering problems in the two-time scale method. Moreover, this approach has been applied to the KVLCC and KCS models as an example and compared to available experimental results of maneuvering in waves. Through the comparison with the model tests, this framework herein has been found to be an accurate and efficient approach to study maneuvering of ships in waves. This research can be also undertaken to expand its range of applicability, including the minimum powering requirements for ships in adverse conditions, which is important considering the IMO Energy Efficiency Design Index (EEDI) to reduce the greenhouse gas and the attraction of significantly reducing the propulsion power in a vessel.

5.2. The 3D Maneuvering Mathematical Model

The mathematical model of the maneuvering motions of ships in calm water is now well established. Linear equations of motions will be considered in this scenario, in motion modes of surge, sway, and yaw, while the motions of roll, pitch, and heave are often neglected and not considered in such analysis. Eulerian or vessel fixed coordinate systems with axes at the midship can be applied to describe the ship motions. The hydrodynamic forces and the modes of vessel motions can be expressed as:

$$\boldsymbol{X_F = m(\dot{u} - rv - x_G r^2)} \tag{5.1}$$

$$\boldsymbol{Y_F = m(\dot{v} + ur + x_G \dot{r})}$$

$$\boldsymbol{N_F = I_Z \dot{r} + m x_G (\dot{v} + ur)}$$

where u and v are the longitudinal and lateral velocities and r is the yaw rate. I_z is the moment of inertia with respect to the vertical axis going through the midship point, therefore the horizontal distance between the center of gravity and the midship point is x_G. The above hydrodynamics forces and moments acting on the ship can be developed through perturbations, where the hydrodynamic loads are proportional to the perturbation quantities. X_{drift} stands for the longitudinal wave drift loads in the seakeeping problem.

$$\boldsymbol{X_F = X_{F_{\dot{u}}} \dot{u} + X_{F_u} \Delta u + X_{F_{drift}}} \tag{5.2}$$

$$\boldsymbol{Y_F = Y_{F_{\dot{v}}} \dot{v} + Y_{F_v} v + Y_{F_{\dot{r}}} \dot{r} + Y_{F_r} r + Y_{F_{drift}}}$$

$$\boldsymbol{N_F = N_{F_{\dot{v}}} \dot{v} + N_{F_v} v + N_{F_{\dot{r}}} \dot{r} + N_{F_r} r + N_{F_{drift}}}$$

Combing the above sets of equations sets with only the linear terms, the linearized equations of maneuvering ship's motion can be expressed as follows.

$$\left(X_{F_{\dot{u}}} - m\right)\dot{u} + X_{F_u}\Delta u + X_{F_{drift}} = 0 \tag{5.3}$$

$$\left(Y_{F_{\dot{v}}} - m\right)\dot{v} + Y_{F_v}v + \left(Y_{F_{\dot{r}}} - mx_G\right)\dot{r} + \left(Y_{F_r} - mu_0\right)r + Y_{F_{drift}} = 0$$

$$\left(N_{F_{\dot{v}}} - mx_G\right)\dot{v} + N_{F_v}v + \left(N_{F_{\dot{r}}} - I_Z\right)\dot{r} + \left(N_{F_r} - mx_G u_0\right)r + N_{F_{drift}} = 0$$

While numerically evaluating a maneuvering ship in waves, there are two modules, namely the seakeeping module and the maneuvering module in each time step, which take the current environmental parameters such as the vessel speed, vessel heading, and wave direction as the input and output the updated input for the next time step. The numerically evaluated hydrodynamic coefficients including the vessel hull, rudder induced loads and the drift loads considering the wave drift damping are all considered as the internal parameters in these two modules. The flow chart of the coupling effect of the seakeeping and maneuvering analysis in terms of slowly varying mean second wave loads that also change the ship speed and wave heading is be presented in Figure 5.1.

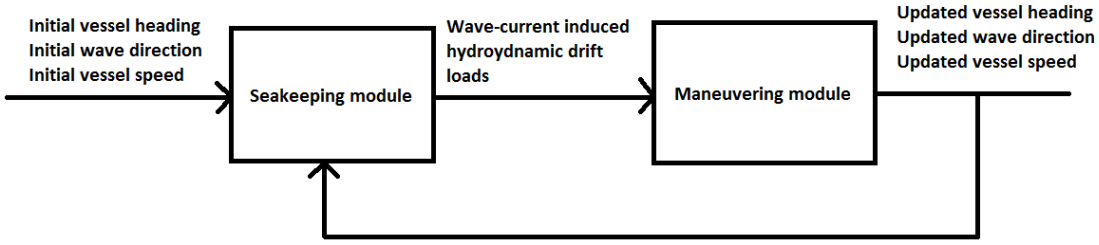

Figure 5.1. Process diagram of numerical maneuvering model.

5.3. Simulation of Maneuvering in Waves

In this study, two vessels were selected, a tanker hull the KVLCC and a containership hull KCS. For the KVLCC in full loading condition: the Lpp is 320 m, the draught is 20.8 m, and the displacement is 312, 622 m^3. Four regular waves have been selected, whose ratios of the wave length and the vessel length are 1.25, 1, 0.75 and 0.5, respectively. The vessel's starting speed is 9.3 knots. Both the turning circle trajectory and zig-zag test time series were numerically evaluated, to investigate the maneuverability (See e.g. ABS Guide for Vessel Maneuverability, 2006). For the KCS containership: the Lpp is 230 m; the draught is 10.8 m; the displacement is 52030 m^3. The experimental maneuvering results carried out by Hiroshima University (Available online, 2020) were chosen as the reference for the turning circle trajectory in both the calm water and regular wave with wave direction of 180 degrees, whose wave length is equal to the vessel length. The vessel's starting speed in both the calm water and wave tests is Fn = 0.16 (corresponding to a full scale 14.5 knots). In the wave test, the regular wave's height is 3.61 m in the full scale with a full-scale wave period of 12.14 s.

Figures 5.2 and 5.3 present the KVLCC's turning trajectories in regular waves with starboard rudder of 35 degrees. In calm water, the turning trajectory will converge to a stable circle after continuous turning. Compared with the turning trajectories in the calm water, the wave drift loads coupled with wave drift damping drives the vessel turning trajectories to present a horizontal shift path, instead of the stable converged circle. It can be seen that as the wave length decreases, this drifting path is more obvious.

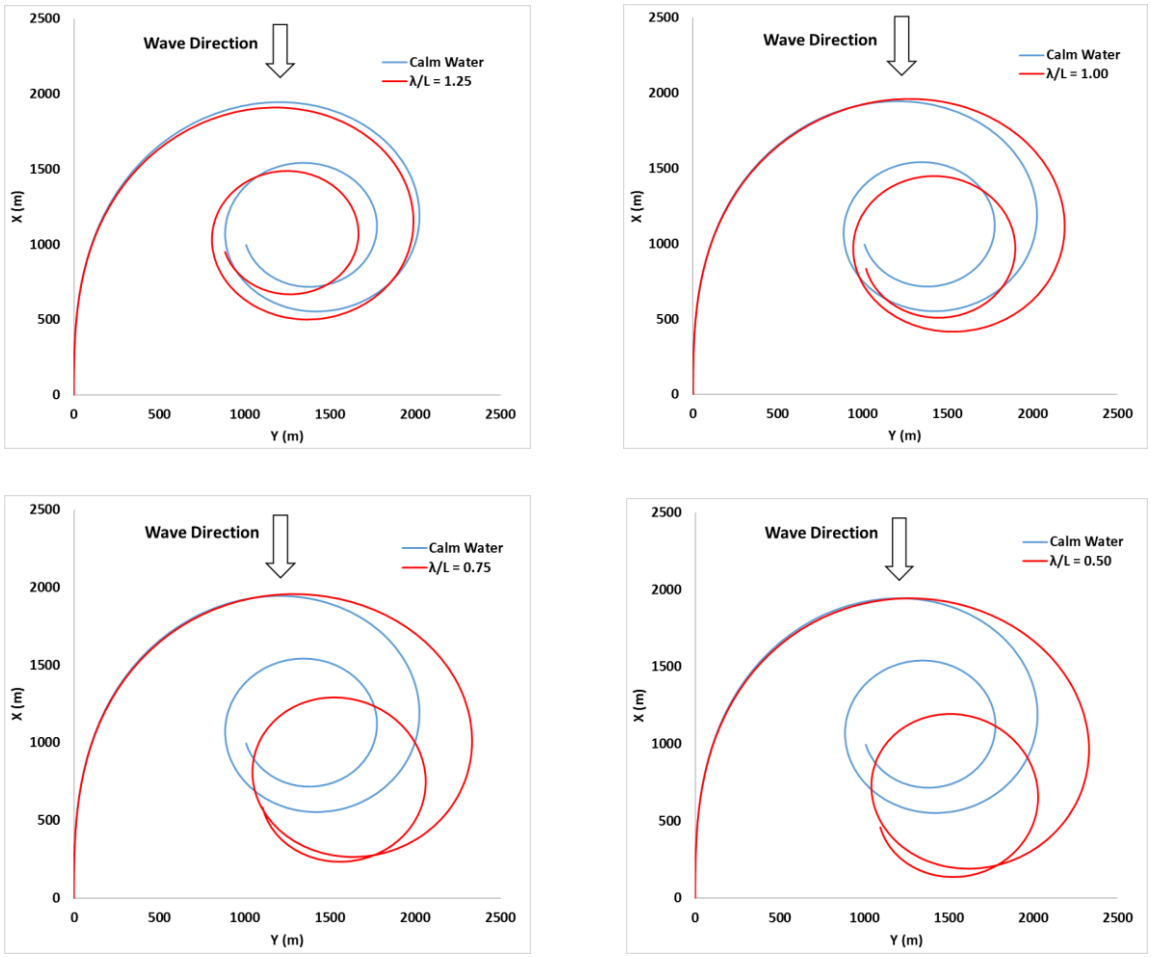

Figure 5.2. KVLCC's starboard-side 35 degrees turning trajectories in regular waves with 180 degrees at t = 0.

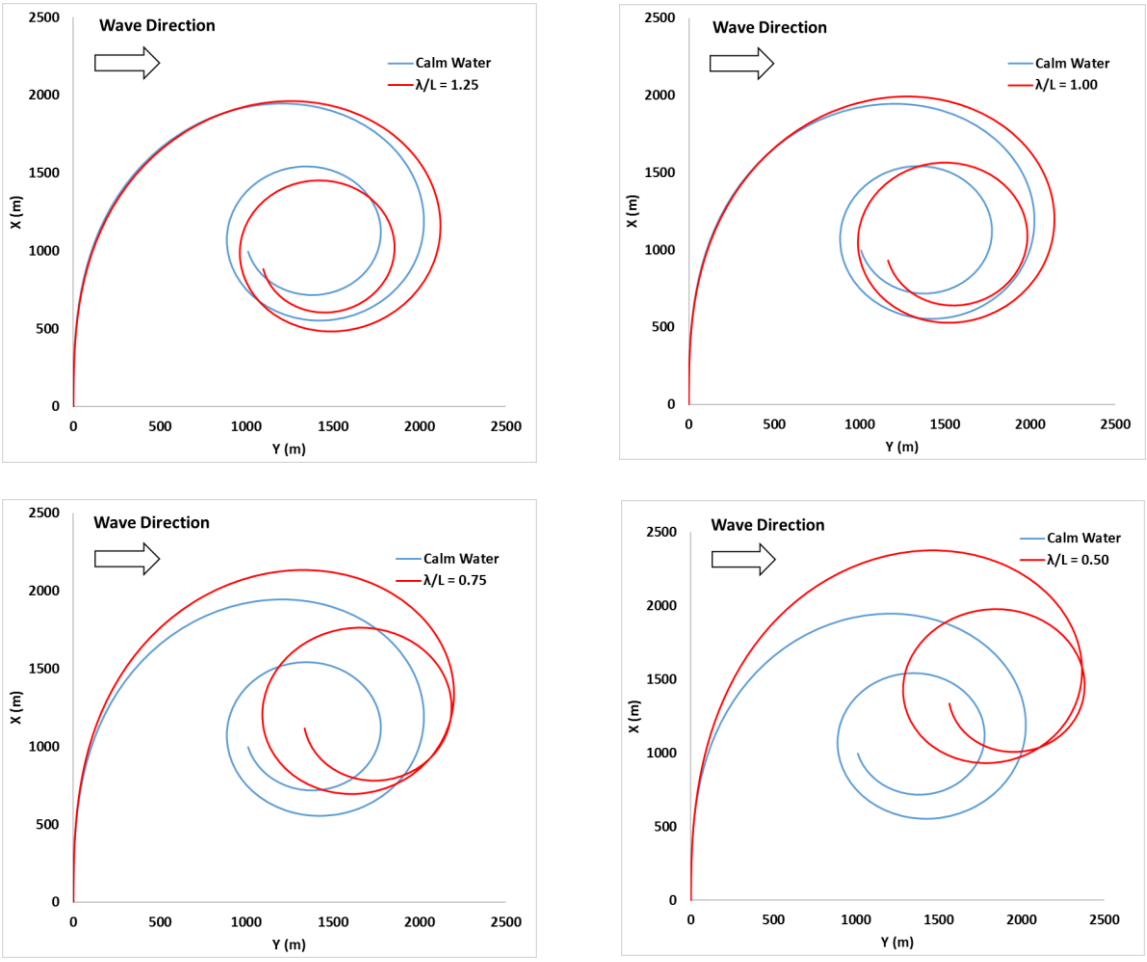

Figure 5.3. KVLCC's starboard-side 35 degrees turning trajectories in regular waves with 90 degrees at t = 0.

Figures 5.4 and 5.5 present the 20/20 deg zig-zag turning test in regular waves with various wave lengths. Compared with the cases in heading sea where the vessel heading presents symmetry characteristic about positive and negative headings, the vessel heading in the cases of beam sea at the starting point presents asymmetric characteristic. In Figure 5.4, it can be observed that the period of the rudder angle fixed at the 20 deg presents an increasing trend with the zig-zag round. When the wave length is equal to the vessel length,

the vessel turning rate is higher than the cases with other wave lengths. In Figure 5.5, as the wave length decreases in beam sea, the period of the fixed rudder angle is unbalanced about the positive and negative sides, presenting an asymmetric characteristic.

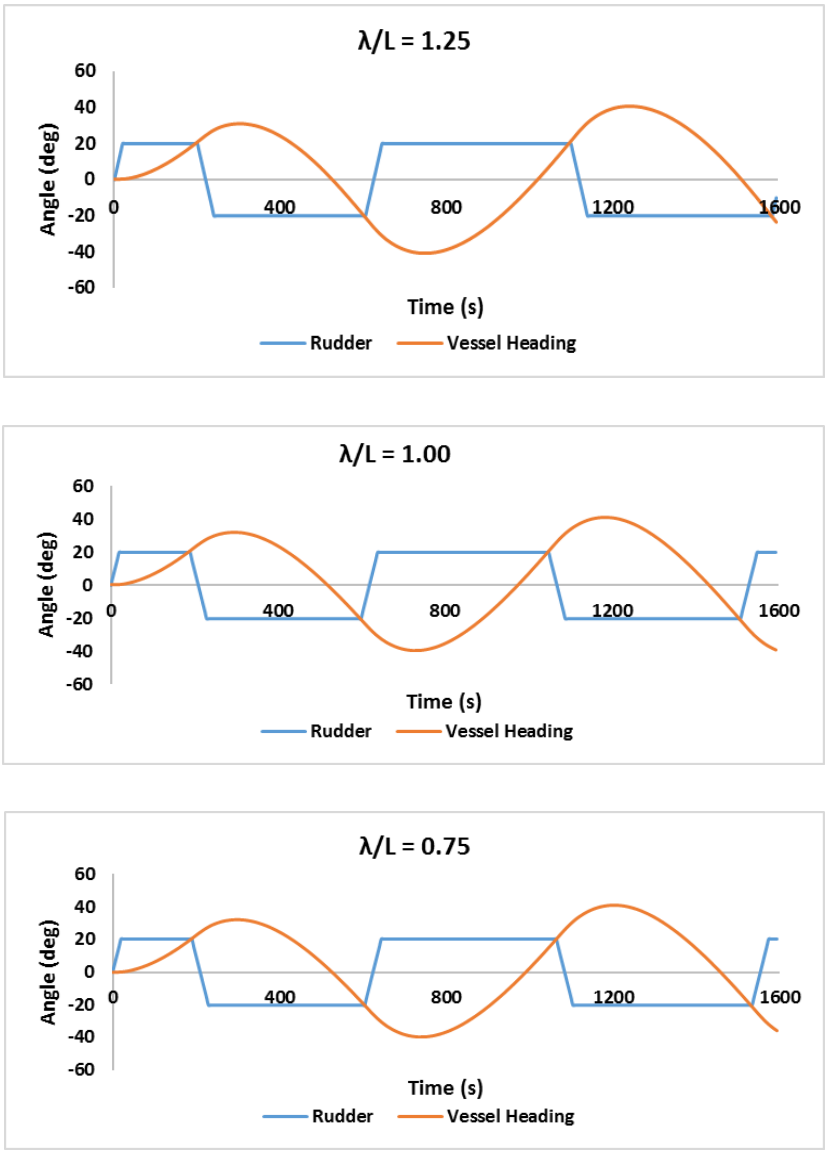

Figure 5.4. KVLCC's 20/20 degrees (starboard-side) Zig-Zag tests in regular waves with 180 degrees at t = 0.

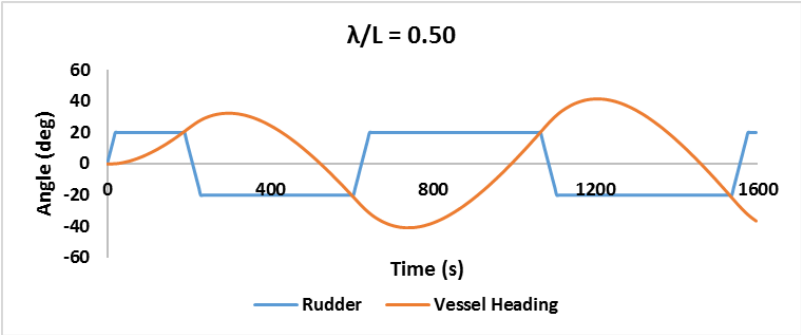

Figure 5.4. Continued.

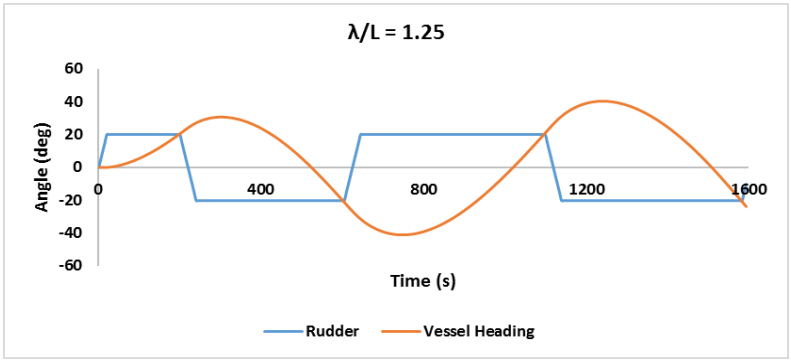

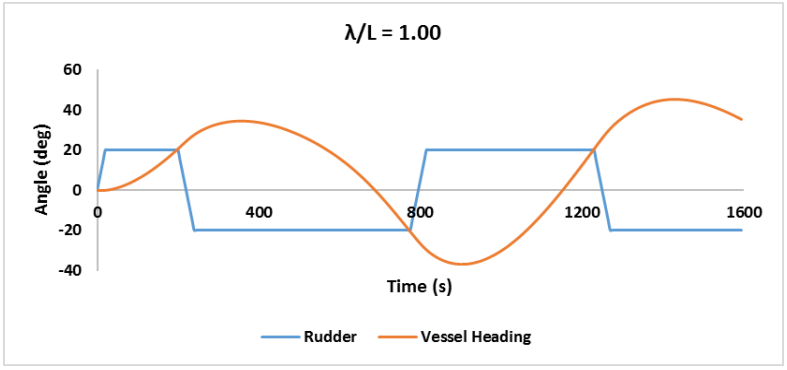

Figure 5.5. KVLCC's 20/20 degrees (starboard-side) Zig-Zag tests in regular waves with 90 degrees at t = 0.

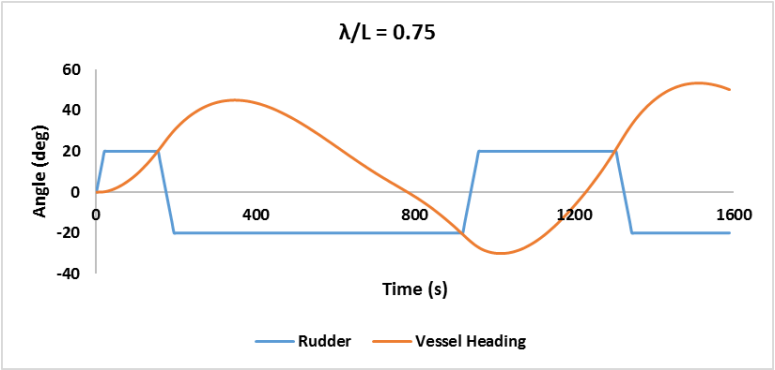

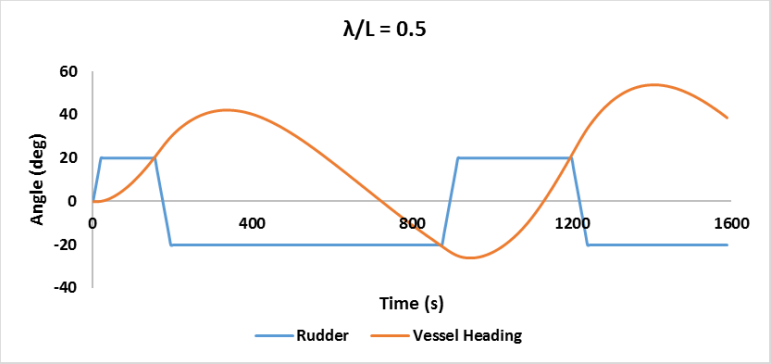

Figure 5.5. Continued.

As shown in Figures 5.6 to 5.10, the numerically simulated turning trajectories for the KCS vessel have been presented and compared with the model test results in both calm water and regular waves.

In calm water, as can be seen in Figure 5.6, the numerically simulated turning trajectory shows an excellent match with the experimental results, providing a convincing comparison basis: the diameter of the turning circle through the numerical simulation is 397.3 m, only 8.64% higher than that of the model test, which is 365.7 m.

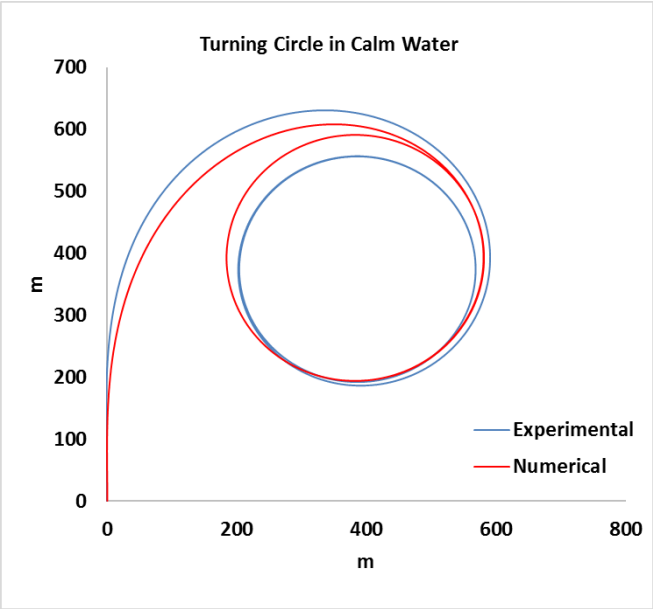

Figure 5.6. KCS's experimental and numerical starboard-side 35 degrees turning trajectories in calm water.

To precisely describe the turning trajectories in waves, multiple parameters including the diameter, the drift angle and the drift distance have been selected in present study. The drift angle is defined as the angle between wave propagating direction and vessel traveling direction in which the wave encounter angle is −90 deg, while the drift distance is defined by successive positions with a wave encounter angle of −90 deg (Ueno et al, 2003). Two measures of diameter have been considered, namely the diameter measured along with the wave direction (V1 and V2) and the diameter measured perpendicular to the wave direction (H1, H2). These parameters are shown in Figure 5.7.

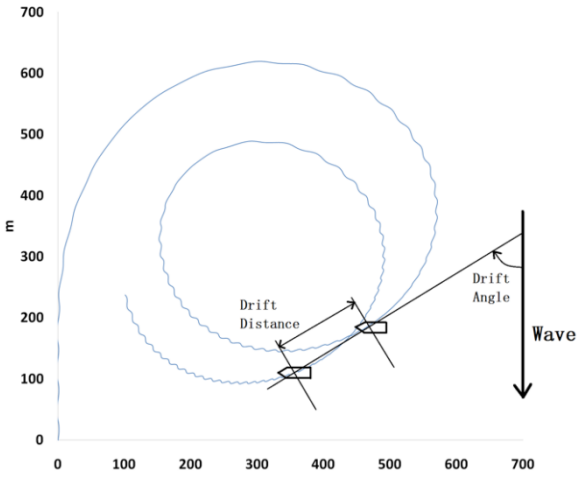

(a)

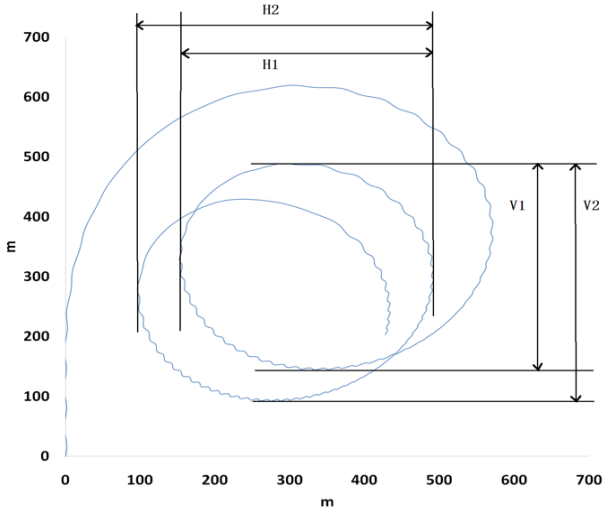

(b)

Figure 5.7. Parameters of the turning trajectory in waves: (a) drift angle and drift distance; (b) horizontal and vertical diameter of the turning trajectory.

In Figures 5.8 to 5.10, a turning trajectory that presents a horizontally shifted path due to the waves is observed in the KVLCC model and can also be observed in both the KCS model's numerical and experimental results. It can be seen in Figure 5.8 that there is

a relatively obvious trajectory shift at the early stage between the numerical and experimental results, which leads to the difference of the corresponding drift angle and drift distance. A similar shift between these two methods can be also found in the calm water results as shown in Figure 5.6. One reason for this phenomenon is the physical model's sensitivity to the rudder, which contributes to the discrepancy of the horizontal hydrodynamic loads due to the rudder perturbations, and leads to a shift between the numerical and experimental trajectories. Another reason is the variance of the wake fraction being dependent on the propeller side-wash angle (Sutulo and Soares, 2019), which thus changes the propeller surge force in the model test, while this component was considered as a constant value in the numerical simulation.

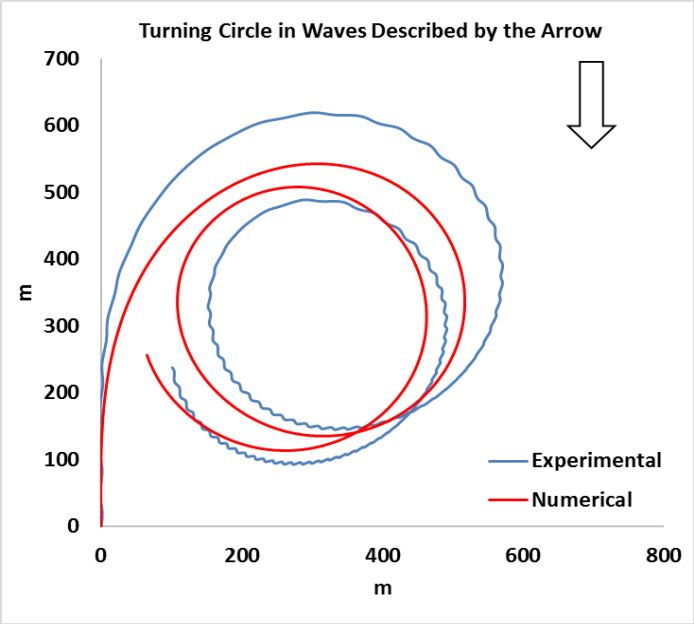

Figure 5.8. KCS's experimental and numerical starboard-side 35 degrees turning trajectories regular wave with 180 degrees at t = 0.

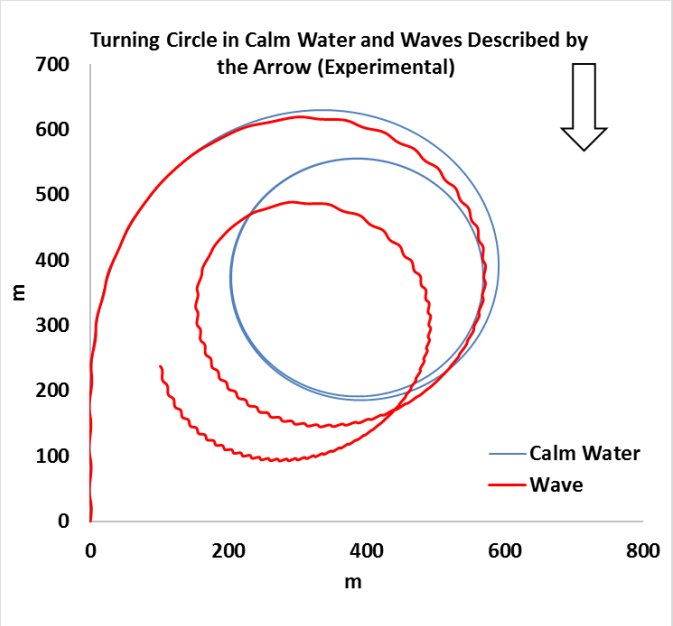

Figure 5.9. KCS's experimental starboard-side 35 degrees turning trajectories in calm water and regular wave with 180 degrees at t = 0.

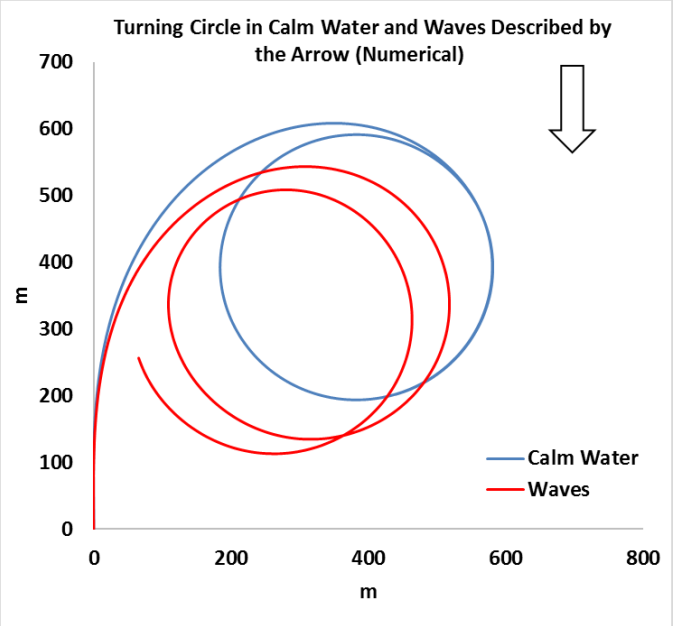

Figure 5.10. KCS's numerical starboard-side 35 degrees turning trajectories in calm water and regular wave with 180 degrees at t = 0.

Similar discrepancies between the model tests and numerical simulations can also be found in Zhang's research (2017), as well as Lee and Kim's research (2009) through the double-body linearization results with and without a vortex sheet. Also, this is the case in Chillcce and Moctar's work (2018) who applied a RANS computer code to obtain calm water forces and a 3D RANKINE source method to consider the second-order wave forces. It should also be noted that the discrepancies between the numerical and experimental results in most recent research also increase in the later stage of the turning trajectory. As is the case in the present study, after the early stage of the turning trajectory, the numerical simulation matches well with the experimental data, accurately capturing the main turning trajectory's drifting path. Moreover, the numerically simulated turning trajectory's diameters have shown a good match with the model test within a 7% discrepancy as presented in Table 1: the H1, V1, H2, and V2 present −2.47%, 6.94%, 0.65%, and −3.48% discrepancies from the model test, respectively.

Table 5.1. Parameters of the turning trajectories in calm water and waves.

	D	**H1**	**V1**	**H2**	**V2**	**Drift angle**	**Drift distance**
Unit	m	m	m	m	m	m	m
Model test	365.7	339.8	344.3	396.1	396.5	51.9	82.6
Numerical simulation	397.3	331.4	368.2	393.5	382.7	65.6	72.5

Therefore, the current framework of coupling the seakeeping and maneuvering modules provides a practical and accurate numerical methodology through the experimental validation, to predict the unconstrained vessel's maneuvering in waves. Compared with the most recent research (See e.g. Zhang, 2017; Chillcce and Motar, 2018), this framework presents a comparatively accurate prediction of the later stage of the turning trajectory in waves. Moreover, with a thorough physical model and explanation of the second-order wave loads through the potential flow theory, this framework is numerically efficient, especially considering CFD's current large requirement of computational resources (Islam and Soares, 2018; Wharek and Cura-Hochbaum, 2018; Wang et al, 2018). In the future research, the sensitivity of the physical model in this framework to various hydrodynamic and wave parameters can be conducted and extended for the design of vessels (Hirdaris et al, 2014).

5.4. Conclusion

In this section, a framework that considers the coupled maneuvering and seakeeping problems that involves an accurate prediction of the second-order wave loads of a maneuvering vessel in waves has been introduced and validated. With the help of the established framework through the two-time scale method and the Neumann-Kelvin linearization, the numerical simulations of maneuvering vessels in waves have been conducted to obtain the turning trajectories and the zig-zag test time series for the KVLCC and KCS models.

According to the numerical simulations, the wave drift loads with wave drift damping drives the vessel turning trajectory away from the calm water trajectory, resulting

in a drifting path. As the wave length decreases, this drifting phenomenon is more pronounced. It can also be concluded that maneuvering in beam seas also presents an asymmetric characteristic for the vessel heading in the zig-zag tests. Through the comparison with the KCS model test and other recent approaches, the corresponding numerical result accurately captures the main characteristic of the turning trajectory, especially in the later stage. Therefore, the framework herein is an accurate and efficient approach to study the maneuvering of ships in waves. In future work, the current framework can be extended and contribute to the IMO standards for determining the minimum propulsion power to guarantee the maneuverability of vessels in adverse conditions.

With the numerical tools in both the 1^{st}-order and 2^{nd}-order hydrodynamic quantities, a optimization framework will be established through the genetic algorithms in the next section.

6. AN OPTIMIZATION FRAMEWORK OF A PARAMETRIC HULL DESIGN*

6.1. Introduction

With our improved hydrodynamic calculation tools, an optimization framework using genetic algorithms has been developed in this research, towards an automated parametric optimization of the Octabuoy semi-submersible design, a new floater concept designed for deep water areas. Compared with deep draft production units, such as SPAR or other deep draft semi-submersibles, the design of the shallow draught Octabuoy semi-submersible provides a floating system with improved motion characteristics, being less susceptible to vortex induced motions (VIM) in loop currents (Korbijn et al, 2005). Figure 6.1 (a) shows a view of the shallow draught Octabuoy semi-submersible platform.

The shallow draught Octabuoy semi-submersible consists of an octagonal shaped pontoon with a rectangular cross section and four circular columns. Parametric resonance is a phenomenon which may occur when a parameter in a mechanical system varies over time, which is different from ordinary resonance as it exhibits instability. Parametric instability describes a coupling between heave and pitch/roll and is known as the Mathieu effect in figure 6.1(b). It can be triggered by an oscillation hydrostatic stiffness in the vertical modes. It is possible to reduce the amplitude of the oscillating stiffness by varying

* Part of this section is reprinted with permission from "An Optimization Framework of a Parametric Octabuoy Semi-Submersible Design" by Zhitian Xie, Jeffrey Falzarano, 2020. *International Journal of Naval Architecture and Ocean Engineering*, 12, 711-722, Copyright (2020) by the Society of Naval Architects of Korea.

the cross-sectional area in the free surface zone. Therefore, on the top of each vertical column, there is a cone shaped section whose half height is located around the still waterline (Pettersen et al, 2007). The relatively large water plane area brings the floating system a high deck load capacity, which makes it a highly competitive solution compared to other semi-submersibles, on one hand. On the other hand, the decreased natural heave period due to the relatively large water plane area locates the floater in a wave period range with more wave energy in harsh sea conditions. A tuned mooring system has been proposed to ensure the improved heave motion characteristics compared to other semi-submersibles, making the floater suited for accommodating steel catenary risers (Korbijn et al, 2005). In this scenario, an optimization process can be developed to reduce the level of the motion response in harsh sea states, improving the shallow draught Octabuoy semi-submersible design's hydrodynamic performance.

Design optimization includes the selection of a set of variables to describe the design alternatives, objective function expressed in terms of the design variables to be minimized or maximized, a set of constraints expressed in terms of design variables and the optimized variables' values, while satisfying all the constraints. Therefore, optimization formalizes what designers have done philosophically and can be operationally used during the design process where analysis can be applied (Papalambros et al, 2000). Genetic algorithms (GAs) have been developed by John Holland (Holland, 1973; Holland, 1984) to design artificial systems that retains the significant mechanisms of natural systems including natural selection and natural genetics, which combine survival of the fittest among string structures with a randomized information exchange to

form a search algorithm. Compared with traditional optimization methods such as Calculus-based methods, the enumerative methods and the random method, genetic algorithms are theoretically and empirically proven to provide robustness, due to its direct use of coding, search from a population, blindness to auxiliary information and randomized operators. Moreover, genetic algorithms keep the balance between efficiency and efficacy in many different environments.

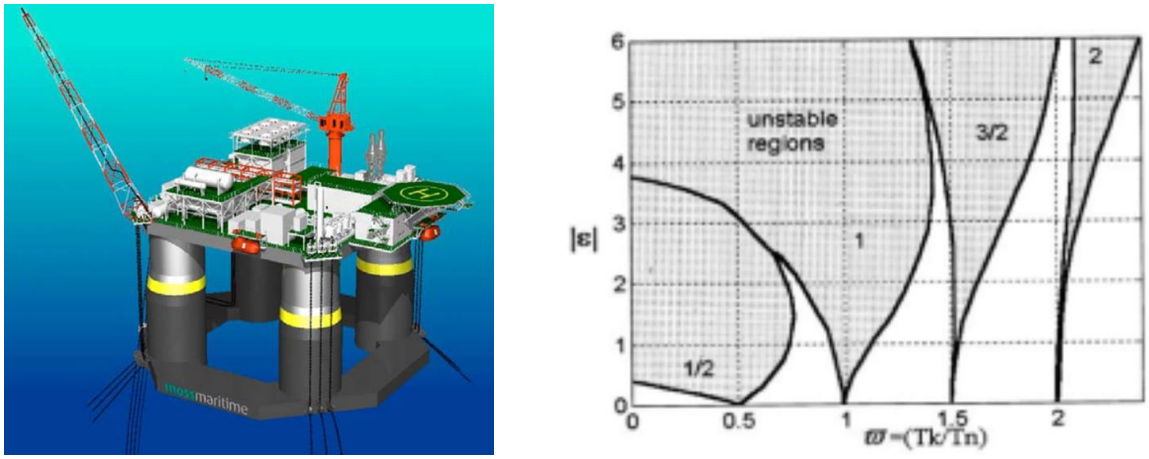

(a) (b)

Figure 6.1. (a) View of the shallow draught Octabuoy semi-submersible platform reprinted from (Korbijn et al, 2005), (b) General solution of the Mathieu differential equation.

In previous research, automated hull shape optimization procedures have been investigated and proven to be an efficient tool for the improvement of existing and the development of new system concepts in a short time (See e.g. Birk et al, 2001; Clauss et

al, 1996; Guha et al, 2016). Multi-objective optimizations towards a fully automated semi-submersible hull form have been conducted through the simulated annealing (SA) method (Park et al, 2015). It shows that the total hull height is proportional to the structural weight and inversely proportional to the heave motion. Non-dominated Sorting Genetic Algorithms (GA) have been employed along with radial basis functions towards a Tension Leg Platform (TLP) design to reduce the maximum dynamic tendon tensions (Zhang et al, 2018). It was found that the maximum dynamic tension shows a positive correlation with pontoon height and width, and a negative correlation with hull draft, column spacing and column diameter. The neural network prediction method and Inverse Multi-Quadric radial basis functions have been applied to estimate the hydrodynamics performances of different hull forms during the optimization process and proven to reduce the Semi-Submersible platforms' heave motion and total weight (Qiu et al, 2019).

In this research, GAs have been applied to optimize the hull design of an Octabuoy semi-submersible, in terms of the pontoon's rectangular cross section area, the cone shaped section's height and diameter, which are also called the free variables. Through the numerical evaluations in both the 1^{st}-order and 2^{nd}-order hydrodynamics, optimization through GAs has been proven to provide improved hydrodynamic performance, in terms of the energy spectrum of heave and pitch motion and the wave drift loads. This work presents a meaningful framework as a reference in the process of floating system's design.

6.2. Optimization Framework

In genetic algorithms (GAs), the first step in the optimization process is to code the single parameter or multiple parameters into a finite-length string or strings as the

starting space. Each parameter is allocated with a probability that is positively correlative with the corresponding objective function, which is also the criterion for selection of the optimal design, including the design variables in the model. The randomly selected information on each parameter with a decided probability in the population will produce the reproduction and crossover for the next generation. As a result, the strings with a higher or lower objective function value obtains a higher probability to contribute one or more offspring to the next generation, making a directional process (Papalambros et al, 2000). Therefore, GAs use a database rich in a population of strings to search multiple peaks in parallel, reducing the probability of converging to a local peak.

The framework of optimization of the Octabuoy semi-submersible hull design in this section can be presented in figure 6.2. The design parameters to be optimized are free variables while all other parameters are fixed in the optimization procedure. A parametric hull of the Octabuoy semi-submersible is firstly generated, according to the randomly generated free variables. With the help of our previously designed in-house hydrodynamics code, the numerical evaluation of the hull design's 1^{st}-order and 2^{nd}-order hydrodynamic quantities will be conducted, which will then contribute to the objective functions including the sea keeping or global performance criteria. In this study, a population of 50 makes the first generation. The information contained in the free variables that are highly correlated to smaller objective functions are with higher possibility to survive and pass their information to the offspring. Through generations' iterations, the objective functions converge and the key information can be kept, forming the optimized parameters of the hull design.

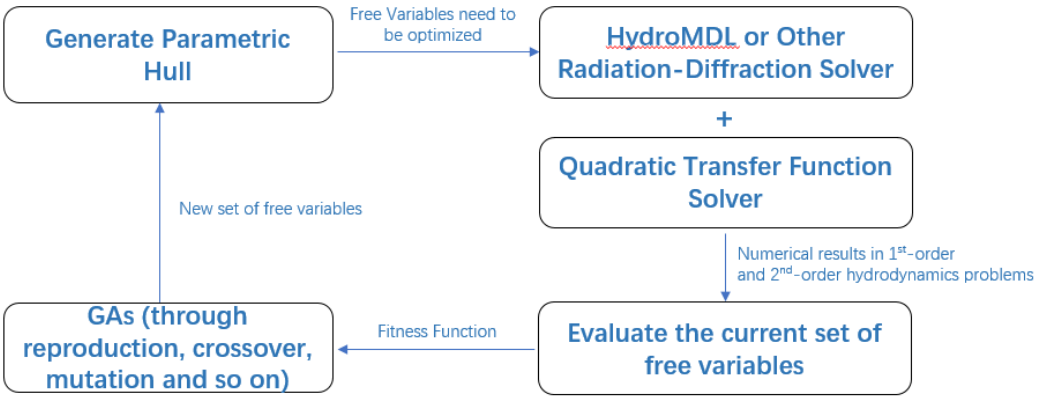

Figure 6.2. Optimization framework of the floater hull design.

6.3. Optimization of a Non-Shipshape Octabuoy Semi-Submersible Parametric Hull Design

The design of shallow draught octabuoy semi-submersible consists of an octagonal shape pontoon with a rectangular cross section, four circular columns with a cone shaped section whose half height is around the still water level, and a plate deck. The principal parameters and the numerical model of the underwater part of the prototype have been presented in Table 6.1 and Figure 6.3.

Table 6.1. Principal parameters of the original design.

Parameter	Value	Unit
Outer length	72	m
Pontoon height	4	m
Column diameter at bottom	15.5	m
Column diameter at water line	15	m
Draught	23	m
KG	17.5	m
Mass	25000	ton

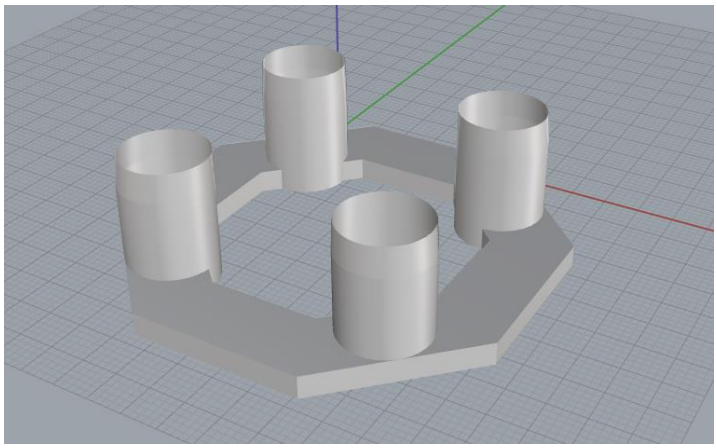

Figure 6.3. Numerical model of the original design.

The characteristic of the wave drift loads needs to be taken into consideration, especially for a floating structure with large volume. Newman's approximation has been widely applied in evaluating the 2^{nd}-order wave drift force with relatively low difference

frequency, possibly losing accuracy in the cases with relatively high difference frequency. In the previous research (Guha et al, 2015; Guha et al, 2016; Liu et al, 2017; Xie et al, 2019), the full expression of the 2nd-order wave loads applied on floating structures has been derived and presented through 1st-order and 2nd-order hydrodynamic quantities, through which the full quadratic transfer function can be numerically obtained. Through the quantities obtained in 1st-order diffraction and radiation problem, in which Green's function with finite water depth can be efficiently evaluated (Xie et al, 2017), the full 2nd-order QTF of the original Octabuoy semi-submersible design can be thus numerically evaluated and presented in Figure 6.4.

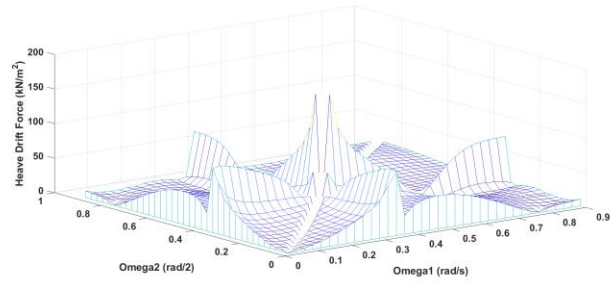

(a)

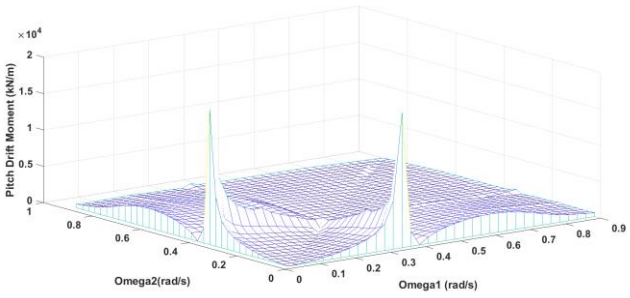

(b)

Figure 6.4. Full QTF of the original design: (a) drift force in heave motion, (b) drift moment in pitch motion.

Two optimized hull forms have been developed, both of which are with a varying cross section area at the pontoon part and a different column diameter at the water line. In the first hull form, there are mainly three parts in the vertical column, the lower part, the middle part and the cone shaped section running through the waterline. The diameter of the middle part is constant and larger than its lower part that is from the original design. This constant diameter of the middle column, the cone shaped section's height and diameter at the water line and the lower column's height are all to be optimized during the optimization process. After that, the height and the location of the middle column can be determined. In the second hull form, the middle column part with a constant diameter mentioned in the first hull form is missing, but still with the cone shaped section with its height and diameter at the water line to be optimized. The numerical models of both hull forms are shown in Figure 6.5. The free variables, namely the parameters in these two hull forms to be optimized in each iteration are shown in Figure 6.6, table 6.2 and 6.3. There is a constraint of the displacement in each iteration during the optimization process. An iteration of design with a displacement within 5% difference from the prototype is considered successfully satisfying the constraint in this research.

Two hull forms of optimizations have been developed, both of which are with a various cross section area at the pontoon part and a different column diameter at the water line. In the first hull form, there are mainly three parts in the vertical column, the lower part, the middle part and the cone shaped section running through the waterline. The diameter of the middle part is constant and larger than its lower part that is from the original design. This constant diameter of the middle column part, the cone shaped

section's height and diameter at the water line are both to be optimized during the optimization process. In the second hull form, the middle column part with a constant diameter mentioned in the first form is missing, but still with the cone shaped section with its height and diameter at the waterline to be optimized. The numerical models of both hull forms have been shown in Figures 6.5 and 6.6. The free variables, namely the parameters in these two hull forms being optimized in the optimization process are shown in Tables 6.2 and 6.3.

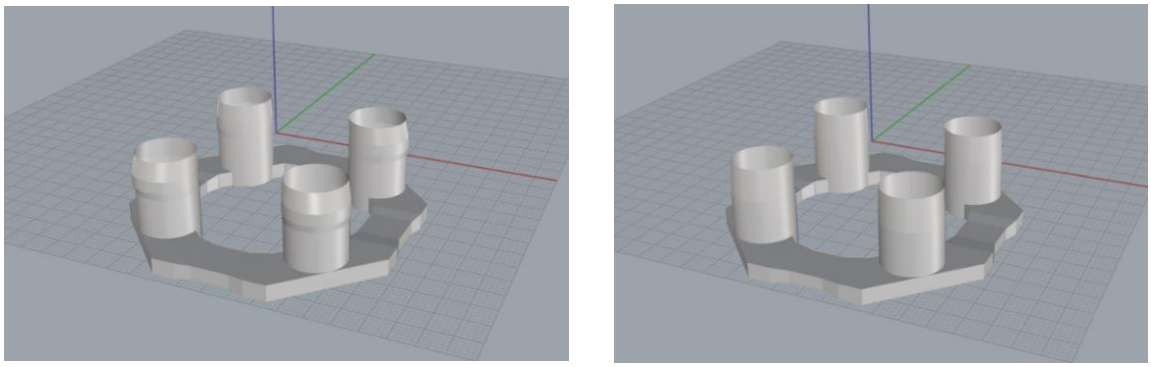

(a) (b)

Figure 6.5. The optimization: (a) hull form 1; (b) hull form 2.

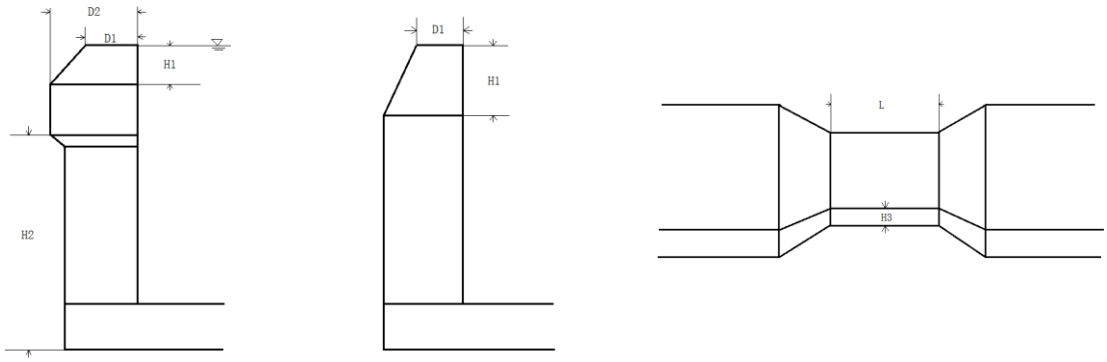

(a) (b) (c)

Figure 6.6. Design variables to be optimized in hull form 1 (a) and hull form 2 (b) and the pontoon part (c): (a) diameter of the column at the waterline (D1), diameter of the middle column (D2), cone shaped section half height (H1), height of the lower column from the keel (H2); (b) diameter of the column at the waterline (D1), cone shaped section half height (H1); (c) middle pontoon part's length (L), middle pontoon part's height (H3).

Table 6.2. Free variables in hull form 1.

Parameter	**Lower bound**	**Upper bound**	**Optimization**	**Unit**
Diameter of the column at the waterline	13.20	15.20	15.06	m
Cone shaped section half height	3.00	5.00	4.63	m
Diameter of the middle column	16.00	20.00	16.05	m
Height of the lower column	13.00	16.00	15.53	m
Middle pontoon part's length	6.00	14.00	9.78	m
Middle pontoon part's height	2.00	6.00	3.35	m

Table 6.3. Free variables in hull form 2.

Parameter	Lower bound	Upper bound	Optimization	Unit
Diameter of the column at the waterline	13.20	15.20	14.93	m
Cone shaped section half height	3.00	12.00	8.07	m
Middle pontoon part's length	6.00	14.00	8.69	m
Middle pontoon part's height	2.00	6.00	3.28	m

During the process of optimization through genetic algorithms, four objective functions that contain the information regarding the heave and pitch motions in the heading sea/roll motion in the beam sea response in both 1^{st}-order and 2^{nd}-order diffraction and radiation problem have been evaluated in each iteration. The viscous damping ratio in heave direction is assumed to be 0.6% in the numerical simulation. The first two objective functions are the total area of the spectrums of the heave and pitch motion in heading sea/roll motion in the beam sea in the 1^{st}-order, while the incident wave spectrum is the Pierson-Moskowitz spectrum with the peak period of 11 s and the significant wave height of 4.82 m. The last two objective functions are the summations of the 2^{nd}-order wave load coefficients in the heave and pitch motion in heading sea/roll motion in the beam sea with difference frequency smaller than 0.3 rad/s, to evaluate the potential level of the 2^{nd}-order motions in these two degrees.

$$F1 = \int RAO_3^2(\omega) \cdot S(\omega) d\omega \tag{6.1}$$

$$F2 = \int RAO_5^2(\omega) \cdot S(\omega) d\omega \text{ in heading sea} \tag{6.2}$$

$$or\ F2 = \int RAO_4^2(\omega) \cdot S(\omega) d\omega \text{ in beam sea}$$

$$F3 = \sum QTF_3(\omega_1,\ \omega_2)\,, |\omega_1 - \ \omega_2| < 0.3 \text{ rad/s} \tag{6.3}$$

$$F4 = \sum QTF_5(\omega_1,\ \omega_2)\,, |\omega_1 - \ \omega_2| < 0.3 \text{ rad/s in heading sea} \tag{6.4}$$

$$or\ F4 = \sum QTF_4(\omega_1,\ \omega_2)\,, |\omega_1 - \ \omega_2| < 0.3 \text{ rad/s in beam sea}$$

The desired information contained in the free variables that give a lower objective function value will be kept and passed to the updated free variables through the GAs, which will generate the next generation's parametric hull form. The four objective functions through multiple iterations are shown in Figures 6.7 and 6.8.

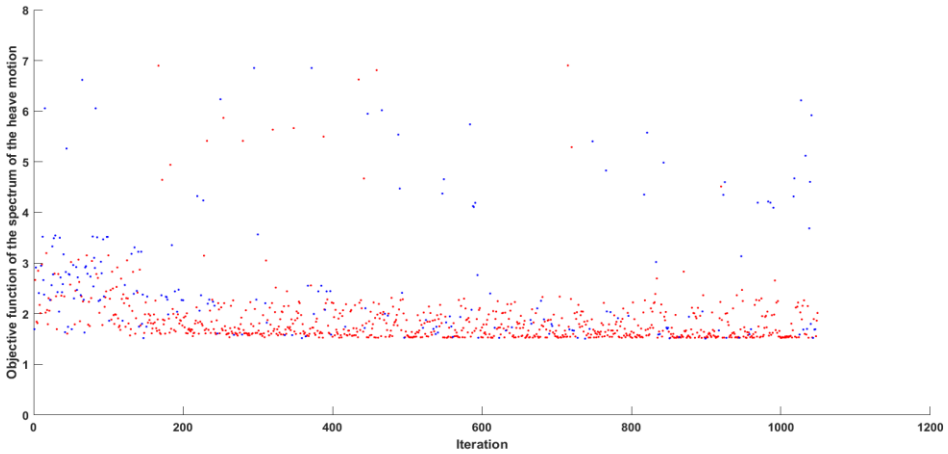

(a)

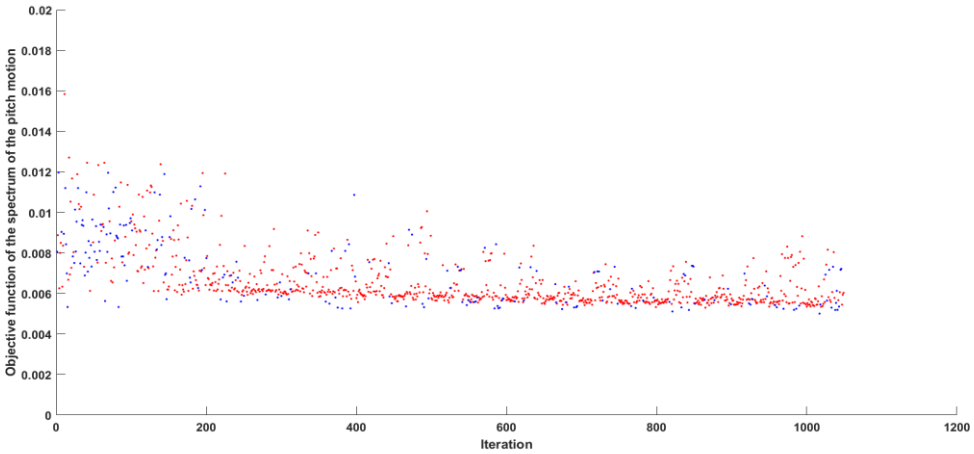

(b)

Figure 6.7. Optimization in hull form 1 through iterations of genetic algorithms: (a) objective function of the 1st-order heave motion, (b) objective function of the 1st-order pitch motion in heading sea/roll motion in beam sea, (c) objective function of the 2nd-order QTF in the heave motion, (d) objective function of the 2nd-order QTF in the pitch motion in heading sea/roll motion in beam sea (red point: constraint successfully satisfied, blue point: constraint unsuccessfully satisfied).

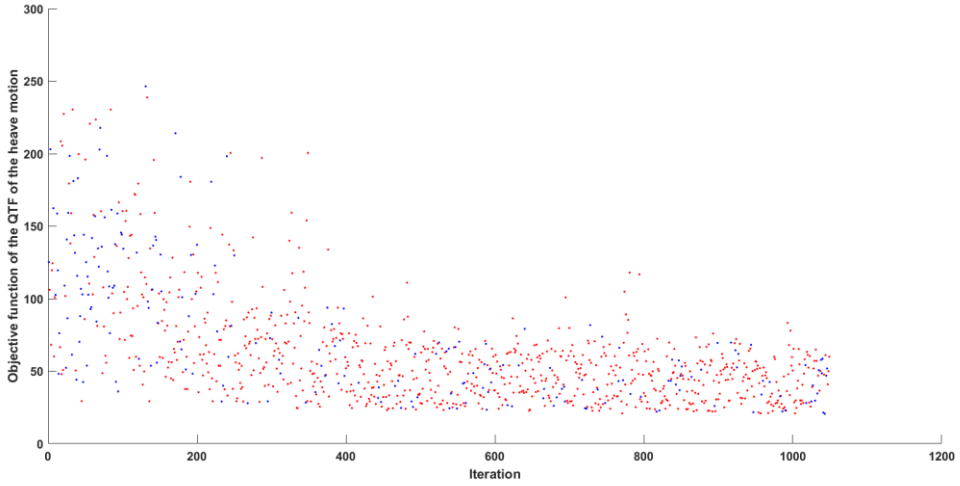

(c)

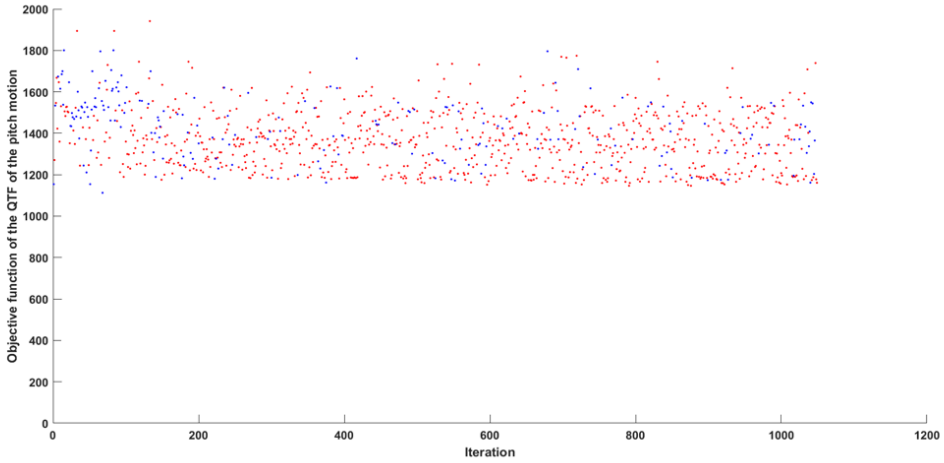

(d)

Figure 6.7. Continued.

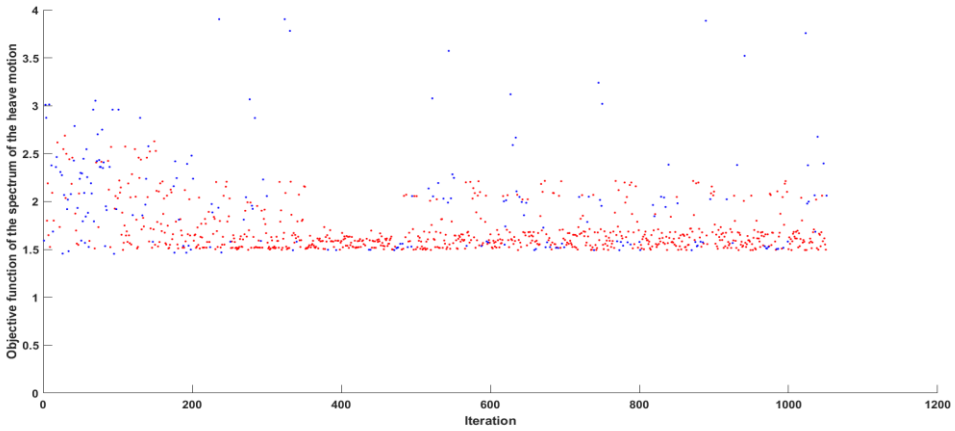

(a)

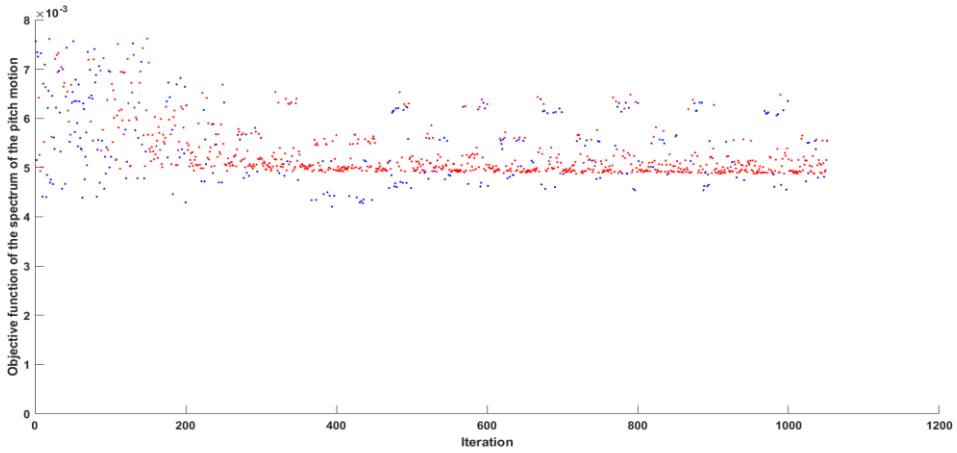

(b)

Figure 6.8. Optimization in hull form 2 through iterations of genetic algorithms: (a) objective function of the 1st-order heave motion, (b) objective function of the 1st-order pitch motion in heading sea/roll motion in beam sea, (c) objective function of the 2nd-order QTF in the heave motion, (d) objective function of the 2nd-order QTF in the pitch motion in heading sea/roll motion in beam sea (red point: constraint successfully satisfied, blue point: constraint unsuccessfully satisfied).

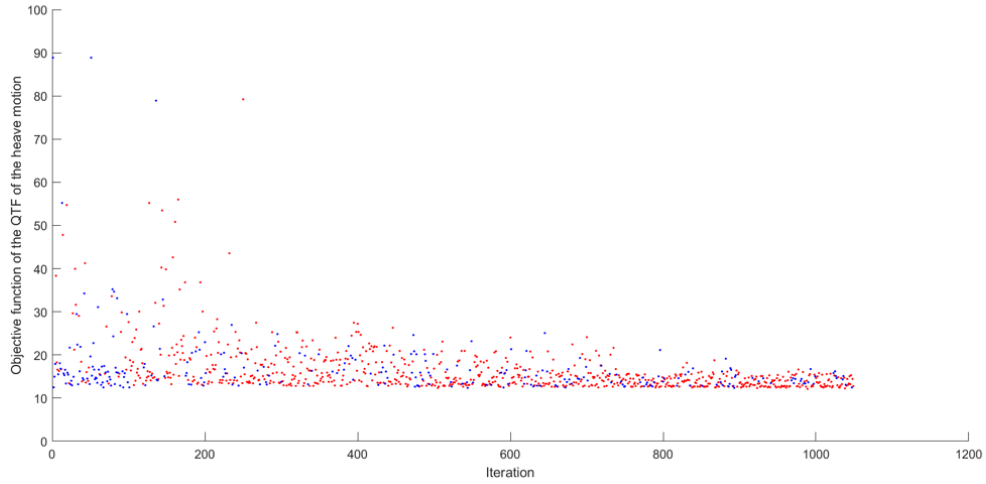

(c)

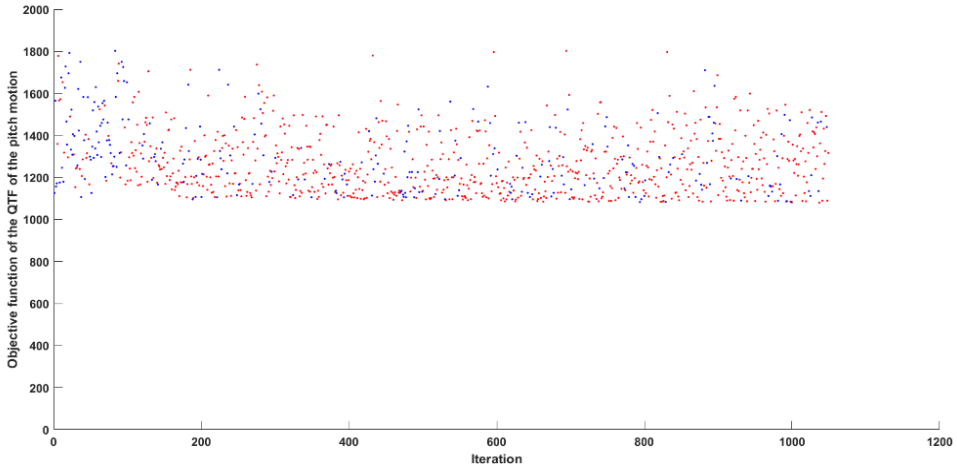

(d)

Figure 6.8. Continued.

From Figures 6.7 to 6.8, it can be seen that there are obvious convergences in the objective functions of the 1st-order heave and pitch motions and the 2nd-order drift loads in the vertical direction. The objective function regarding the wave drift load in the pitch motion does not show that obvious convergence, which indicates that the design

parameters that reduce the 1st-order heave and pitch motions and drift heave load present an insignificant correlation with the wave drift load in the pitch motion. Despite this weak correlation, there is still a significant decrease in the pitch drift moment of the optimizations, compared with the original design. The RAOs and the motion response spectrums of the optimizations in these two hull forms have been numerically evaluated and compared with the original design, respectively. Two PM incident wave spectra (Hs_1 = 4.82 m, Tp_1 = 11s; Hs_2 = 9.3 m, Tp_2 = 15s) have been selected in this scenario: the first spectrum has been chosen to evaluate the objective function in the optimization process, while the second incident wave spectrum with higher significant wave height and peak period is to evaluate the optimizations' response in the extreme sea state.

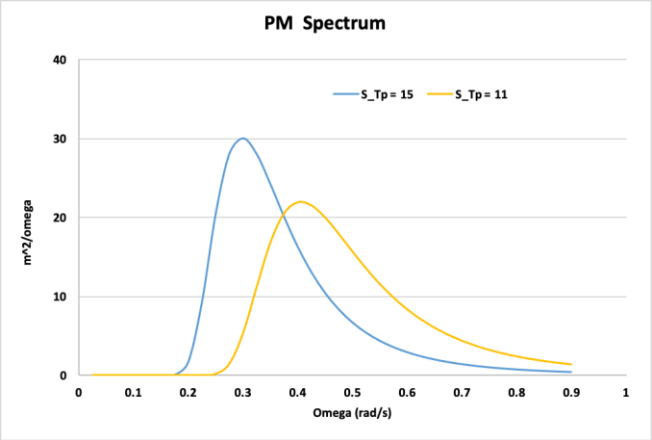

Figure 6.9. PM spectra

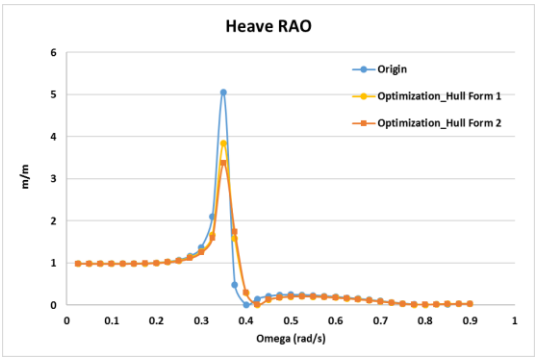

(a)

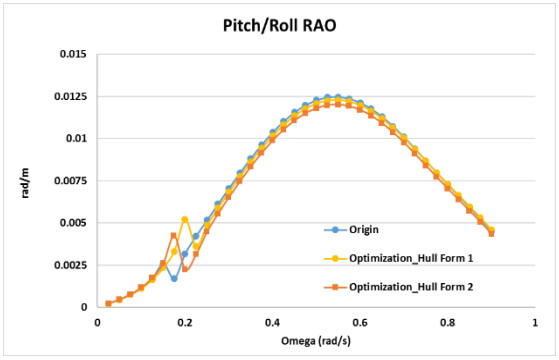

(b)

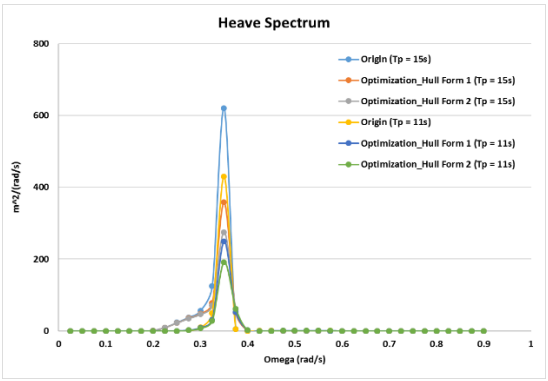

(c)

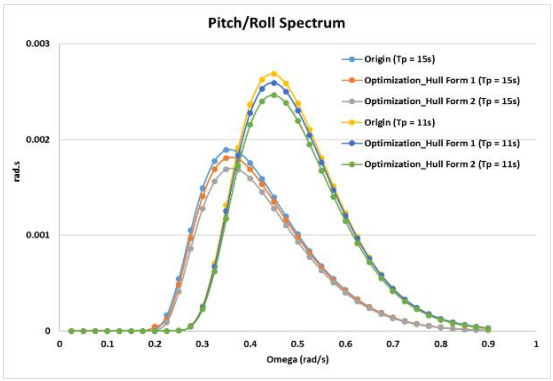

(d)

Figure 6.10. Comparison of the original design and the optimizations: (a) RAO of the heave motion, (b) RAO of the pitch motion in heading sea/roll motion in beam sea, (c) spectrum of the heave motion, (d) spectrum of the pitch motion in heading sea/roll motion in beam sea.

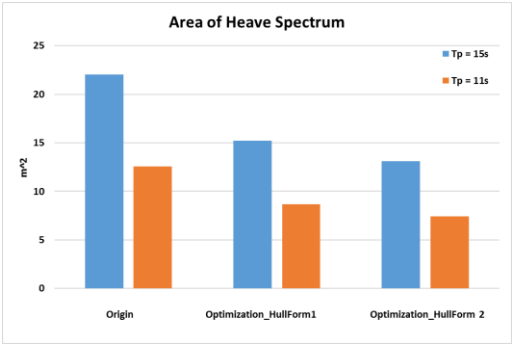

(a)

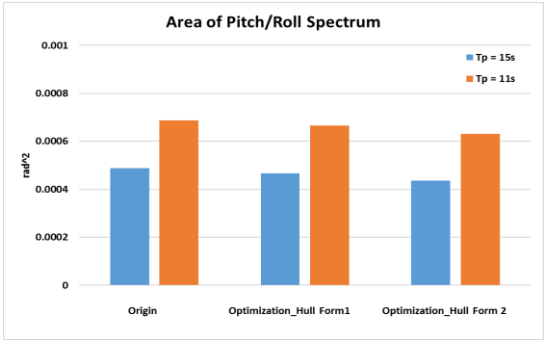

(b)

Figure 6.11. The motion spectrums: (a) heave motion, (b) pitch motion.

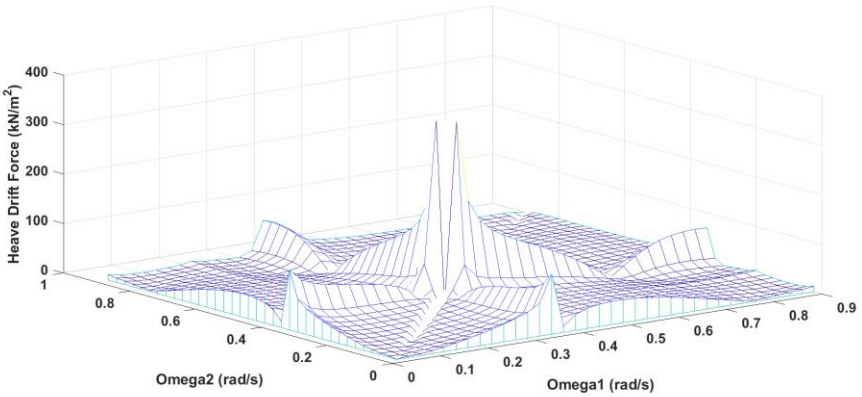

(a)

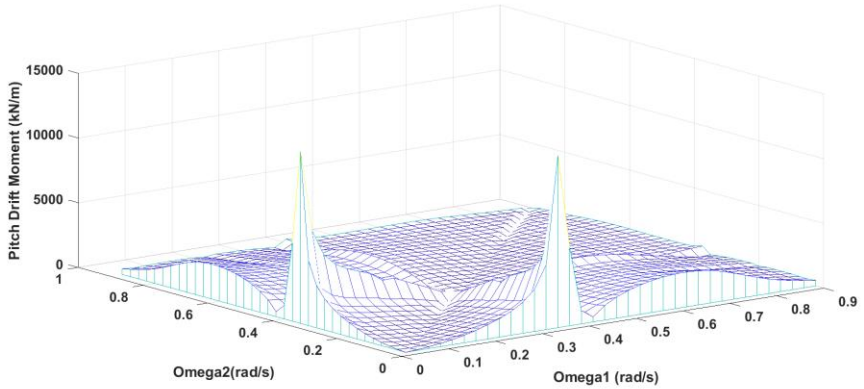

(b)

Figure 6.12. Full QTF of the optimization in hull form 1: (a) drift force in heave motion, (b) drift moment in pitch motion in heading sea/roll motion in beam sea.

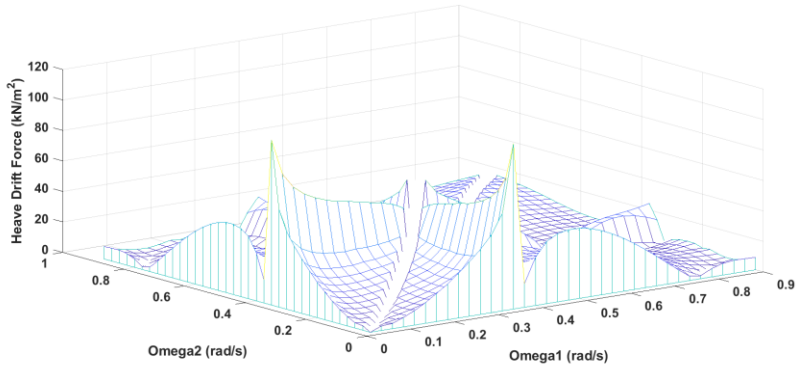

(a)

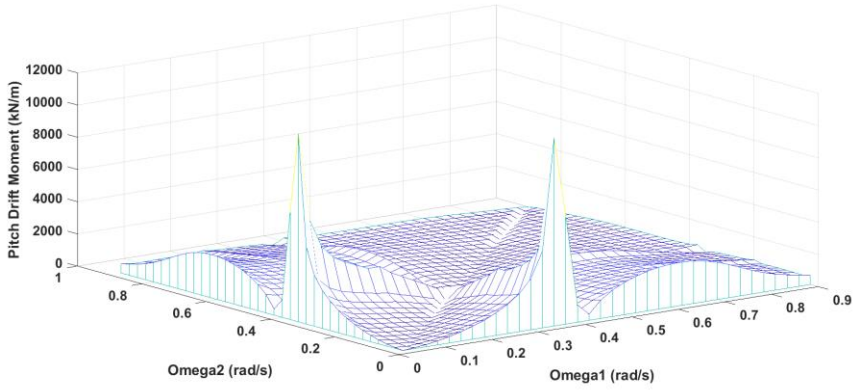

(b)

Figure 6.13. Full QTF of the optimization in hull form 2: (a) drift force in heave motion, (b) drift moment in pitch motion in heading sea/roll motion in beam sea.

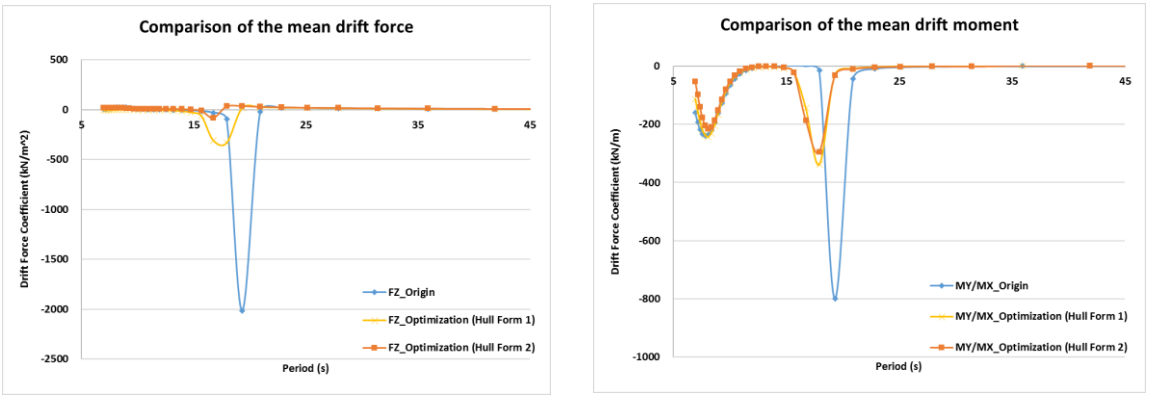

(a) (b)

Figure 6.14. Comparison of the mean drift force between the original design and the optimizations: (a) drift force in heave motion, (b) drift moment in pitch motion in heading sea/roll motion in beam sea.

Considering head sea, only the heave and pitch degrees of freedom have been taken into consideration. From Figure 6.10 to 6.11, it can be seen that both forms of optimization designs have a better hydrodynamics performance in the 1st-order motions of heave and pitch. Compared with the original design, the optimization minimizes both heave and pitch RAO's peak value and reduces the motion responses that are within the wave period range with the main wave energy in harsh sea states. As a result, there is a respectively 30.99 and 4.22 percent decline regarding the total spectra area of the motions of heave and pitch in hull form 1 while Tp is 15s, 30.92 and 3.12 percent decline while Tp is 11s. As for hull form 2, the percentage decline is 40.45 and 10.59 while Tp is 15s, 40.86 and 8.20 while Tp is 11s, respectively.

Table 6.4. Optimizations' decline in the 1st-order response spectrums compared with the original design.

Spectra	Hull form 1		Hull form 2	
	Heave	**Pitch**	**Heave**	**Pitch**
Tp15	30.99	4.22	40.45	10.59
Tp11	30.92	3.12	40.86	8.20

Moreover, the full QTF of the optimizations in the motions of heave and pitch have been numerically evaluated and presented in Figures 6.12 and 6.13. The diagonal elements of the full QTF matrix, namely the mean drift load coefficients of the optimizations have been compared with the original design in Figure 6.14, to directly present the decline in the 2nd-order difference frequency wave loads included in the objective functions and the so thus potentially reduced 2nd-order motion. Therefore, this optimization framework considering both the 1st-order and 2nd-order hydrodynamic quantities shows its efficacy in directly minimizing the shallow draught Octabuoy semi-submersible design's 1st-order heave and pitch/roll motions and potentially reducing the 2nd-order motions.

6.4. Optimization of a Parametric Shipshape FPSO Hull Design

In the previous research (Zhao et al, 2011), it has been found that the level of the 2nd-order roll motion can be as significant as the 1st-order roll motion for a single point moored (SPM) floating system. Moreover, the 2nd-order roll motion of a SPM floating system develops a coupled effect with the yaw motion in the time domain. Considering

the security of the operating instruments installed on board, minimizing or suppressing the level of the roll motion in both the 1st-order and 2nd-order is a principal object during the phase of hull design. In this scenario, the framework by using the genetic algorithms has been applied to a shipshape parametric FPSO hull design, to improve the hydrodynamics performance in the roll motion.

The prototype and the optimized design are shown in Figure 6.15. The parameters such as the longitudinal locations of the various parallel stations from the stern that can generate a parametric FPSO hull design are selected as the free variables to be optimized during the optimization process. These free variables of the prototype and the optimization design are listed in Table 6.5.

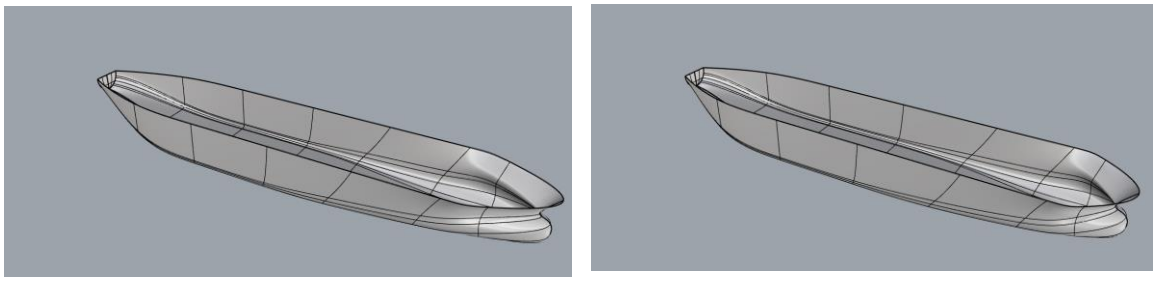

(a) (b)

Figure 6.15. Parametric FPSO hull design: (a) prototype; (b) the optimization.

Table 6.5. Free variables.

Parameters (m)	Original Design	Optimization	Lower Boundary	Upper Boundary
Parallel Midship I	53.68	46.28	33.60	81.20
Parallel Midship II	99.21	97.54	84.00	137.20
Parallel Midship III	159.24	155.34	140.00	179.20
Flat of Side I	186.66	199.27	182.00	207.20
Flat of Side II	252.2	255.43	210.00	257.60
Forward Shoulder	274.54	277.19	260.40	285.60
Bow Contour	301.46	290.32	288.40	313.60

Two objective functions that consider both the 1st-order roll motion spectrum and the 2nd-order wave loads of the roll motion in irregular waves are established as the metrics during the optimization process. A fully developed Pierson-Moskowitz incident wave spectrum with $U_{19.5}$ = 15 m/s is selected in this study. Considering that the 2nd-order roll motion presents a significant response at relatively low difference wave frequencies, there is a boundary regarding the difference wave frequency pairs in bichromatic waves in the objective function.

$$F1 = \int RAO_4^2(\omega) \cdot S(\omega) d\omega \tag{6.5}$$

$$F2 = \sum_{m=1}^{N} \sum_{n=1}^{N} 2\sqrt{S(\omega_m) S(\omega_n)}\, QTF_4(\omega_m, \omega_n) d\omega, |\omega_m - \omega_n| < 0.3 \frac{rad}{s} \tag{6.6}$$

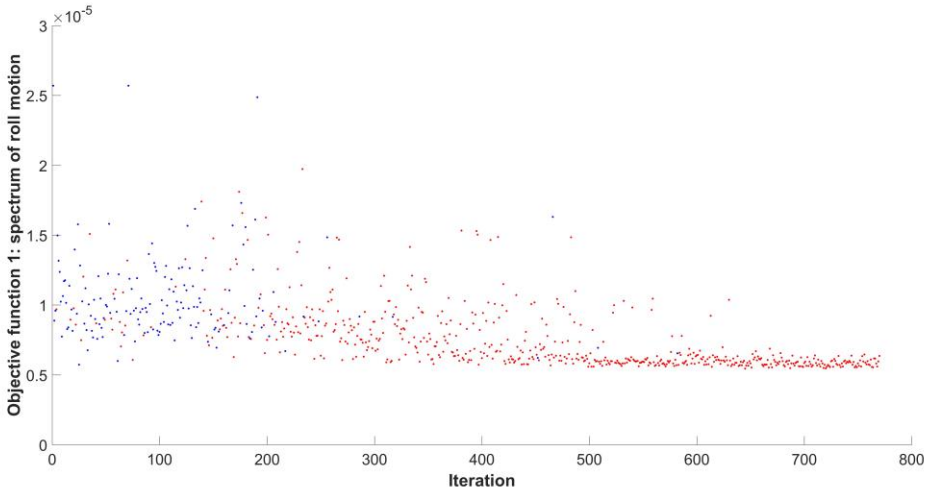

(a)

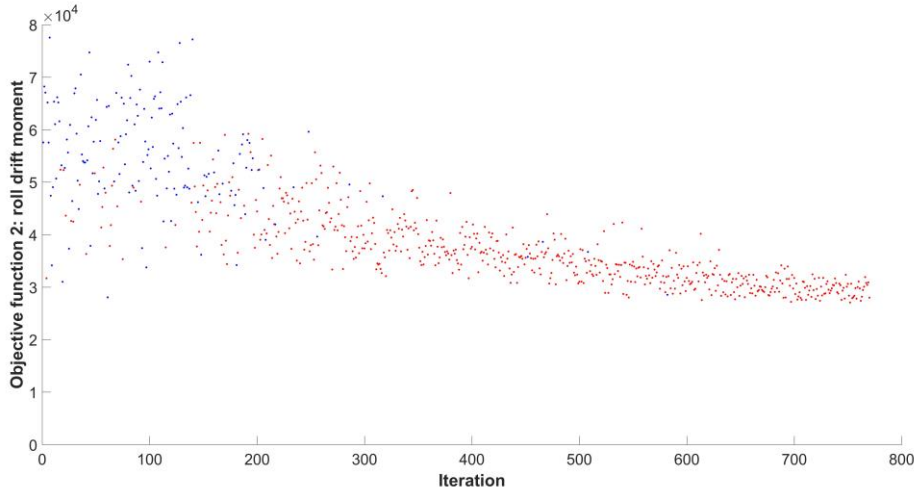

(b)

Figure 6.16. Optimization through iterations of genetic algorithms: (a) objective function of the 1st-order roll motion, (b) objective function of the 2nd-order wave load in the roll motion (red point: constraint successfully satisfied, blue point: constraint unsuccessfully satisfied).

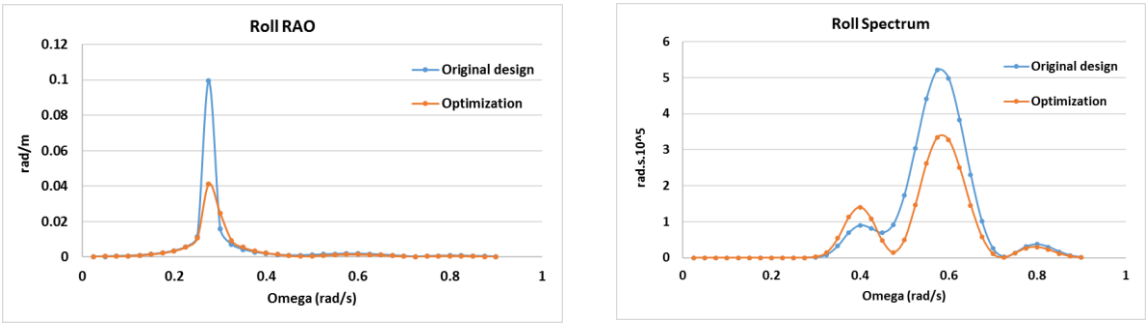

(a) (b)

Figure 6.17. Comparison of the original design and the optimizations: (a) RAO of the roll motion, (b) spectrum of the roll motion in quartering sea.

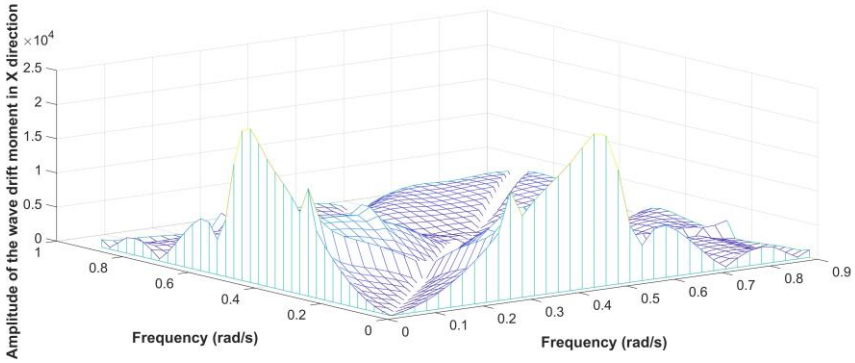

(a)

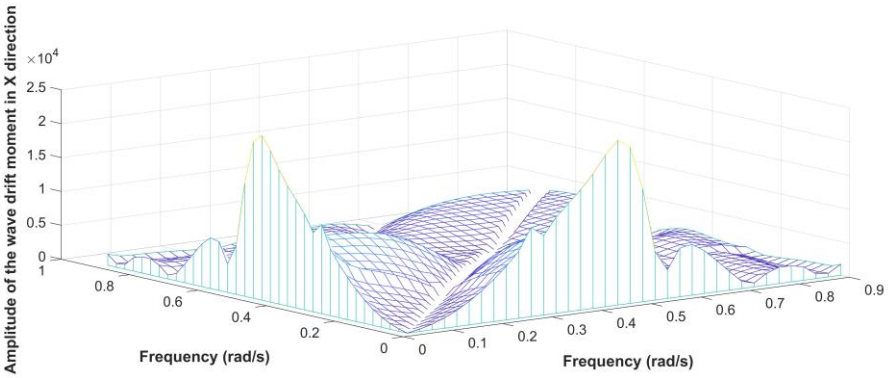

(b)

Figure 6.18. Full QTF in the roll motion: (a) prototype; (b) the optimization.

In Figure 6.16, it can be seen that both objective functions regarding the 1st-order roll motion and the 2nd-order wave loads of the roll motions in irregular waves converge and decrease through the iterations during the optimization process.

Compared with the original design, the optimized parametric FPSO hull presents a significant decrease in the 1st-order roll motion's RAO and response spectrum in irregular waves, which is shown in Figure 6.17. Figure 6.18 presents the full QTF in the roll motion of the prototype and the optimized parametric hull design. The optimized parametric hull design presents a 37.70 and 14.56 percent decrease in two objective functions respectively, which validates this optimization framework's capacity of reducing the level of the parametric shipshape FPSO's roll motion in both the 1st-order and 2nd-order.

6.5. Conclusion

A genetic algorithm has been applied to the optimized shallow draft Octabuoy Semi-Submersible hull. During the process of optimization, two hull form designs have been proposed, in terms of various cone shaped column section heights, diameters and the cross-section areas of the pontoons. During each iteration of the optimization process, a new set of free variables, namely the parameters to be optimized is generated and the corresponding hull form design is evaluated, according to its corresponding objective functions that evaluate the 1st-order and 2nd-order hydrodynamic quantities. Through the comparison of the hydrodynamic performance in both 1st-order and 2nd-order between the final optimization and the original design, it can be seen that there is an obvious decline in the RAOs of the heave and pitch, and the corresponding motion spectrum in harsh sea

state. The reduced wave drift loads enable the optimized design's improved 2^{nd}-order motions. Moreover, this optimization framework can also be applied to a shipshape parametric FPSO hull design, with improved 1^{st}-order and 2^{nd}-order roll motion performance. This work presents a meaningful framework as a reference for the optimizations of the non-shipshape and shipshape parametric floating platforms.

7. CONCLUSIONS

7.1. Concluding Remarks

The main objective of this dissertation was to develop an improved hydrodynamic analysis methodology with applications to maneuvering in waves and an optimization framework regarding offshore structure's hull, which involves several distinct topics that are steps leading towards a definite goal. A numerical evaluation of Green's function in finite water depth has been developed through the Gauss-Legendre integral with improved efficiency and efficacy in solving the 1st-order diffraction and radiation hydrodynamics problems, which was compared to published approach (Li, 2001). Next the full expression of the 2nd-order wave loads has been derived and the full quadratic transfer function of a floating structure has been numerically calculated. The effect of the water depth and the current or the vessel's forward speed on the 2nd-order wave loads have also been investigated through Aranha's formula and the Neumann-Kelvin linearization method. Through the seakeeping module considering the vessel's forward speed through the Neumann-Kelvin linearization method, a framework has been developed to numerically simulate a maneuvering vessel in waves that simultaneously incorporates the maneuvering and seakeeping aspects that includes the hydrodynamics effects corresponding to both. An optimization framework through genetic algorithms has been developed towards an automated parametric Octabuoy semi-submersible design, considering both 1st-order and 2nd-order quantities. Moreover, optimization of the 2nd-order roll motion of a Shipshape hull form was also conducted.

The following conclusions have been drawn based on the studies in the previous sections:

- The results of the Gauss-Legendre method show a good agreement with the direct integral method in evaluating Green's function in finite water depth in both the near field and far field and series form in the far field.
- The computational efficiency of the case with the field point near the water bottom is higher than that of the case with the field point near the free surface, due to the convergence of the exponential term.
- It is suggested to apply the Gauss-Legendre integral method while $R/h \leq 1$ and the series form while $R/h > 1$ to numerically evaluate Green's function and its derivatives in finite water depth.
- The results of the numerically evaluated 2nd-order mean drift loads in this study compare well with the mean drift force coefficients obtained through the industry standard commercial software, providing a convincing numerical reference while calculating the off-diagonal elements in the QTF matrix.
- As the water depth decreases, the nearly constant mean drift force coefficient in vertical Z direction at a relatively higher wave period increases and the QTFs present a more significant response in general.
- As the water depth decreases, the amplification factor in Pinkster's approximation increases significantly when the frequency pair moves towards the origin, due to the dispersion relation. The so thus dominated 2nd-order wave contribution neglects

the actual physical meaning, which means Pinkster's approximation may approach its limitation in shallow water.

- While considering the effect of current on the 2nd-order wave loads, both Aranha's formula and Neumann-Kelvin linearization provide a reasonable estimation at low Froude number for a vertical cylinder. As the Froude number increases, the numerical results from Aranha's formula lack of physical meaning and meet its limitation, due to its low current speed premise.
- The Neumann-Kelvin linearization provides a more robust numerical estimation and converges to the expression of the mean 2nd-order forces and moments in the previous research when the basis flow reduces to zero.
- The wave drift loads with wave drift damping drives the vessel turning trajectory away from the calm water trajectory, resulting in a drifting path. As the wave length decreases, this drifting phenomenon is more pronounced.
- Maneuvering in beam seas also presents an asymmetric characteristic for the vessel heading in the zig-zag tests. The framework herein is an accurate and efficient approach to study the maneuvering of ships in waves.
- The optimization framework in this research by using the genetic algorithms shows its efficacy in optimizing a non-shipshape parametric hull, the shallow draft Octabuoy Semi-Submersible platform with reduced 1st-order and 2nd-order heave and pitch motions, and a parametric shipshape FPSO hull with reduced 1st-order and 2nd-order roll motion.

7.2. Contributions

The contributions of this thesis are summarized as follows:

- The Gauss-Legendre method has been applied to numerically evaluate Green's function in finite water depth with improved efficiency and efficacy in solving the 1st-order diffraction and radiation hydrodynamics problems, compared to the Gauss-Laguerre method as compared to the published approach.
- A full expression of the 2nd-order wave loads has been derived and the corresponding numerical study has been conducted. It is concluded that the waterline integral term of this full expression of the 2nd-order wave loads is an important factor in evaluating the 2nd-order wave loads.
- A framework that considers the coupled maneuvering and seakeeping problems that involves an accurate prediction of the second-order wave loads of a maneuvering vessel in waves has been introduced and validated. This framework herein is an accurate and efficient approach to capture the main characteristic of the turning trajectory and study the maneuvering of ships in waves and compare well to experiments.
- An optimization framework has been established by using the genetic algorithms to optimize a non-shipshape shallow draft Octabuoy Semi-Submersible parametric hull design and a shipshape parametric FPSO design, with reduced 1st-order and 2nd-order hydrodynamics quantities.

7.3. Recommendations for the Future Research

- The empirical maneuvering model can be improved. The sensitivity of the physical model in the maneuvering framework to various hydrodynamic and wave parameters such as rudder perturbations can be conducted and extended for the design of vessels.
- The current maneuvering framework can be extended and contributed to the IMO standards for determining the minimum propulsion power to guarantee the maneuverability of vessels in adverse conditions.
- With the framework of numerically simulate the maneuvering in waves and optimization, the genetic algorithms can be extended to optimize or enhance the vessel's maneuverability during the phase of hull design.
- The optimization framework through the genetic algorithms can be applied to the renewable energy industry, such as enhancing the efficiency of the wave energy converter (WEC) and the hydrodynamic performance of floating base of the floating wind turbine.

REFERENCES

Abramowitz, M., Stegun, I. A., 1964. Handbook of Mathematical Functions with Formulas, Graphs, and Mathematical Tables. Government Printing Office, Washington, and Dover, New York, USA.

American Bureau of Shipping, 2006. Guide for Vessel Maneuverability. Houston, TX.

Aranha, J. A. P., 1994. A Formula for 'Wave Damping' in the Drift of a Floating Body. J. Fluid Mech., 275, 147-155.

Aranha, J. A. P., 1996. Second-Order Horizontal Steady Forces and Moment on a Floating Body with Small Forward Speed. J. Fluid Mech., 313, 39-54.

Aranha, J. A. P., Fernandes, A. C., 1995. On the Second-Order Slow Drift Force Spectrum. Applied Ocean Research, 17, 311-313.

Aranha, J. A. P., Silva, S. da, Martins, M. R., Leite, A. J. P., 2001. A Weathervane Ship under Wave and Current Action: An Experimental Verification of the Wave Drift Damping Formula. Applied Ocean Research, 23, 103-110.

Available online: http://www.simman2019.kr/contents/KCS.php (accessed on 20th March 2020).

Bailey, P. A., Price, W.G., Temarel, P., 1997. A Unified Mathematical Model Describing the Maneuvering of a Ship Travelling in a Seaway. Trans. R. Inst. Nav. Archit., 140, 131–149.

Barr, R. A., Webster, W. C., 2021. Principles of Naval Architecture Maneuvering. Society of Naval Architects and Marine Engineers, USA.

Birk, L., Clauss, G.F., 2001. Automated Hull Optimization of Offshore Structures Based on Rational Seakeeping Criteria. Proceedings of the 11th International Offshore and Polar Engineering Conference. June, Stavanger, Norway.

Boese, P., 1970. Eine einfache Methode zur Berechnung der Widerstandserhöhung eines Schiffes im Seegang. Institute fur Schiffbau der Univ. Hamburg.

Brard, R., 1972. The Representation of a Given Ship Form by Singularity Distributions When the Boundary Condition on the Free Surface is Linearized. J. Ship Research, 16, 79-92.

Lee, C. H., 2013. WAMIT User Manual, Chestnut Hill, MA, USA.

Chen X. B., Duan W. Y., 2007. Formulation of Low-Frequency QTF by $O(\Delta\omega)$ Approximation. 22nd International Workshop on Water Waves and Floating Bodies, Plitvice (Crotatia).

Chillcce, G., Moctar, O., 2018. A Numerical Method for Maneuvering Simulation in Regular Waves. Ocean Eng., 170, 434–444.

Clauss, G. F., Birk, L., 1996. Hydrodynamic Shape Optimization of Large Offshore Structures. Applied Ocean Research, 18, 157-171.

Dai, Y. S., Duan, W. Y., 2007. Potential Flow Theory of Ship Motions in Waves. National Defense Industry Press, Beijing, China.

Dawson, C. W., 1977. A Practical Computer Method for Solving Ship-Wave Problem. Proceedings of the Second International Conference on Numerical Ship Hydrodynamics, Berkeley, California.

Dean, R. G., Sharma, J. N., 1981. Simulation of Wave Systems due to Nonlinear

Directional Spectra. Int. Syp. Hydrodynamics Ocean Eng., Norwegian Inst. Of Tech., 2, 1211-1222.

Faltinsen, O. M., 1990. Sea Loads on Ships and Offshore Structures. Cambridge University Press, Cambridge, UK.

Guevel, P., Vaussy, P., Kobus, J. M., 1974. The Distribution of Singularities Kinematically Equivalent to a Moving Hull in the Presence of a Free Surface. Shipbuilding Progress, 21, 311-324.

Guha, A., Falzarano, J., 2015. The Effect of Hull Emergence Angle on the Near Field Formulation of Added Resistance. Ocean Eng., 105, 10–24.

Guha, A., Falzarano, J., 2015. Estimation of Hydrodynamic Forces and Motions of Ships with Steady Forward Speed. Int. Shipbuild. Prog., 62, 113–138.

Guha, A., Falzarano, J. M., 2016. The Effect of Small Forward Speed on Prediction of Wave Loads in Restricted Water Depth. Ocean Systems Engineering, 6(4), 305-324.

Guha, A., Falzarano, J., 2016. Optimization of a Parametric FLNG in Finite Water Depth. 35th International Conference on Offshore Mechanics and Arctic Engineering, June, Busan, South Korea.

Hermans, A. J., 1999. Low-Frequency Second-Order Wave-Drift Forces and Damping. Journal of Engineering Mathematics, 35(1-2), 181-198.

Hirdaris, S. E., Bai, W., Dessi, D., Ergin, A., Gu, X., et al., 2015. Loads for Use in the Design of Ships and Offshore Structures. Ocean Eng., 78, 131–174.

Holland, J. H., 1973. Genetic Algorithms and the Optimal Allocations of Trials. SIAM Journal of Computing, 2(2), 88-105.

Holland, J. H., 1984. Genetic Algorithms and Adaptation. Proceedings of the NATO Advanced Research Institute on Adaptive Control of Ill-Defined Systems, 317-333, Plenum Press, New York.

Islam, H., Soares, C.G., 2018. Estimation of Hydrodynamic Derivatives of a Container Ship Using PMM Simulation in OpenFOAM. Ocean Eng., 164, 414–425.

John, F., 1950. On the Motion of Floating Bodies. Communication of Pure Applied Mathematics, 3, 45-101.

Joncquez, S. A. G., 2009. Second-Order Forces and Moments Acting on Ships in Waves. PhD Thesis, Technical University of Denmark, Copenhagen, Denmark.

Kim, C. H., 2008. Nonlinear Waves and Offshore Structures. World Scientific Publishing, Singapore.

Kim, D. J., Yun, K., Park, J., Yeo, D. J., Kim, Y. G., 2019. Experimental Investigation on Turning Characteristics of KVLCC2 Tanker in Regular Waves. Ocean Eng., 175, 197–206.

Kim, K. H., Kim, Y. H., 2010. Comparative Study on Ship Hydrodynamics Based on Neumann-Kelvin and Double-Body Linearization in Time-Domain Analysis. International Journal of Offshore and Polar Engineering, 20(4), 265-274.

Kim, K. H., Kim, Y. H., 2011. Numerical Study on Added Resistance of Ships by Using a Time-Domain Rankine Panel Method. Ocean Eng., 38, 1357-1367.

Kim, M. H., Yue, D. K. P., 1990. The Complete Second-Order Diffraction Solution for an Axisymmetric Body, part 2, Bichromatic Incident Waves and Body Motions. J. Fluid Mech., 211, 557-593.

Korbijn, F., Husem, I., Pettersen, E., 2005. Octabuoy SDM, A Compact Semi-Submersible Design for Deepwater Applications. 24th International Conference on Offshore Mechanics and Arctic Engineering, June, Halkidiki, Greece.

Lee, S.K., Hwang, S.H., Yun, S.W., Rhee, K.P., Seong, W.J., 2009. An Experimental Study of a Ship Maneuverability in Regular Waves. Proceedings of the International Conference on Marine Simulation and Ship Maneuverability, Panama City, Panama.

Lee, J., Kim, Y., 2020. Study on Steady Flow Approximation in Turning Simulation of Ship in Waves. Ocean Eng., 195, 106645.

Li, L., 2001. Numerical Seakeeping Predictions of Shallow Water Effect on Two Ship Interactions in Waves. PhD. Dissertation, Dalhousie University, Canada.

Liu, R. M., Ren, H. L., Li, H., 2008. An Improved Gauss-Laguerre Method for Finite Water Depth Green Function and Its Derivatives. Journal of Ship Mechanics, 12(2), 188-196.

Liu, Y., Falzarano, J. M., 2016. Suppression of Irregular Frequency in Multi-Body Problem and Free-Surface Singularity Treatment. Proceedings of the ASME 2016 35th International Conference on Ocean, Offshore and Arctic Engineering, Busan, South Korea, June.

Liu, Y. J., Falzarano, J. M., 2017. Suppression of Irregular Frequency Effect in Hydrodynamic Problems and Free-Surface Singularity Treatment. Journal of Offshore Mechanics and Arctic Engineering, 139(5), 051101.

Liu, Y. J., Falzarano, J. M., 2017. A Method to Remove Irregular Frequencies and Log Singularity Evaluation in Wave-Body Interaction Problems. Journal of Ocean Engineering and Marine Energy. 3(2), 161-189.

Liu, Y. J., Falzarano, J. M., 2017. Irregular Frequency Removal Methods: Theory and Applications in Hydrodynamics. Journal of Marine System and Ocean Technology, 12(2), 49-64.

Liu, Y., Falzarano, J. M., 2017. Improvement on the Accuracy of Mean Drift Force Calculation. Proceedings of the ASME 2017 36th International Conference on Ocean, Offshore and Arctic Engineering, Trondheim, Norway, June.

Liu, Y., Falzarano, J. M., 2019. A Wall Damping Method to Estimate the Gap Resonance in Side-by-Side Offloading Problems. Ocean Eng., 173, 510-518.

Maruo, H., 1960. Wave Resistance of a Ship in Regular Head Seas, Bulletin of the Faculty of Engineering. Yokohama National University, March.

Masuda, K., Asanuma, T., Maeda, H., Ikoma, T., Rheem, C. K., 2002. A Prediction Method for Horizontal Plane Behavior of FPSO under the Single Point Mooring. Proceedings of 21st International Conference on Offshore Mechanics and Arctic Engineering, Oslo, Norway.

Munipalli, J., Pistani, F., Thiagarajan, K. P., Winsor, F., Colbourne, B., 2007. Weathervaning Instabilities of a FPSO in Regular Waves and Consequence on Response Amplitude Operators. Proceedings of 26th International Conference on Offshore Mechanics and Arctic Engineering, San Diego, CA, USA.

Molin, B., 2002. Hydrodynamique des Structures Offshore. Editions Technip, Paris, France.

Molin, B., 2021. Offshore Structure Hydrodynamics. Cambridge University Press, Ocean Technology Series, Cambridge, UK.

Newman, J. N., 1967. The Drift Force and Moment on Ships in Waves. Journal of Ship Research, 11(3), 51-60.

Newman, J. N., 1974. Second-Order Slowly Varying Forces of Vessels in Irregular Waves. Proceedings of International Symposium on Dynamics of Marine Vehicles and Structures in Waves. IMechE, London, 182-186.

Newman, J. N., 1984. Approximations for the Bessel and Struve Functions. Mathematics of Computation, 43(168), 551-556.

Newman, J. N., 1985. Algorithms for the Free-surface Green Function. Journal of Engineering Mathematics, 19, 57-67.

Noblesse, F., 1982. The Green Function in the theory of Radiation and Diffraction of Regular Water Waves by a Body. J. Eng. Math., 16, 137-169.

Noblesse, F., 1983. Integral Identities of Potential Theory of Radiation and Diffraction of Regular Water Waves by a Body. J. Eng. Math., 17, 1-13.

Nomoto, K., Taguchi, T., Honda, K., Hirano, S., 1957. On the Steering Qualities of Ships. Int. Shipbuild, Prog., 4, 354–370.

Pettersen, E., Machado-Damhaug, U. E., 2007. Parametric Motion Responses for Deep Draft Production Units. Proceedings of the 17th International Offshore and Polar Engineering Conference. July, Lisbon, Portugal.

Pinkster, J. A., 1979. Mean and Low Frequency Wave Drifting Forces on Floating Structures. Ocean Eng., 6(1), 593-615.

Pinkster, J. A., 1980. Low Frequency Second Order Wave Exciting Forces on Floating Structure. Delft University of Technology, Delft.

Rezende, F. C., Oliveira, A. C., Chen, X. B., Menezes, F., 2013. A Comparison of Different Approximations for Computation of Second Order Roll Motions for a FLNG. Proceedings of the ASME 2013 32nd International Conference on Ocean, Offshore and Arctic Engineering, Nantes, France.

Romberg, W., 1955. Vereinfachte Numerische Integration. Det Kongelige Norske Videnskabers Selskab Forhandlinger, Trondheim, 28(7), 30-36.

Skejic, R., 2013. Ships Maneuvering Simulations in a seaway-How Close Are We to Reality? In Proceedings of the International Workshop on Next Generation Nautical Traffic Models, Delft, The Netherlands, July.

Skejic, R., Faltinsen, O.M., 2008. A Unified Seakeeping and Maneuvering Analysis of Ships in Regular Waves. J. Mar. Sci. Technol. 13, 371–394.

Seo, M.G., Kim, Y., 2011. Numerical Analysis on Ship Maneuvering Coupled with Ship Motion in Waves. Ocean Eng., 38, 1934–1945.

Somayajula, A., Falzarano, J. M., 2017. A Comparative Assessment of Approximate Methods to Simulate Second Order Roll Motion of FPSOs. Ocean Systems Engineering, 7, 53-74.

Sutulo, S., Soares, C.G., 2019. On the Application of Empiric Methods for Prediction of Ship Maneuvering Properties and Associated Uncertainties. Ocean Eng., 186, 106111.

Trassoudaine, D., Naciri, M., 1999. A Comparison of a Heuristic Wave Drift Damping Formula with Experimental Results. Applied Ocean Research, 21, 93-97.

Telste, J. G., Noblesse, F., 1986. Numerical Evaluation of the Green Function of Water-Wave Radiation and Diffraction. Journal of Ship Research, 30(2), 69-84.

Ueno, M., Nimura, T., Miyazaki, H., 2003. Experimental Study on Maneuvering Motion of a Ship in Waves. Proceedings of the International Conference on Marine Simulation and Ship Maneuverability, Kanazawa, Japan, 25-28 August.

Uharek, S., Cura-Hochbaum, A., 2018. The Influence of Inertial Effects on the Mean Forces and Moments on a Ship Sailing in Oblique Waves Part B: Numerical prediction using a RANS Code. Ocean Eng., 165, 264–276.

Wang, R. S., 1992. The Numerical Approach of Three Dimensional Free-Surface Green Function and its Derivatives. Journal of Hydrodynamics, 7(3), 277-286.

Wang, J.H., Zou, L., Wan, D.C., 2018. Numerical Simulations of Zigzag Maneuver of Free Running Ship in Waves by RANS-Overset grid method. Ocean Eng., 162, 55–79.

Wang, H., Falzarano, J. M., 2017. Energy Balance Analysis Method in Oscillating Type Wave Converter. J. Ocean Eng. & Mar. Energy, 3(3), 193-208.

Wang, H., Sitanggang, K., Falzarano, J. M., 2017. Exploration of Power Take Off in Wave Energy Converters with Two-Body Interaction. Ocean Syst. Eng., 7(2), 89-106.

Wang, H., Somayajula, A., Falzarano, J. M., Xie, Z. T., 2020. Development of a Blended Time-Domain Program for Predicting the Motions of a Wave Energy Structure. Journal of Marine Science and Engineering, 8, 1.

Wehausen, J. V., Laitone, E. V., 1960. Surface Waves. Encyclopedia Phys., 9, 446-815.

Wichers, J. E. W., Devlin, P. V., 2001. Effect of Coupling of Mooring Lines and Risers on the Design Values for a Turret Moored FPSO in Deep Water of the Gulf of Mexico. Proceedings of the 11th ISOPE Conference, Stavanger, Norway.

Wu, H., Zhang, C. L., Zhu, Y., Li, W., Wan, D. C., Noblesse, F., 2017. A Global Approximation to the Green Function for Diffraction Radiation. European Journal of Mechanics B/Fluids, 65, 54-64.

Xie, Z. T., Yang, J. M., Hu, Z. Q., Zhao, W. H., Zhao, J. R., 2015. The Horizontal Stability of an FLNG with Different Turret Locations. International Journal of Naval Architecture and Ocean Engineering, 7, 244-258.

Xie, Z. T., Yang, J. M., Hu, Z. Q., Xie, B., Wang, J. R., 2015. Investigation on Hydrodynamic Performance of an SPM FLNG. China Offshore Oil and Gas, 27(1), 96-101.

Xie, Z. T., Liu, Y. J., Falzarano, J. M., 2017. A More Efficient Numerical Evaluation of the Green Function in Finite Water Depth. Ocean Systems Engineering, 7(4), 399-412.

Xie, Z. T., Liu, Y. J., Falzarano, J. M. 2019. A Numerical Evaluation of the Quadratic Transfer Function for a Floating Structure. Proceedings of the ASME 2019 38th International Conference on Ocean, Offshore and Arctic Engineering, Glasgow, Scotland, UK.

Xie, Z. T., Falzarano, J. M., 2020. Study on 2nd-Order Wave Loads with Forward Speed through Aranha's Formula and Neumann-Kelvin linearization. Proceedings of the

ASME 2020 39th International Conference on Ocean, Offshore and Arctic Engineering, Fort Lauderdale, FL, USA.

Xie, Z. T., Falzarano, J. M., Wang, H., 2020. A Framework of Numerically Evaluating the Maneuvering Vessel in Waves. Journal of Marine Science and Engineering, 8(6), 392.

Xie, Z. T., Falzarano, J. M., 2020. An Optimization Framework of a Parametric Octabuoy Semi-Submersible Design. International Journal of Naval Architecture and Ocean Engineering, 12, 711-722.

Yu, M., Falzarano, J. M., 2017. A Comparison of the Neumann-kelvin and Rankine Source Methods for Wave Resistance Calculations. Ocean Systems Engineering, 7(4), 371-398.

Yang, P., Gu, X. K., Tian, C., Cheng, X. M., Ding, J., 2014. Numerical Study of 3D Pulsating Source Green Function of Finite Water Depth. Proceedings of the ASME 2014 33rd International Conference on Ocean, Offshore and Arctic Engineering, San Francisco, USA.

Zhang, B. J., Zhang, S. L., 2018. Research on Ship Design and Optimization Based on Simulation-Based Design (SBD) Technique. Shanghai Jiao Tong University Press, Shanghai, China.

Zhang, W., Zou, Z. J., Deng, D. P., 2017. A Study on Prediction of Ship Maneuvering in Regular Waves. Ocean Eng., 137, 367–381.

Zhao, W. H., Yang, J. M., Hu, Z. Q., Wei, Y. F., 2011. Recent Developments on the Hydrodynamics of Floating Liquid Natural Gas (FLNG). Ocean Eng., 38, 1555-1567.

Zhao, W. H., Yang, J. M., Hu, Z. Q., Xiao, L. F., Peng, T., 2012. Investigation on the Hydrodynamic Performance of an Ultra Deep Turret-Moored FLNG system. China Ocean Engineering, 26(1), 77-93.